Sapienza
Università di Roma

HIGHER ORDER ELECTROACOUSTIC LAMB WAVES FOR SENSOR APPLICATIONS

Department of Information Engineering, Electronics and Telecommunications

Doctoral Program in Information and Communications Technologies – Cycle XXXI

Candidate

Muhammad Hamidullah

ID Number: 1703256

Thesis Supervisor

Prof. Giampiero de Cesare

Co-supervisor

Dr. Cinzia Caliendo

A thesis submitted in partial fulfillment of the requirements for the degree of

Doctor of Philosophy in Information and Communications Technologies (ICT)

October 2018

Thesis defended on February 2019
in front of a Board of Examiners composed by:
Prof. Nome Cognome (chairman)
Prof. Nome Cognome
Dr. Nome Cognome

Higher Order Electroacoustic Lamb Waves for Sensor Applications
Ph.D. thesis. Sapienza – University of Rome
ISBN: 000000000-0

Version: October 31, 2018
Author's email: hmdoel@gmail.com

ACKNOWLEDGMENTS

Firstly, I would like to express my gratitude to my supervisors, Prof Giampiero de Cesare and Dr. Cinzia Caliendo to give me the opportunity to work in this PhD research project. The research work was performed mostly in the Institute for Photonic and Nanotechnologies (IFN) – CNR Rome, so I would like to specially acknowledge Dr Cinzia Caliendo, with whom I have worked closely for the last three years, for the fruitful discussion, and all the help and support not only in the technical aspect but also in overcoming all obstacles that I faced during my stay in Rome.

I am grateful to all colleagues and staffs of IFN-CNR Rome that have been very supportive and helpful, especially during the experiment works inside the cleanroom. I would like to thank Dr. Ennio Giovine that has supported me in the EBL microfabrication process. Also, to the director of the institute, Dr Gabriella Castelano, for all the help in solving all administrative issues during my research stay in the institute.

I would like to thanks all member of the MSCA-ITN SAWTrain: the ESR fellows who have gone through the same journey in this training network, the PIs particularly my SAWtrain co-supervisor, Dr Jorge Pedros for all the support during my secondment in UPM Madrid and for the help on the characterisation of the devices using RF probe. This research project will not be possible without the financial support from the European Union's Horizon 2020 research and innovation programme under the Marie Sklodowska-Curie grant agreement No 642688

Finally, I would like to thank my friends and family back in Indonesia and Singapore for all the moral support extending across distance and time zone. Special dedication is for my mother for her unconditional love, to whom I dedicate this thesis report.

ABSTRACT

Since the emergence of acoustic waves devices for sensing application, more than 30 years ago, extensive works have been reported that involve different acoustic waves types and modes, for both gaseous and liquid environment applications. Concurrently, the convergence between biology, chemistry, and microengineering requires a miniaturised and highly sensitive sensor able to detect a miniscule amount of a substance in liquid environments. Acoustic wave sensors able to work in a liquid environment include, other than the well-known Quartz Crystal Microbalance (QCM), devices based on the propagation of several other types of acoustic waves, such as pseudo Surface Acoustic Waves (PSAW), high velocity PSAWs (HVPSAW), Love Waves, shear horizontal acoustic plate modes (SHAPM), and the fundamental symmetric and antisymmetric Lamb modes, A_0 and S_0, which offer high sensitivities, high operation frequencies, and are compatible with the Integrated Circuit technology.

The recent trend of surface acoustic waves (SAW) devices is shifting toward thin film plate acoustic waves (PAW) motivated by the requirement of achieving ultra-high frequency (UHF) devices for application in the telecommunication field (GHz range), and for the development of enhanced sensors sensitivity. The fundamental A_0 and S_0 Lamb waves have been extensively reported for the sensor application in liquid environments but limited to the low frequency range due to specific requirement of large metal electrode periodicity (that corresponds to the acoustic wavelength) with respect to the plate thickness. Higher order quasi-longitudinal Lamb waves (qL-LW) is a promising candidate to overcome the low frequency limitation by reducing the electrodes periodicity and thus offering higher operation frequency. However, as to our knowledge, only little work has been reported on qL-LWs, especially the use of simulation and finite element method (FEM) to explore qL-LWs for liquid sensing applications.

The main objective is to perform a theoretical study, finite element method (FEM) simulation, design, fabricate and characterize higher order qL-LWs devices for sensor application in liquid environment. The COMSOL Multiphysics eigenfrequency study is used to obtain the Lamb waves dispersion curves, followed by device level simulation of qL-LWs resonator by frequency domain study and qL-LWs delay line by time domain study. The qL-LWs device based on ST-cut Quartz piezoelectric substrate was fabricated and characterised.

The experimental results agreed with the FEM simulation where it is found that the higher order S_1 and A_1 modes have dominantly longitudinal displacement components, thus the acoustic energy doesn't attenuate to the liquid environments.

Aiming for device miniaturisation and for achieving GHz operating frequency range, the study of higher order qL-LWs is extended to composite thin film membranes consisting of a non-piezoelectric and a piezoelectric layer material, such as a-SiC/Zn and SiN/AlN. The theoretical and simulation study shows that higher order qL-LWs can achieve GHz operating frequency and sensitivity much higher than that of the fundamental qL-LW device. Fabrication process flow of SiN/AlN-based qL-LWs devices is developed by direct electron beam lithography (EBL) and direct deposition of a piezoelectric c axis oriented AlN film onto 200 nm thick SiN thin film. The adopted process flow simplifies the fabrication processes as it does not require the back-side etching of the silicon substrate to release the suspended membrane, as used in conventional process flow. This thesis reported a preliminary result of a fabricated higher order qL-LW device based on a SiN/AlN suspended membrane.

Furthermore, the dispersive characteristic of Lamb waves results in a vanishing group velocity condition characterized by a finite phase velocity, thus resulting in a stationary non-propagating mode. An electroacoustic resonator based on a zero-group velocity (ZGV) Lamb mode offers the great advantage to reduce the complexity of the device fabrication technology, since metal strip gratings or suspended edges are no more necessary to confine the acoustic energy. A theoretical and simulation studies of ZGV resonators based on SOI/AlN and a-SiC/ZnO composite thin suspended membranes are reported in this thesis with possible application to gas and pressure sensing.

The overall result of this thesis work will give a new and deeper understanding on the sensing application of devices based on higher order Lamb waves: these applications include gaseous and liquid environment sensing, as well as pressure sensing. Depending on the sensing application, the Lamb waves with the proper characteristics, such as mode shapes and displacement components, can be selected in order to design highly sensitive and low-loss devices. The continuous work on this topic will result in an integrated acoustic waves sensor that can be used for various sensor applications.

TABLE OF CONTENTS

Page

ACKNOWLEDGMENTS iv

ABSTRACT..v

INTRODUCTION 1

1.1 Elastic Wave Propagation in Solids 3
1.1.1 Surface Acoustic Waves 7
1.1.2 Plate Acoustic Waves 8
1.2 Piezoelectricity and Electro-Acoustic Waves 9
1.2.1 Thin Film Bulk Acoustic Resonator 12
1.2.2 Interdigital transducers (IDTs)...15
1.3 Objectives and Organisation of the Thesis 18
Bibliography 18

SAW SENSOR FOR LIQUID ENVIRONMENT: A REVIEW 21

2.1 PSAW and HVPSAW sensors 23
2.2 Love wave sensors 28
2.3 Shear Horizontal Acoustic Plate Mode sensors 35
2.4 Lamb Wave sensors 40
2.4.1 Quasi-longitudinal symmetric modes 42
2.4.1 Fundamental antisymmetric mode 46
Bibliography 53

HIGHER ORDER QUASI-LONGITUDINAL LAMB WAVES: FINITE ELEMENT ANALYSIS...58

3.1 Higher Order Quasi-Longitudinal Lamb Waves in Single Crystal Piezoelectric Materials 60
3.1.1 Eigenfrequency analysis 61
3.1.2 Frequency Domain analysis 66
3.1.3 Time Domain Analysis 67
3.1.4 Liquid Model 69
3.1.5 Viscosity Sensor...70
3.2 Higher Order Quasi-Longitudinal Lamb Waves in Composite Thin Film Membrane 72
3.2.1 a-SiC/ZnO 72
3.2.2 SiN/AlN 79
Bibliography 82

DEVICES BASED ON HIGHER ORDER QUASI-LONGITUDINAL LAMB WAVES:

EXPERIMENTAL RESULT 84

4.1 Microfabrication Techniques 85
4.1.1 Electron Beam Lithography 85
4.1.2 Radio Frequency Magnetron Sputtering 87
4.1.3 Device Fabrication Process flow 90
4.2 Characterisation Result 93
4.2.1 ST-cut Quartz Lamb waves 93
4.2.2 SiN/AlN thin film Lamb waves 95
Bibliography 97

ZERO GROUP VELOCITY LAMB WAVES 98

5.1 Silicon-on-insulator (SOI)/AlN 100
5.1.1 Lamb waves dispersion curves in SOI/AlN 101
5.1.2 Gas Sensing Application...107
5.2 Amorphous Silicon Carbide (a-SiC)/c-ZnO 110
5.2.1 Lamb waves dispersion curves in a-SiC/c-ZnO 111
5.2.2 Pressure Sensing Application 115
Bibliography 125

CONCLUSION 128

6.1 Summary and Contribution..129
6.2 Future Work and Recommendation 130

CHAPTER 1

INTRODUCTION

This chapter starts by introducing the emergence of surface acoustic wave for sensor application, followed by the basic principle acoustic waves and piezoelectric material. The interdigital transducer (IDT) to excite surface acoustic waves (SAW) will be introduced followed by the design of a resonator and delay line. Finally, the objective and the organisation of the thesis are explained.

Related Publications:

Caliendo, C., **M. Hamidullah**, and F. Mattioli. "Finite Element Modeling and Synthesis of c-axis Tilted AlN TFBAR for Liquid Sensing Applications." *Procedia Engineering* 168 (2016): 1032-1035.

The commercial application of electrically excited acoustic (electroacoustic) waves using piezoelectric materials have been started since more than 70 years ago, with the telecommunication industry as the main consumer. Acoustic waves (AW) devices are mainly used as band-pass filters, where annually ~3 billion acoustic wave filters are used in mobile phones. In the early 1980s, the application of AW devices emerged beyond their conventional fields of application, notably as a physical, chemical and biological sensor. Quartz crystal microbalance (QCM) biosensor is firstly reported by Nomura and Minemura in 1980 by employing shear wave mode of bulk acoustic wave (BAW) [1]. The sensor application of acoustic wave is extended to surface acoustic wave (SAW) devices, due to the confinement of the acoustic wave energy onto the surface of the substrate, making the wave extremely sensitive to any surface perturbation. Gas sensing using surface acoustic waves is reported by Martin et al by exciting Rayleigh wave (RW) on thin film ZnO deposited on Silicon substrate [2]. Several other RW sensor applications are reported on various material, such as ST-cut Quartz for humidity sensing [3] and YZ lithium niobate ($LiNbO_3$) for temperature sensing [4], to cite just a few.

However, RW sensor is impractical for sensing applications in liquid environments since the RW has elliptical particle motion, and thus the vertical (out of plane) particle displacement component will be responsible of power dissipation into the liquid [5]. In-plane polarized waves are required for sensing applications in liquid medium. Moriizumi et al demonstrated theoretically and experimentally that the propagation of such waves can be achieved by selection of proper material type, crystal cut, and direction of wave propagation [6]. They concluded that 36°YX lithium tantalate ($LiTaO_3$) substrate supports *leaky* SAWs, which are predominantly shear horizontally polarized surface waves (SHSAW) showing a slightly amount of acoustic energy loss into the bulk of crystal. Since then, the use of SHSAW devices as biosensors was emerging with one of the earliest applications based on the pH change and reported by Kondoh et al [7]. Gizeli et al. demonstrated that enhanced sensor sensitivity can be achieved by covering the surface of the piezoelectric substrate that supports the propagation of surface skimming bulk waves (SSBW), such as Quartz substrate, with a thin layer, such as polymethyl-methacrylate (PMMA) [8] that acts as a guiding layer and traps the wave energy close to the surface. SSBWs have pure shear displacement component, and travel slightly below the surface of piezoelectric substrate [9]. A thin PMMA layer onto the surface of the piezoelectric substrate that sustains the SSBW propagation will convert the SSBW into a guided shear horizontal surface wave, named Love modes (LM) [10].

Currently, the research works on acoustic wave devices for both telecommunication and sensor applications are shifting toward plate acoustic waves (PAWs), that travel in finite thickness plates, as opposed to the SAWs that travel onto the surface of half-spaces. The interests are motivated by the requirement of achieving ultra-high frequency (UHF) devices for application in the GHz range telecommunication, and for the development of enhanced higher sensors sensitivity. Shear horizontal acoustic plate mode (SHAPM) [11] and fundamental antisymmetric [12] and symmetric [13] Lamb modes are the two most common PAW that are used for sensing application.

The present chapter will start with the fundamental concepts of the acoustic waves propagation in bulk materials, half-space and finite thickness plates.The used of interdigitated transducer (IDT) to electrically excite the elastic waves propagation in piezoelectric substrates will be discussed in the two cases where 1. the IDT acts as a single transducer in the resonator design; 2. a couple of IDTs act as the transmitting and receiving IDTs in the delay line design. Finally, the last subchapter will describe the organization and the objective of this thesis.

1.1 Elastic Wave Propagation in Solids

The history of research in acoustic wave field is started by the theoretical work of wave propagation in solid that is linked with the development of the theory of elasticity in nineteenth century [14]. In the early twentieth century, the research works were primarily concerned with and influenced by the fields of seismology and geophysics, with specific discoveries by scientists such as Rayleigh, Lamb and Love [15]. The term of bulk acoustic wave (BAW) is used to describe the elastic waves propagating in an unbounded, homogeneous medium and they are categorized into a longitudinal wave and transverse wave as shown in figure 1.1a and 1.1b respectively [16].

In an isotropic media, that have only two 2 independent variables (i.e. elastic constants) in their stiffness and compliance matrices (as opposed to the 21 elastic constants in the general anisotropic case), the phase velocity of the bulk longitudinal wave, V_l , and bulk transverse wave, V_t, are given by:

$$V_l = \sqrt{c_{11}/\rho} \tag{1.1}$$

$$V_t = \sqrt{c_{44}/\rho} \tag{1.2}$$

where c_{11} and c_{44} are the bulk and shear modulus respectively, and ρ is the mass density of the material.

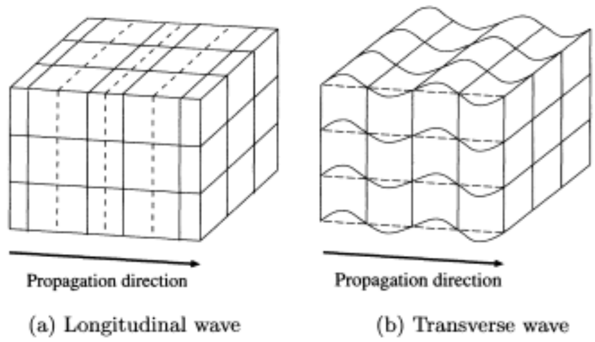

Figure 1.1: (a) Bulk Longitudinal and (b) Transverse wave

In an anisotropic media, the BAW phase velocities are also dependent on crystal orientation and direction propagation, thus the velocity equation is becoming more complex. Christoffel developed mathematical formulae to compute the phase velocities in anisotropic media, known as Christoffel equation. This equation was derived combining the equation of motion:

$$\rho \ddot{u}_i = \frac{\partial}{\partial x_i} \sigma_{ij} \tag{1.3}$$

and the Hooke's Law,

$$\sigma_{ij} = c_{ijkl} e_{kl} \tag{1.4}$$

So that equation (1.3) can be rewritten as:

$$\rho \ddot{u}_i = c_{ijkl} \partial_j \partial_l u_k \tag{1.5}$$

by defining the displacement as

$$\vec{u} = \vec{g} e^{i\omega(t - \vec{s}.\vec{x})} \tag{1.6}$$

where

$\vec{g}$ is the polarization direction

$\vec{s}$ is the slowness vector

$\vec{x}$ is the position vector

the equation (1.3) can again be rewritten as:

$$\rho g_i = g_k c_{ijkl} s_j s_l \tag{1.7}$$

or

$$(c_{ijkl} s_j s_l - \rho\ \delta_{ik}) g_k = 0 \tag{1.8}$$

Finally, normalizing the elastic moduli tensor by the density

$$\frac{c_{ijkl}}{\rho} = \Gamma_{ijkl} \tag{1.9}$$

And define the Christoffel Matrix

$$M_{ik} = \Gamma_{ijkl}\ \hat{s}_j \hat{s}_l \tag{1.10}$$

to arrive to Christoffel equation.

$$(\Gamma_{ijkl} s_j s_l - c^2\ \delta_{ik}) g_k = 0 \tag{1.11}$$

where c is the phase velocity.

The equation (1.11) is a general equation and the anisotropy will be introduced via the elastic moduli tenor in the Christoffel Matrix. Furthermore, the equation is an eigenvalue problem: solving it will yield three phase velocities (the eigenvalues) corresponding for the three bulk waves (the longitudinal and the two transverse bulk waves, named hereafter as slow and fast transverse waves), V_l , V_{sslow} and V_{sfast} . To each eigenvalue an eigenvector corresponds that represents the polarization vectors of the wave. A MATLAB program was written to rotate the material constants according to the selected Euler angles (by using the Bond matrices method outlined in Auld's book), and then solving the Christoffel equations for different direction of propagation. The 3D plot of the BAWs velocities were obtained for both isotropic and anisotropic materials. As an example, the V_l ,

V_{sslow} , and V_{sfast} for isotropic amorphous silicon (a-Si) and anisotropic single crystal (100) silicon are shown in figure 1.2(a) and 1.2(b) respectively. As shown in figure 2(a), the phase velocities are equal for any direction, while in figure 2(b), the phase velocities are dependent on the direction of propagation.

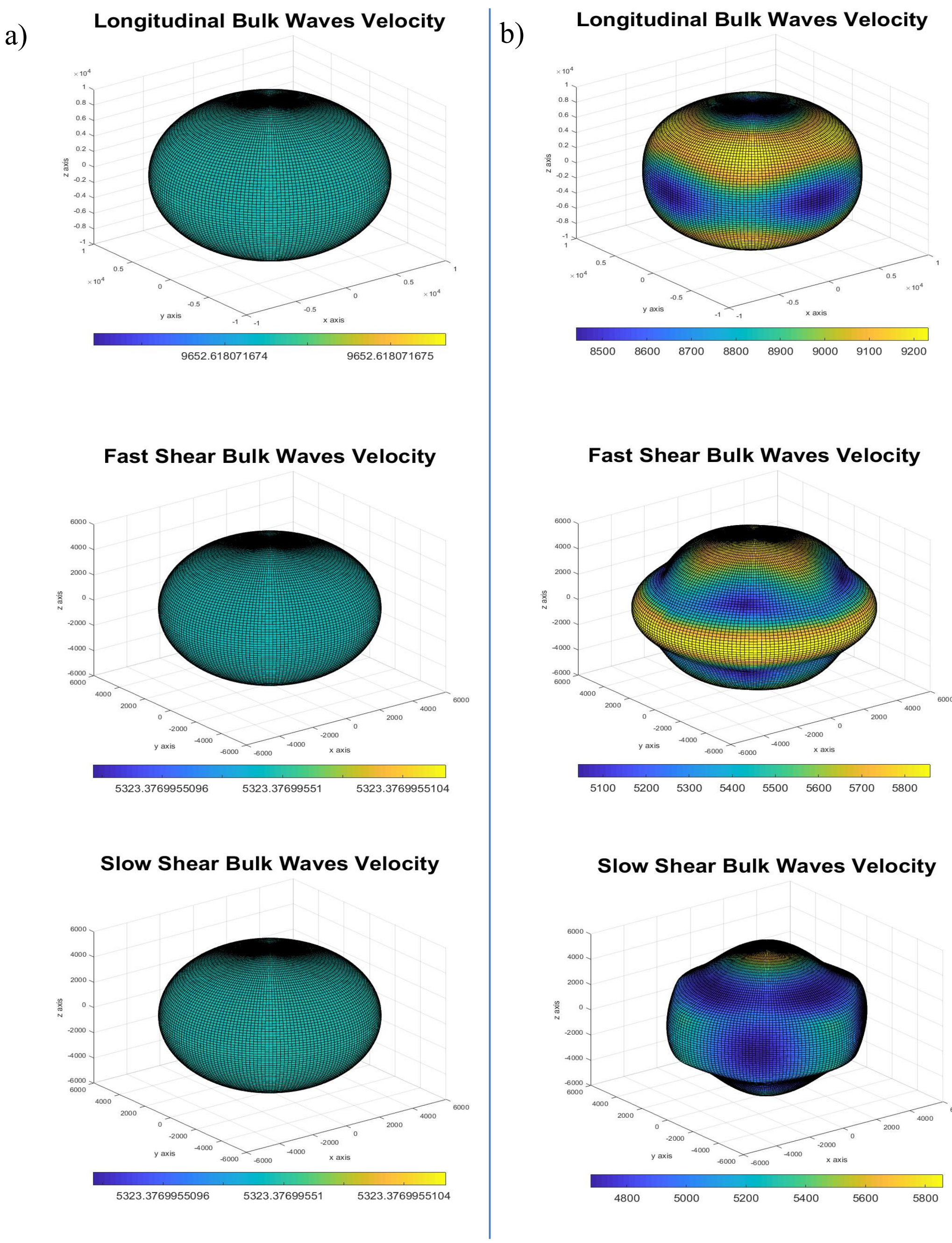

Figure 1.2: Bulk acoustic wave in a) isotropic amorphous-Silicon and b) anisotropic single crystal Silicon (100)

1.1.1 Surface Acoustic Waves

Stimulated by the problem of seismic shock propagation in the earth's crust, Lord Rayleigh described, predicted and later observed experimentally, a type of wave that travels near the surface of solids in 1885, which later named after himself (17). The Rayleigh wave (RW) was modelled based the radius of the earth is much larger than the wavelength of seismic disturbance, thus the problem was simplified by considering the elastic wave guided on the surface of an infinite half space. In isotropic solids, RWs are elliptically polarized in that they have two surface particles displacement components, normal to the surface (U_3) and parallel to the direction of propagation (U_1) as shown in figure 3(a). However, the structure of the earth is more complex thus other types of seismic wave can exist. In 1911, A.E.H. Love described the mathematical model for the propagation of horizontally polarized shear waves (SH waves), that exist only in the presence of a semi-infinite medium covered by an upper layer of finite thickness; these waves were later named as Love waves or Love modes (LM) [18], as shown in figure 1.3(b). LM travel with a lower velocity than P- or S-waves, but faster than Rayleigh waves. These waves are observed only if the layer has a shear velocity lower than that of the semi-infinite substrate. The Love waves have in plane particle displacement component only, that is orthogonal to the direction of propagation, and the particle motion is restricted to the layer depth and decay exponentially into the depth of the half-space, as shown in figure 1. 3(b).

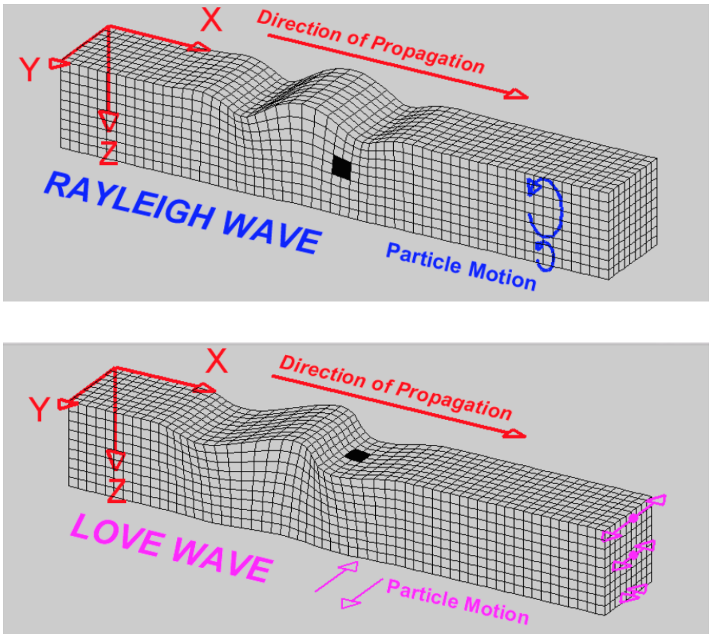

Figure 1.3: Surface Acoustic Wave (a) Rayleigh and (b) Love Wave

It has been suggested that as the elastic anisotropy of the Earth's crust is relatively small, thus both earlier work on RW and LM were not considering the anisotropy of the material. Other than Lord Kelvin who began to investigate wave propagation in anisotropic media and reproduced Christoffel's findings in 1904 [19], little work was conducted on wave propagation in anisotropic in the early 20th century. Only later in the 1950s, the interest on acoustic wave propagation on anisotropic media was revived due to the development of piezoelectric transducers and ultrasonic nondestructive evaluation (NDE) methods. In 1959, Buchwald was the first researcher to perform a detailed investigation of waves propagating from a point-force in an anisotropic elastic solid [20] Furthermore, many more works were reported by considering the piezoelectricity effect [21-22]. The piezoelectricity effect will be described in the later sub-section of this chapter.

1.1.2 Plate Acoustic Waves

While the *SAW* acronyms is used to describe the acoustic wave travelling along the surface of semi-infinite medium, the term plate acoustic waves (PAW) is used to describe the acoustic wave travelling along a finite thickness medium. The former waves have one traction free surface, while the latter waves have two surfaces with traction-free boundary conditions. Horace Lamb described in 1911 a simple case of an elastically isotropic plate where an infinite set of waves that can exist [23] showing two particle displacement components, U_1 and U_3, longitudinal and shear vertical, named Lamb modes. These modes are divided naturally into two infinite sets of modes, *symmetric* and *antisymmetric*: as an example, figure 1.4(a) and (b) shows the field profile of the fundamental modes, A_0 and S_0. The Lamb waves are dispersive, since their velocity depends on the plate thickness value. The dispersion curves of the Lamb modes can be obtained by solving the Christoffel and the boundary conditions equations, which will be described with more details in the chapter 3.

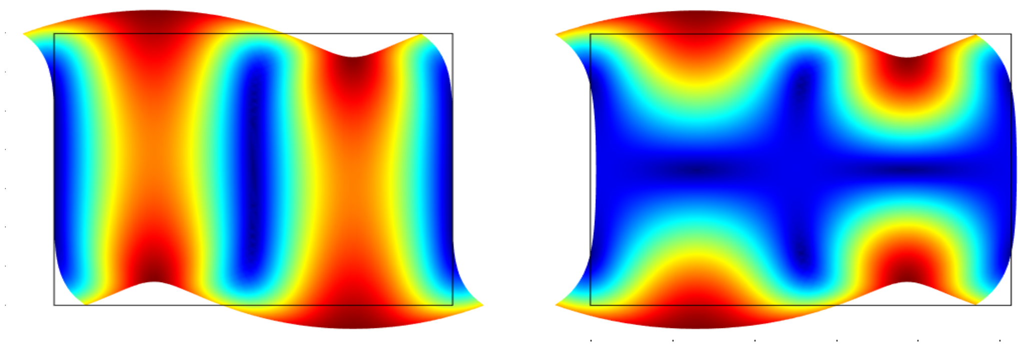

Figure 1.4: (a) Symmetric and (b) Antisymmetric Lamb Waves

Another type of PAW is called *shear horizontal acoustic plate modes* (SHAPM) [24]. While Lamb waves in isotropic plate have two particle displacement components, the SH-APMs have only one particle displacement component shear horizontally polarized, normal to the direction of propagation, as shown in figure 1.5. As well as for the Lamb modes, the absence of a surface normal component of displacement allows each SHAPM to propagate in contact with a liquid without coupling excessive amount of acoustic energy into the liquid, which will be described more detail in chapter 2.

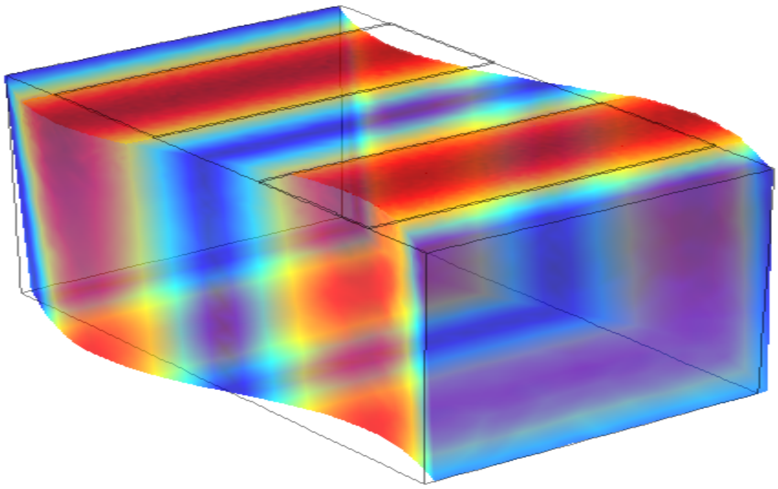

Figure 1.5: Shear Horizontal Acoustic Plate Mode

1.2 Piezoelectricity and Electro-Acoustic Waves

The piezoelectric effect was discovered by brothers Pierre and Paul-Jacques Curie in 1880 [25]. A material is piezoelectric if it results electrically polarized when subjected to a mechanical stress; vice versa , when subjected to an electric field, the piezoelectric material generates a strain that changes the structure of the material itself, as shown in figure 1.6. The two phenomena are called direct and the inverse piezoelectric effects.

The relationship between the electric and mechanical components can be described by the following equations

$$T = c^E S - eE \tag{1.12}$$

$$D = eS + \varepsilon^S E \tag{1.13}$$

where T= [T11 T22 T33 T23 T13 T12] is the stress vector (T_{ij} is the i-th stress component normal to the j surface, for i,j =1, 2, 3), S = [S11 S22 S33 S23 S13 S12] is the displacement vector ($S_{ij} = \partial U_i/\partial x_j$, being U_i the displacement component along x_j), D=[D1 D2 D3] is the electrical displacement vector, E=[E1 E2 E3] is the electric field vector, c^E is the 6x6 elastic constants matrix for a constant electric field, e is the 3x6 piezoelectric constants matrix, ε^s is the 3x3 dielectric constants matrix. Equation 1.12 and 1.13 expresses the linear dependency of the stress components T with respect of the electric field E and the strain components S. Likewise, the electric displacement D is determined by the electric field E and the permittivity tensor for constant strain ε^S. In equation 1.13 one can observe that for the constant piezoelectric coupling tensor e, the electric displacement has a linear distribution with respect to the stress.

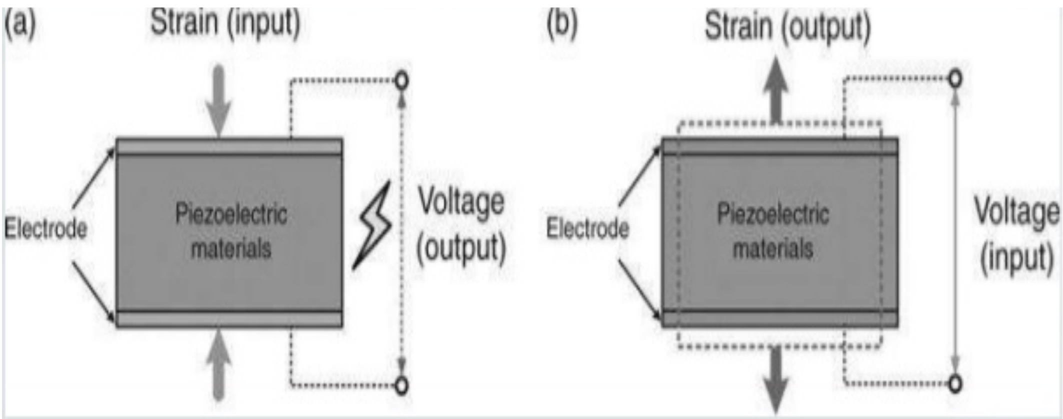

Figure 1.6: (a) Direct piezoelectic and (b) inverse piezoelectric effects.

Due to the piezoelectric effect, the solution of the equations of motion is becoming more complex than that of the nonpiezoelectric materials because the additional term of electric displacement *D* must be also considered. One method to simplify the analysis is by using the *Quasistatic Approximation* method [10]. In this method, a new set of elastic module tensor is used, which is called *piezoelectrically stiffened elastic constant* $c^E{}_{ijkl}$. By using the piezoelectrically stiffened constants $c_{ij}^{stiff} = c_{ij} - {e_{ik}e_{kj}}/{\varepsilon_{kk}}$, the same form as Christoffel equation is used to calculate the three *piezoelectrically stiffened bulk longitudinal waves velocities,* $V^E{}_l$, $V^E{}_{sslow}$ *and* $V^E{}_{sfast}$. A MATLAB program was written to calculate the velocities of the BAWs travelling in lithium niobite ($LiNbO_3$) along different propagation directions, as shown in figure 1.7.

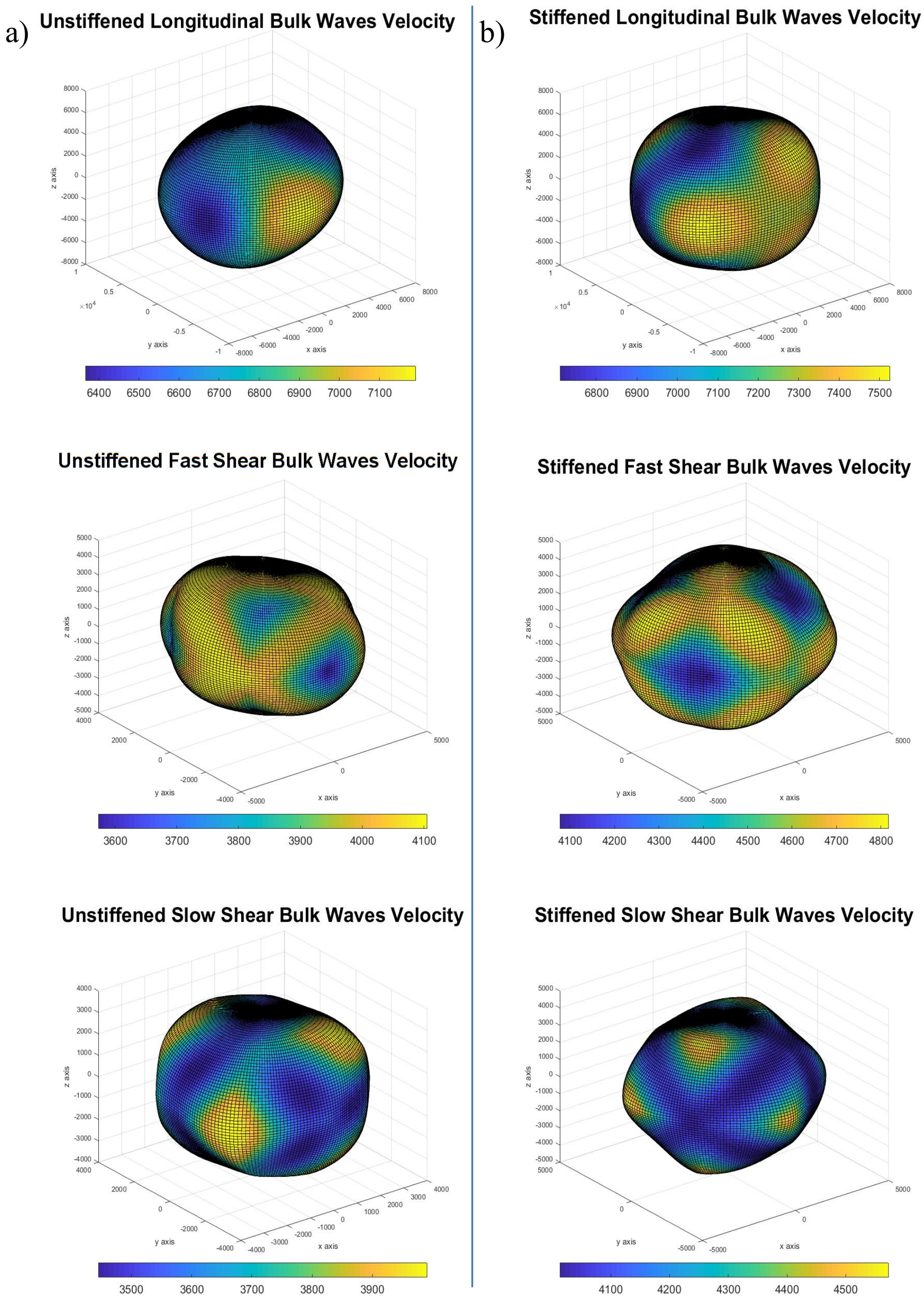

Figure 1.7: X-cut Lithium Niobate(a) unstiffened b) stiffened bulk acoustic waves

Another important parameter in the application of piezoelectric material for electroacoustic wave is the electromechanical coupling coefficient K^2, which is defined as numerical measure of the conversion efficiency between electrical and acoustic energy in piezoelectric materials. In Quasitatic approximation, the K^2 can be approximated as:

$$K^2 = \left(\frac{{V^E}^2 - V^2}{V^2}\right) \qquad (1.14)$$

where V^E and V are the stiffened and unstiffened bulk acoustic wave velocities, respectively. The K^2 of the three BAWs was calculated for $LiNbO_3$ by a Matlab program: V and V^E are the BAWs velocity calculated by considering the unstiffened and stiffened elastic constants of the $LiNbO_3$ in the Christoffel equation. Figure 1.8 shows the 3D plot of the K^2 of the three BAWS travelling in $LiNbO_3$.

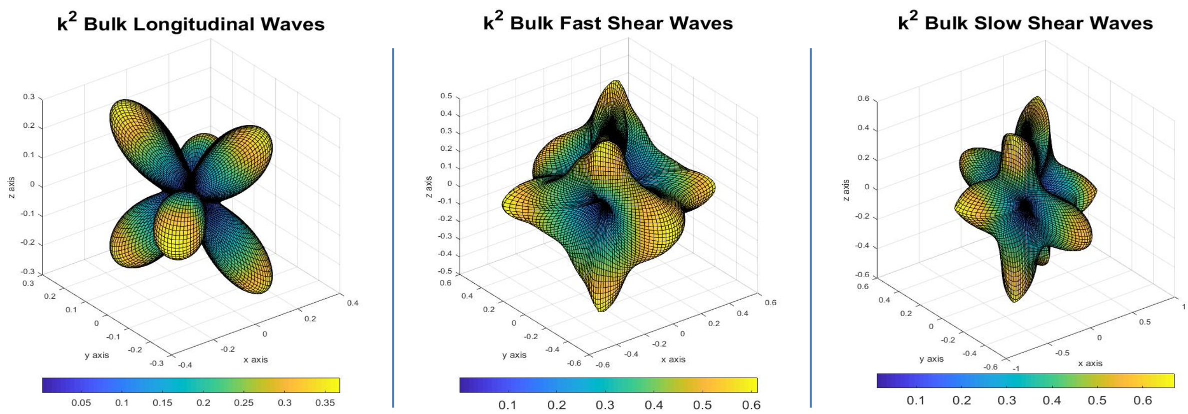

Figure 1.8: K^2 of the BAWs travelling in Lithium Niobate

1.2.1 Thin Film Bulk Acoustic Resonator

The thin film bulk acoustic resonator (TFBAR) is one example of BAW-based device. It consists of a piezoelectric material (with thickness equal to half wavelength) sandwiched between two metal electrodes as shown in figure 1.9. A common application of FBARs is the radio frequency (RF) filter for use in cell phones and other wireless applications. Aluminum nitride (AlN) and zinc oxide (ZnO) are two common piezoelectric materials used in TFBAR; as their thicknesses is of several micrometers, they resonate in the frequency range of hundreds MHz to GHz. The resonance frequency f_o of the TFBAR is dependent on the phase velocity of the BAW modes excited by the applied electric field and the wavelength, which is two times of thickness d of the film.

$$f_o = \frac{V_{ph}}{2d} \qquad (1.15)$$

Figure 1.9. the TFBAR schematic

Moreover, the crystallographic cut of the piezoelectric material will decide the type of BAW modes that can be electrically excited, depending on the value of electromechanical coupling constant K^2. Furthermore, the thickness of the electrodes will also contribute to the total thickness, hence to the resonance frequency of the TFBAR. We reported the theoretical and simulation study of TFBAR based on piezoelectric AlN thin film [26] for different c-axis tilt angles. The FBAR based on c-axis oriented AlN has non-zero K^2 only for longitudinal BAW. However, when the c-axis of AlN thin films is tilted to certain angle μ with respect to the surface normal, the non-zero K^2 of one of the transverse BAW (fast shear BAW) appears. The velocity v and K^2 of the BAWs propagating along AlN substrate were theoretically calculated for different c-axis tilt angle and the results are shown in figs. 1.10a and b. TFBAR behaves as a single-mode resonator for certain μ values, such as 0° and 65° for the longitudinal resonance modes. For all the others μ values the TFBAR behaves like a dual mode resonator, but the μ = 30° tilt angle seems to be the optimized angle for improved operation of shear mode resonators.

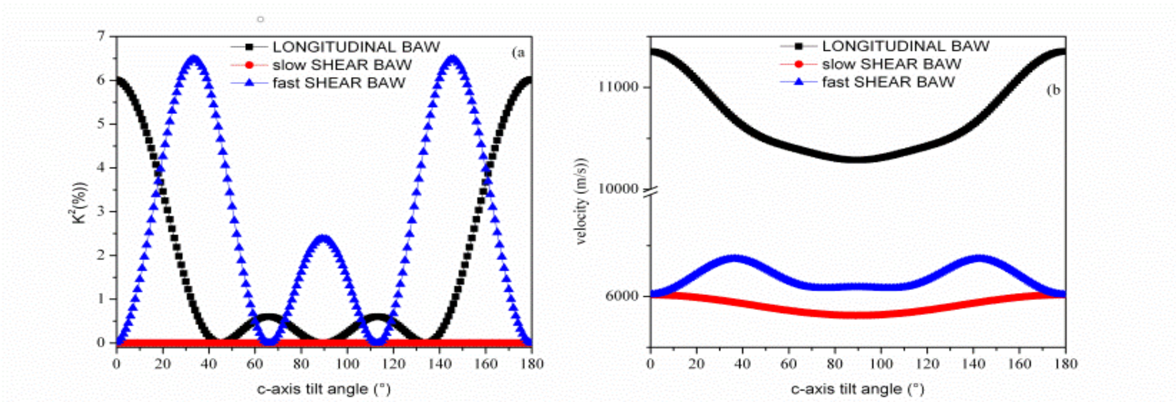

figure 1.10 (a) coupling coefficient K^2 (b) acoustic wave velocity v angular dispersion curves.

The piezoelectric film thickness d, as well as the BAWs v and K^2 are important parameters for the TFBAR design: the former affects the operating frequency f=v/2d, while the latter affects the quality factor Q. TFBAR based on c-axis tilted AlN, molybdenum top and bottom electrodes and a bottom silicon nitride suspended layer was simulated using COMSOL Multiphysics: Figure 1.11(a) shows the simulated structure and the reference coordinated system (x_1, x_2, x_3). To account for the tilted c-axis and the wave propagation direction along x_3, the x_2 axis was set out of plane with rotation angle about x_2 axis. Perfectly matched layer (PML) was applied in left and right side of the structure to prevent wave reflection. The particle displacement of the longitudinal and shear BAW (LBAW and SHBAW) is along the x_3 and x_1 directions. COMSOL frequency domain simulation was performed with 20° tilt angle and the dual mode frequency behaviour was achieved as shown in figure 1.11(b).

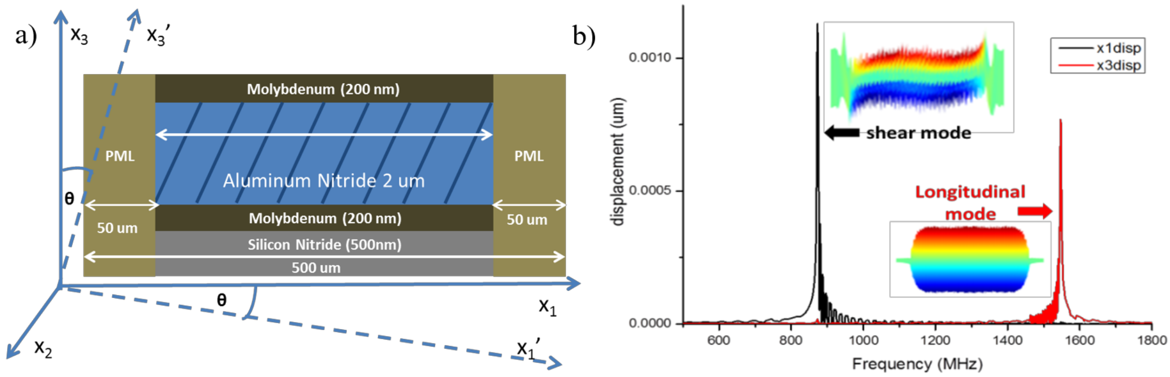

figure 1.11 (a) TFBAR simulation structure and (b) longitudinal and shear mode displacement at 20 degree c-axis tilt angle

The TFBAR first frequency response has only one particle displacement component along x_1 which indicated a shear mode where the second frequency response has only x_3 particle displacement component which indicated a longitudinal mode. The longitudinal mode frequency is expected to be higher than that of the shear mode because the LBAW has higher velocity than that of the SHBAW. The TFBAR admittance was simulated for different μ values to observe the effect of the tilt angle on the TFBAR resonant frequency f, modulus of impedance and Q. As shown in the figure 1.12(a), for μ = 0° there is only a longitudinal mode that propagates at f = 1543 MHz; the shear mode appears for μ = 15° at f = 873 MHz. The highest impedance modulus for the shear mode is at 30° tilt angle with a resonant frequency equal to 874 MHz. At 45° tilt angle, the resonant frequency reduces back to 873 MHz and its impedance modulus becomes lower than that of the 30°degree tilt angle. The simulation results agree with the theoretical calculations shown in figure 1.10 where, at 30° tilt angle, the shear mode has the highest coupling coefficient and velocity.

Further simulation was performed with different Mo thickness from 50 nm to 200 nm at fixed tilt angle (μ = 30°). As the frequency is inversely proportional to the total thickness of TFBAR including AlN, Mo electrodes and SiN, an increased resonant frequency is expected for thinner metal electrodes. As shown in figure 1.12(b), the Mo electrode thickness affects the performances of the SH mode resonator. With reducing the Mo electrode thickness, the shear mode resonant frequency increases from 874 to 1120 MHz, and the impedance modulus at resonance also increases; these two effects result in an enhanced sensitivity of the sensor. The growth of c-axis tilted AlN thin layer with RF magnetron sputtering technique will be demonstrated in chapter 4 of this thesis.

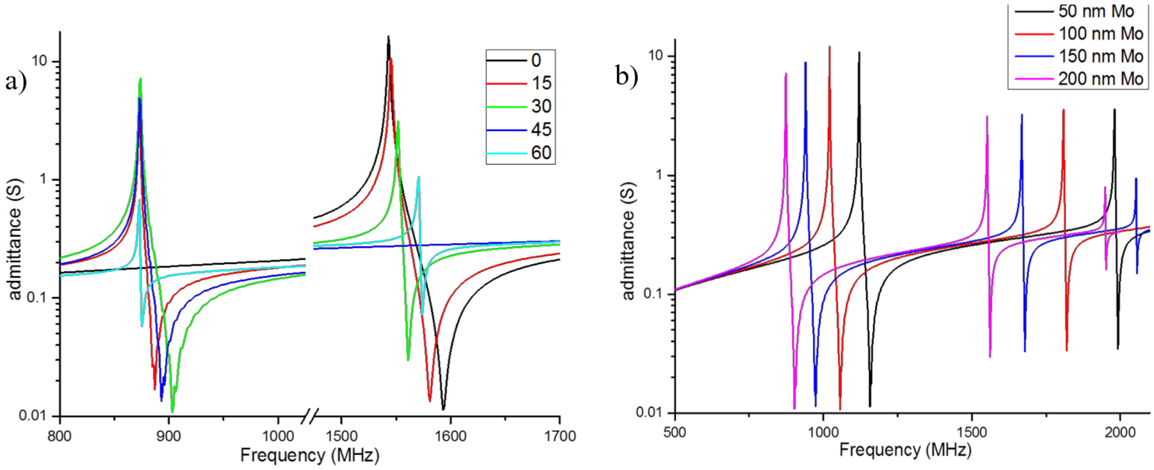

Figure 1.12 TFBAR longitudinal and shear horizontal modes at (a) various tilt angles and (b) various Mo thicknesses

1.2.2 Interdigital transducers (IDTs)

The interdigital transducers (IDT) are metal electrode used to generate and detect SAW on the surface of piezoelectric crystals, and are designed as a comb-like metal structure (electrodes), as shown in Figure 1.13

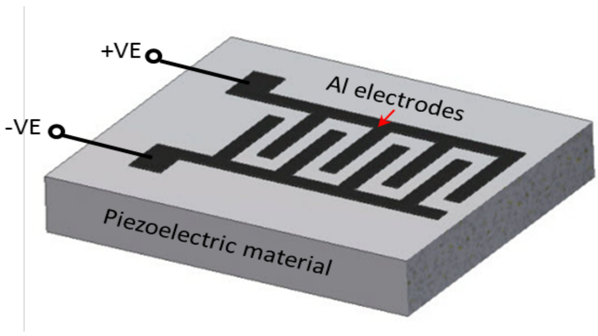

Figure 1.13: Schematic representation of an IDT structure.

An applied voltage between alternating electrodes causes a periodic electric field imposed on the crystal (Figure 1.14(*a*) and (*b*)). This generates a periodic strain field in the piezoelectric crystal that produces a standing SAW. This standing wave gives rise to propagating waves that are launched by the bidirectional emitting IDT in both directions away from the transducer, with the wave fronts being parallel to the transducer electrodes.

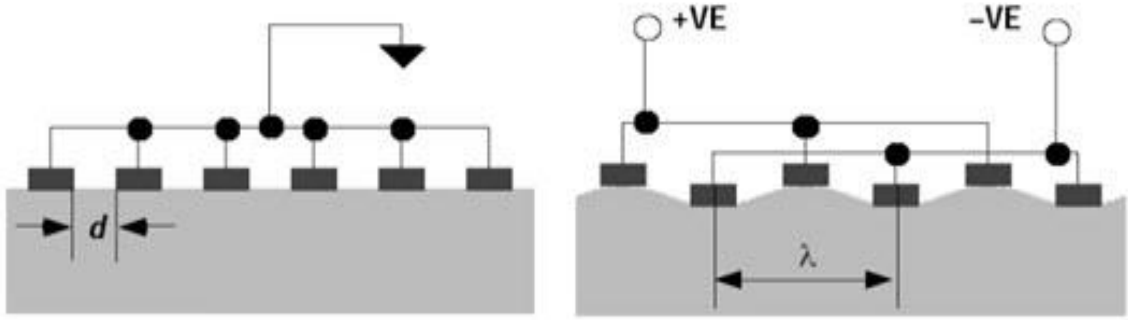

Figure 1.14: Schematic representation of the voltage applied to the IDTelectrodes (*a*) and the induced displacement field (*b*) [27].

When the IDT is placed in between two reflecting grating structures (Figure 1.15 (*a*)) the acoustic wave launched by the transducer is reflected back and a standing wave pattern is created. Such structure generates a resonance and can be used for oscillator applications. A two-port SAW Resonator has a pair of IDT's which are placed in between the reflectors thus resulting in a similar resonance as one port resonator (Figure 1.15 (*b*)). The two-port resonator can be also looked at as kind of a very narrow, low loss band-pass filter.

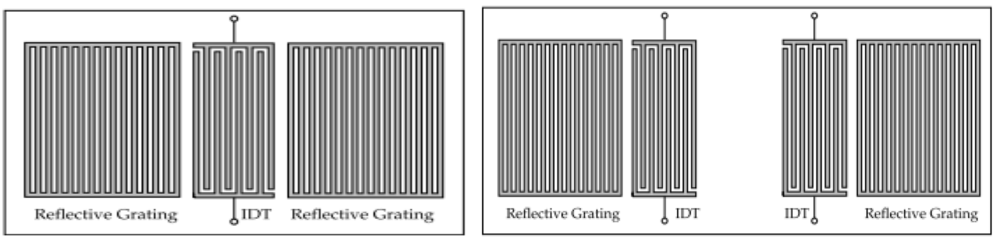

Figure 1.15: Schematic representation of one-port resonator (*a*) and a two port resonator (*b*) [28].

The basic SAW delay line device consists of a piezoelectric substrate, an input and an output IDT on the same side of the substrate, as shown in figure 1.16 [29].

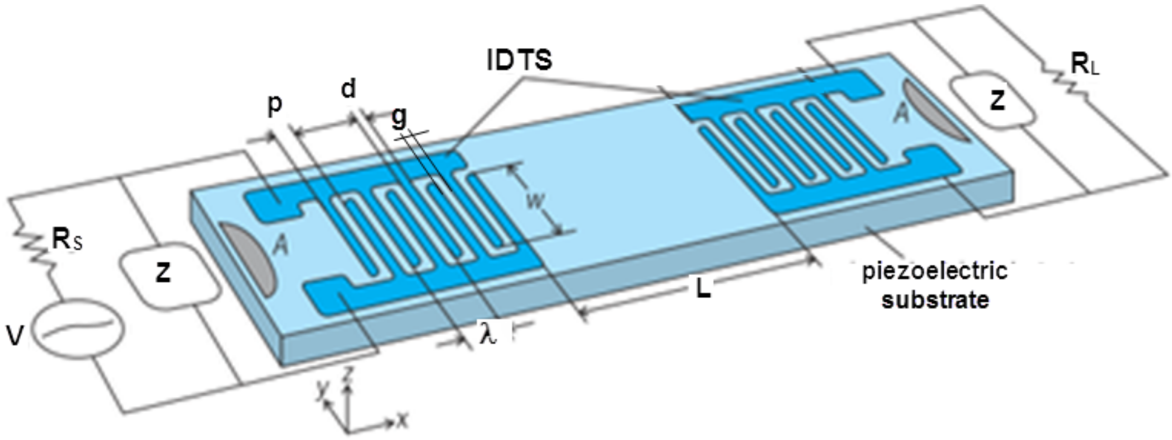

Figure 1.16: Schematic picture of a SAW device [29]

The centre frequency of the delay line in Figure 1.16 can be determined by the following equation:

$$f_o = \frac{v}{\lambda} = \frac{v}{2p} \quad (1.15)$$

where f_0 is the centre frequency, v is the acoustic wave velocity, λ is the wavelength and p is the acoustic pitch. For standard structures as shown in Figure 2.1, p is defined by the total width of gap g and electrode d as following equation:

$$p = d + g \quad (1.16)$$

The bandwidth of signal (BW) is in inverse proportion to the number of fingers pair N_p of the IDTs as shown in below:

$$BW \sim \frac{1}{Np} \quad (1.16)$$

The IDT aperture W (the IDT fingers overlapping) will affect the diffraction of the SAW signal. The necessary aperture required to prevent diffraction effects should be at least 20 times larger than the wavelength.

The thickness of the electrodes, h, should be thick enough to give low electrical resistance but thin enough to prevent the mass loading effect. Typically, h = 100nm for aluminium electrodes [20].

1.3 Objectives and Organisation of the Thesis

The final goal of this thesis is to extend the knowledge of SAW sensors beyond the current state of the art, more specifically by exploiting the higher order Lamb waves for sensor application. The higher order modes will provide several advantages, such as shorter wavelength that results in higher resonance frequency; multiple modes with different characteristics can be utilized for different sensing applications. More emphasize will be given for higher order quasi longitudinal Lamb waves, that are suitable for liquid environment applications, followed by zero group velocity Lamb wave resonators and their application for gas and pressure sensing.

The thesis is organized in six chapters. **The present chapter** introduces the basic principles of the propagation of different types of acoustic waves (BAW, SAW, and PAW), and describes the resonator and delay line IDTs configurations.

Chapter 2 gives an in-depth review of the current state of the art of SAW and PAW sensors for liquid environments.

Chapter 3 is devoted to the finite element simulation method of higher order quasi-longitudinal Lamb waves in single crystal ST Quartz substrate and composite thin film consisting of piezoelectric and non-piezoelectric thin film.

Chapter 4 describes the fabrication process and the characterization of the higher order quasi-longitudinal Lamb waves in single crystal ST Quartz substrate and composite SiN/AlN thin film.

Chapter 5 provides the theoretical and finite element analysis of zero group velocity Lamb wave resonators and their potential application for gas and pressure sensing.

Chapter 6 presents the conclusion of the thesis and the suggested future works.

Bibliography

[1] Nomura, T. and Minemura, A. (1980) Behavior of a Piezoelectric Quartz Crystal in an Aqueous Solution and the Application to the Determination of Minute Amount of Cyanide. Chemical Society of Japan, 10, 1621-1625.

[2] Martin, S. J., et al. *Gas sensing with surface acoustic wave devices*. No. SAND-84-2436C; CONF-850685-2. Sandia National Labs., Albuquerque, NM (USA), 1985.

[3] Caliendo, Cinzia, et al. "Organometallic polymer membrane for gas detection applied to a surface acoustic wave sensor." Sensors and Actuators B: Chemical 25.1-3 (1995): 670-672.
[4] Viens, Martin, and J. David N. Cheeke. "Highly sensitive temperature sensor using SAW resonator oscillator." Sensors and Actuators A: Physical 24.3 (1990): 209-211.
[5] Calabrese, Gary S., Hank Wohltjen, and Manas K. Roy. "Surface acoustic wave devices as chemical sensors in liquids. Evidence disputing the importance of Rayleigh wave propagation." Analytical Chemistry 59.6 (1987): 833-837.
[6] Moriizumi, T., Y. Unno, and S. Shiokawa. "New sensor in liquid using leaky SAW." *IEEE 1987 Ultrasonics Symposium*. IEEE, 1987.
[7] Kondoh, Jun, Yusuke Matsui, and Shigeki Shiokawa. "SH-SAW biosensor based on pH change." *Ultrasonics Symposium, 1993. Proceedings., IEEE 1993*. IEEE, 1993.
[8] Gizeli, Electra, et al. "A Love plate biosensor utilising a polymer layer." *Sensors and Actuators B: Chemical* 6.1 (1992): 131-137. 54
[9] Gizelli, E., et al. "Surface skimming bulk waves: a novel approach to acoustic biosensors." *Solid-State Sensors and Actuators, 1991. Digest of Technical Papers, TRANSDUCERS'91., 1991 International Conference on*. IEEE, 1991.
[10] Auld, Bertram Alexander. *Acoustic fields and waves in solids*. Рипол Классик, 1973.
[11] Martin, S. J., et al. "Characterization of SH acoustic plate mode liquid sensors." Sensors and actuators 20.3 (1989): 253-268.
[12] sensor antisimetric lamb
[13] sensor asimetric lamb
[14] Love AEH (1944) A treatise on the mathematical theory of elasticity, 4th edn. Dover Publications, New York
[15] Achenbach JD (1975) Wave propagation in elastic solids. Elsevier Science Publishers B. V, Amsterdam
[16] Hashimoto, Ken-ya. "Bulk Acoustic and Surface Acoustic Waves." Surface Acoustic Wave Devices in Telecommunications. Springer, Berlin, Heidelberg, 2000. 1-23.
[17] Rayleigh, Lord. "On waves propagated along the plane surface of an elastic solid." Proceedings of the London Mathematical Society 1.1 (1885): 4-11.
[18] Love, Augustus Edward Hough. Some problems of geodynamics. Cambridge University Press, 2015.
[19] Kelvin L (1904) Baltimore lectures on molecular dynamics and the wave theory of light. C. J.Clay and Sons, London
[20] Buchwald, V. T. "Elastic waves in anisotropic media." *Proc. R. Soc. Lond. A* 253.1275 (1959): 563-580.
[21] Hutson, A. R., and Donald L. White. "Elastic wave propagation in piezoelectric semiconductors." Journal of Applied Physics 33.1 (1962):
[22] Slobodnik Jr, A. J., and J. C. Sethares. "Elastic, Piezoelectric, and Dielectric Constants of Bi12 GeO20." Journal of Applied Physics 43.1 (1972): 247-248.
[23] Lamb Lamb, Horace. "On waves in an elastic plate." Proc. R. Soc. Lond. A 93.648 (1917): 114-128.

[24] Martin, S. J., et al. "Characterization of SH acoustic plate mode liquid sensors." Sensors and actuators 20.3 (1989): 253-268.
[25] Manbachi, Amir, and Richard SC Cobbold. "Development and application of piezoelectric materials for ultrasound generation and detection." Ultrasound 19.4 (2011): 187-196.
[26] Caliendo, C., M. Hamidullah, and F. Mattioli. "Finite Element Modeling and Synthesis of c-axis Tilted AlN TFBAR for Liquid Sensing Applications." Procedia Engineering 168 (2016): 1032-1035.
[27] B. Drafts, "Acoustic Wave Technology Sensors," *Sensors Magazine,* vol. 17, 2000
[28] D. P. Morgan, *Surface acoustic wave filters: with applications to electronic communications and signal processing*: Academic Press, 2007.
[29] .Mauder, "SAW gas sensors: comparison between delay line and two port resonator," Sensors and Actuators B: Chemical, vol. 26, pp. 187-190, 1995.

CHAPTER 2

SAW SENSOR FOR LIQUID ENVIRONMENT: A REVIEW

This chapter gives a topical in-depth review on SAW sensor for liquid environment, including Pseudo and High Velocity Pseudo SAW (PSAW and HVPSAW), Love waves, SH-APM, and Lamb waves.

Related Publications:

Caliendo, C and **M. Hamidullah** "SAW sensors for liquid environments: a review" *Journal Physics D (under revision)*

Caliendo, Cinzia, and **Muhammad Hamidullah.** "A theoretical study of love wave sensors based on ZnO–glass layered structures for application to liquid environments." Biosensors 6.4 (2016): 59.

Book Chapter

C. Caliendo, **M. Hamidullah**. "Sensors and Applications in Measuring and Automation Control Systems (Book Series: Advances in Sensors: Reviews, Vol. 4)– Chapter 6, P. 121-131.Editor: Sergey Y. Yurish – Publisher: International Frequency Sensor Association (IFSA) Publishing – ISBN: 978-84-617-7596-5

The basic structure of a Surface Acoustic Wave (SAW) sensor includes a piezoelectric substrate and a pair of interdigitated transducers (IDTs) photolithographically patterned onto the free surface of the piezoelectric wafer [1]. The transmitting IDT converts an electrical signal to elastic waves that travel along the substrate surface; the receiving IDT converts the substrate mechanical stress in an electrical signal. The piezoelectric substrate can be a *bulk* single crystal substrate (such as quartz, lithium niobate or lithium tantalate to name just a few), with thickness H much higher that the acoustic wavelength λ (H >> λ), or a *thin film* (such as ZnO or AlN) with thickness H < λ, grown onto a non-piezoelectric *bulk* substrate (such as silicon, sapphire, glass, or diamond, to cite just a few). In SAW devices, the acoustic wave travels along the surface of the propagating medium and its energy is confined one wavelength in depth; it follows that the SAW characteristics (wave velocity and amplitude) are highly affected by any physical and chemical changes that occur at the propagating medium surface and/or at the adjacent medium when the SAW device interacts with the external environmental stimuli (such as humidity, temperature, pressure, and viscosity, to cite just a few). The wave characteristics can be perturbed by the changes of the electrical (conductivity and permittivity) and mechanical (mass density and viscosity) properties of the liquid contacting the sensor surface, or by the anchorage of a mass onto the sensing layer surface, at the presence of a liquid environment.

The environment interacts with the SAW directly or by means of a thin surface *sensing* layer that, for some specific applications, covers the wave propagation path between the two IDTs and is in direct contact with the environment to be tested. If the membrane is an insulating material, it can cover the entire SAW device surface, including the IDTs, while if it is conductive, it is positioned in between the two IDTs. Therefore, part of the SAW energy is distributed into the sensing layer and any change in its physical properties affects either or both the wave velocity and propagation loss, giving rise to a detectable output signal (a frequency and/or insertion loss shift) that represents the sensor response. The sensing layer affinity towards a specific target analyte is a fundamental prerequisite as it can drive the sensor selectivity towards a specific application. In gas sensing applications, the interactive membrane can be a thin Pd film [2,3], a thin lead phthalocyanine (PbPc) film [4] a graphene-like nano-sheet [5], a calixarene layer [6] or a polyethynyl-fluorenol layer [7] to cite just few examples, to detect H_2, NO_2, carbon monoxide, organic vapors or simply the relative humidity of the of the surrounding environment. In liquid phase sensing applications, the interactive membrane can be poly(isobutylene) (PIB), poly(epichlorohydrin) (PECH), or poly(ethyl acrylate) (PEA) to test toluene, xylenes, and ethyl benzene solutions [8], or polysiloxane film containing acidic functional groups for detection of organic amines in aqueous phase [9], or macrocyclic calixarenes for the detection of organic pollutants in drinking water [10]. The SAW sensors described in [11] were fabricated and derivatized with a rabbit polyclonal IgG antibody, which selectively binds to E. coli O157:H7. A dual channel SAW biosensor for the simultaneous detection of Legionella and Escherichia coli was fabricated using a novel protocol of coating bacteria on the sensor surface prior to addition of the antibody [12.]. Reference [13] presents an overview of 20 years of worldwide development in the field of biosensors based on special types of SAW devices that permit the highly sensitive detection of biorelevant molecules in liquid media.

Whatever the sensing layer is, it is important to underline that the design of the device can significantly affect the performances of the sensor since its sensitivity is also dependant on their wave-type and polarization, on the electroacoustic coupling configuration, on the materials thickness and crystallographic orientation. The present chapter gives a survey of the SAW sensors design for liquid environmental applications. Sensors based on the propagation of elastic waves propagating along *half-spaces* and finite thickness *plates* are presented, such as shear horizontal SAWs (Pseudo SAW, PSAW), high velocity pseudo SAWs (HVPSAWs), Love wave modes (LMs), shear horizontal acoustic plate modes (SHAPMs) and Lamb wave modes (LWs).

2.1 PSAW and HVPSAW sensors

Pseuso SAW (PSAW) and high velocity PSAW (HVPSAW) are surface acoustic waves that travel near the free surface of an half-space and satisfy the traction-free boundary condition. As opposed to the SAWs that exhibit three particle displacement components that decay with depth, they have both decaying and radiating components; the latter component radiates power into the half-space, thus resulting in an attenuation of the field amplitudes as the wave propagates. If the contribution from the radiating terms is sufficiently small, these two pseudo waves are observed as in standard SAW devices. The PSAW usually has the U_2 component as the dominant component while the HVPSAW usually has the longitudinal component U_1 as the dominant term [14]. For specific crystallographic cuts and wave propagation directions in the most common piezoelectric substrates, piezoelectrically active PSAWs and HVPSAWs travel with minimum propagation loss and, since they are both in-plane polarized, they are suitable to work in contact with liquid. 3D eigenfrequency FEM analysis was performed using COMSOL Multiphysics® Version 5.2 to explore the field shape of the SAW, PSAW and HVPSAW travelling along the ST-x quartz substrate (Euler angles 0° 132.75° 0°) with an Al IDT, as shown in figure 2.1.

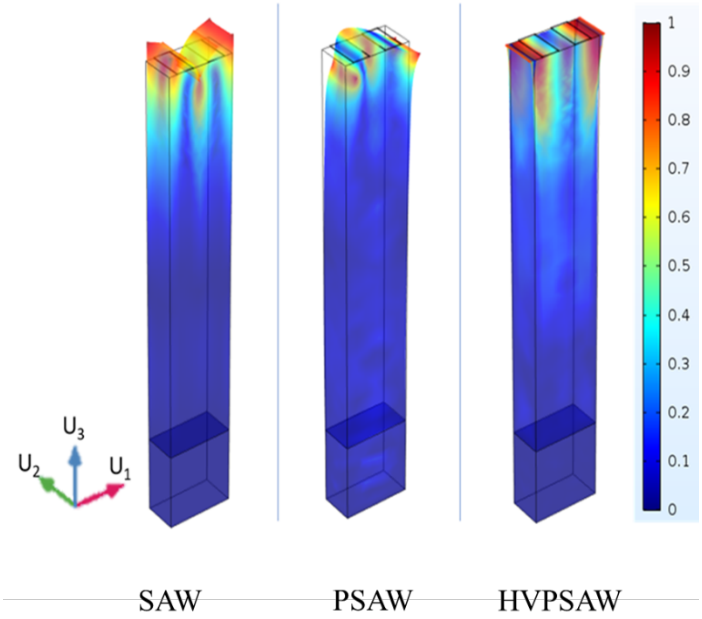

Figure 2.1: The field profile of the SAW, PSAW and HVPSAW travelling along the ST-x quartz substrate in air.

The primitive SAW cell is a single wavelength (λ) cell with two periodic and two continuity boundary conditions applied on the sidewalls. A perfectly matched layer (PML) at the bottom is introduced to simulate the halfspace. In these specific simulations $\lambda = 20$ µm resulting in an IDTs pitch of $p = 5$ µm. The Al thickness was set to $h_{Al} = 0.1$ µm, and the Al strip width to spacing ratio to 1. The colour density is representative of the relative particle displacement and it can be clearly observed that, unlike what happens for the SAWs, the particle motion of the PSAW and HVPSAW is contained in the surface plane of the propagating medium. The PSAW and HVPSAW travel at velocity higher than that of the SAW and close to that of the transverse and longitudinal bulk acoustic wave, respectively: the superior phase velocity of these waves makes it possible to increase the operating frequency without decreasing the wavelength.

The sensors based on PSAWs and HVPSAWs can measure the mechanical (mass density and viscosity) and electrical (conductivity and relative permittivity) property changes of the liquid that contacts the wave path directly, without covering the sensor surface with any selective film. The sensor surface is in direct contact with the liquid test bath whose extent greatly exceeds the penetration depth of the wave mode excited by the IDTs. The sensor response is caused by the mechanical and electrical boundary conditions changes resulting from the changes the of properties the adjacent medium undergoes. If the wave propagation path is metallized and electrically shorted, only the liquid mechanical properties will affect the sensor response, as only the particle displacement component interacts with the adjacent liquid. If the bare path is in direct contact with the liquid, the sensor will be sensitive also to the electrical properties of the liquid as both the wave electrostatic potential and particle displacement interact with the liquid, and two perturbations occur. The electrical perturbation can be discriminated by detecting differential signals between two delay lines.

Figure 2.2 shows the absolute value of the normalized admittance Y vs frequency curves for the three modes propagating in ST-x quartz in air and in water. Three peaks are clearly visible while the half-space contacts the air (the black curve), corresponding to the SAW, PSAW and HVPSAW whose velocities are 3167, 5083 and 5751 m/s, respectively, evaluated ad $f = v/\lambda$. The PSAW has a propagation loss higher than that of the SAW and HVPSAW [15]. The SAW, which has a large component of displacement normal to the substrate, is completely dampened by the water. The PSAW and HVPSAW, which have strong in-plane motions, show poorly reduced amplitudes when dampened with water.

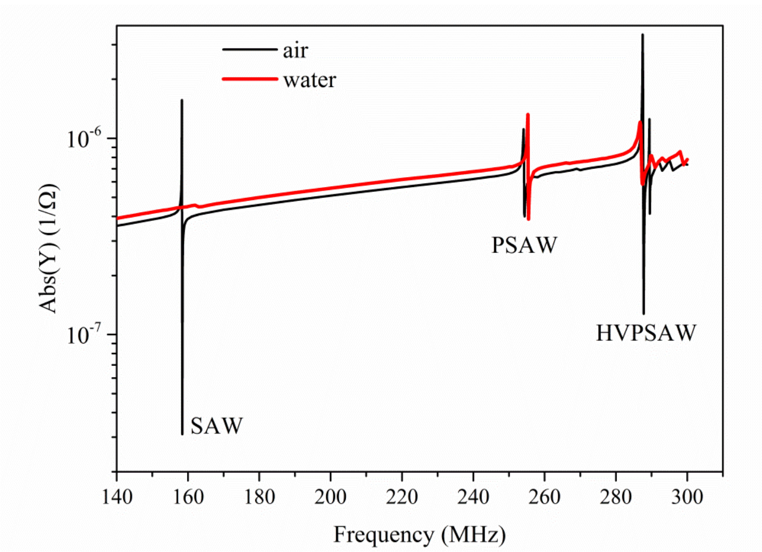

Figure 2.2: The absolute value of the normalized admittance Y vs frequency curves of the SAW, PSAW and HVPSAW travelling along the ST-x quartz substrate in air and in water.

2D COMSOL simulations of the PSAW displacement profile inside the ST-x quartz is plotted in figure 2.3: the blue and the green curves represent the U_2 and U_3 PSAW displacement components; the inset shows the 2D representation of the displacement confinement inside the substrate. The ST-x quartz extends from 0 to 120 μm of the abscissa values, while the liquid half-space extends from 120 to 240 μm abscissa value. The substrate and liquid depth are equal. The liquid was modelled as a linear isotropic viscoelastic material with independent elastic constants, the bulk modulus and the dynamic viscosity, extracted from Reference [16].

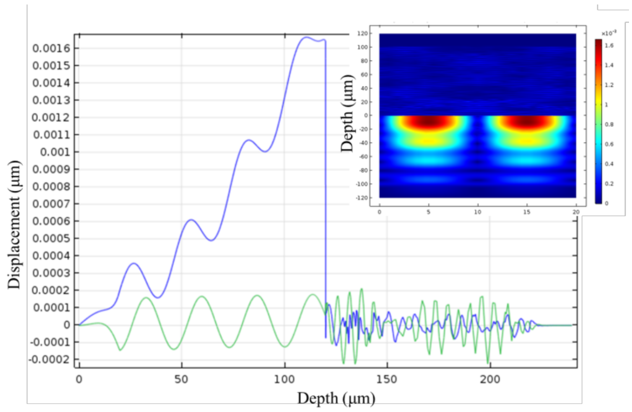

Figure 2.3: the PSAW displacement profile inside the ST-x quartz (from 0 to 120 μm abscissa values) and in water (from 120 to 240 μm abscissa value); the inset shows the 2D representation of the total displacement confined inside the substrate.

References [17-19] provide a very useful list of substrates types and crystallographic orientations along which low-attenuated, strongly-coupled PSAW and HVPSAW travel (such as 64°YX $LiNbO_3$, 36°YX $LiTaO_3$, quartz ST-X, $LiNbO_3$ with Euler angles (90° 90° 36°), (90° 90° 31°) $LiTaO_3$, and (0° 45° 90°) $Li_2B_4O_7$) and also give many information (such as phase velocity, propagation loss, particle displacement components, electroacoustic coupling coefficient K^2 and power flow angle) of the SAW, PSAW and HVPSAW. Moreover, these references also describe the waves behaviour with increasing the thickness of a metallic layer covering the wave propagation path: depending on the layer thickness, the wave diffraction into the bulk can be prevented, as well as the transitions from HVPSAWs to higher order PSAWs modes, and from PSAWs to the GSAWs can be observed. The piezoelectric substrates of the LGX-family group have been studied in references 20,21,22 for application to temperature stable, high coupling, low loss sensors for liquid environments. Several applications of PSAW sensors are presented in the available literature for the measurement of viscosity, electrical properties and mass loading of an adjacent liquid. In reference [23] a sensor for liquid viscosity and conductivity measurement is described that is based on a PSAW dual delay line on 41∘YX $LiNbO_3$ and covered by a SiO_2 protective layer. In reference [24] a PSAW sensor is implemented on 36°-YX $LiTaO_3$ substrate for methanol concentration measurement. In reference [25] the PSAW trapping efficiency of the free, metallized, and grating paths in YX-36° and YX-42° Lithium Tantalate and YX-64° Lithium Niobate are compared at fundamental and harmonic frequencies. A high frequency (>500 MHz) PSAW sensor for liquid environment is designed that show high coupling, low loss, high operating frequency and high resistance to surface contamination.

In reference [26] the propagation of PSAW along bare 41° and 64° $LiNbO_3$, and 36°$LiTaO_3$ substrates is studied and compared with that along the same substrates covered by a thin sputtered glass films to increase the resistance to surface contamination. It was demonstrated experimentally and theoretically that the glass layer does not affect the wave loss but it lowers the temperature stability. Film thickness to wavelength ratio regions were found which represent a good trade-off between lowered temperature coefficient of frequency and a preserved high coupling factor. Sensors of liquid viscosity and mass loading have been demonstrated utilizing the present mode on 36° rotated Y-cut X-propagation $LiTaO_3$ [27]. PSAW delay line designed and fabricated on langasite (LGS), Euler angles (0°, 22°, 90°).

One way to enhance the sensor sensitivity (i.e. i.e. the frequency change per unit incremental change of the measured quantity) is to raise the working frequency: this effect can be obtained by reducing the size of the IDTs metal strips or utilizing the SAW devices based on high velocity acoustic wave modes. The HVPSAWs are attractive for this potential application as they travel at velocity close to the longitudinal BAW velocity. In reference [28] the propagation of HVPSAWs in $LiNbO_3$ has been studied in the range of Euler angles (0°, 0° - 90°, 90°): the corresponding theoretical velocities are between 6700 m/s and 7400 m/s, about twice that of normal surface waves, but the K^2 varies between about 0.14% to 0.5%, much less than that of surface waves. In reference [29] some experiments show that the HVPSAW phase velocity in the direction with Euler angle (0°, 124°, 50°) in quartz reaches 6992 m/s and the propagation attenuation is as low as less than $1 \cdot 10^{-4}$ dB/λ, thus is suitable for liquid sensing applications. In reference [30] the propagation of HVPSAW along a semi-insulating Fe-doped GaN films grown on sapphire substrates is experimentally studied and the small propagation attenuation of the mode when travelling along a liquid/solid interface is demonstrated in glycerol solutions. In reference [31] the propagation loss due to bulk wave radiation of a HVPSAW is reduced by loading the 36°YX -$LiNbO_3$ substrate with a dielectric amorphous AlN thin film with a higher velocity than the substrate. The amorphous AlN layer plays the double role to protect the IDTs patterned onto the 36°YX -LN substrate surface and to enhance the device performances.

2.2 Love wave sensors

Love waves are a type of surface acoustic waves characterized by a shear horizontal particle displacement component U_2 largely dominant over the vertical and longitudinal ones ($U_2 >> U_3, U_1$). The propagation of the Love waves is excited and revealed by means of a couple of IDTs, as for the SAW-based devices. Due to the in-plane polarization, the Love waves, as well as the PSAW and HVPSAWs, are suitable to travel along a surface contacting a liquid environment. In the most general sense, Love waves propagate along the surface of a piezoelectric half-space covered by a thin layer: the substrate is responsible for the excitation of a surface skimming *bulk* wave (SSBW) that propagates below the substrate surface; the thin overlayer traps the acoustic energy and slows down the wave propagation velocity, thus reducing the loss from radiation into the bulk. As a result, the SSBW is converted into a shear *surface* wave, the Love wave. The number of Love modes (LMs) that can propagate in the layer/substrate medium depends on the layer thickness, but he essential condition for the propagation of the Love waves is that shear bulk wave velocity (SHBAW) of the halfspace, v_{sub}^{SHBAW} , is larger than the shear bulk wave velocity of the layer, v_{layer}^{SHBAW} , as the velocity of the Love wave lies in between the v_{sub}^{SHBAW} and the v_{layer}^{SHBAW} [32].

Higher order LMs develop at their respective cut-off frequencies, which are related to the thickness of the layer: at the cut-off the phase velocity of the mode equals the SHBAW velocity of the substrate. As the LM acoustic energy is mostly concentrated inside the guiding layer, the LM-based devices show good performances in terms of sensitivity to any disturbance loading the surface of the guiding layer. A comprehensive review of the Love wave sensors cab be found in Reference [33]. LMs are dispersive as their velocity depends on the layer thickness, other than on the substrate and the layer's material properties. As an example, Figure 2.4 shows the phase velocity dispersion curves of the first five modes (LM1, LM2, LM3, LM4 and LM5) travelling along the ST 90°-x quartz half-space covered by a SiO_2 film. The picture also shows the v_{sub}^{SHBAW} and the v_{layer}^{SHBAW}. The velocity values were numerically calculated by using the McGill software [34].

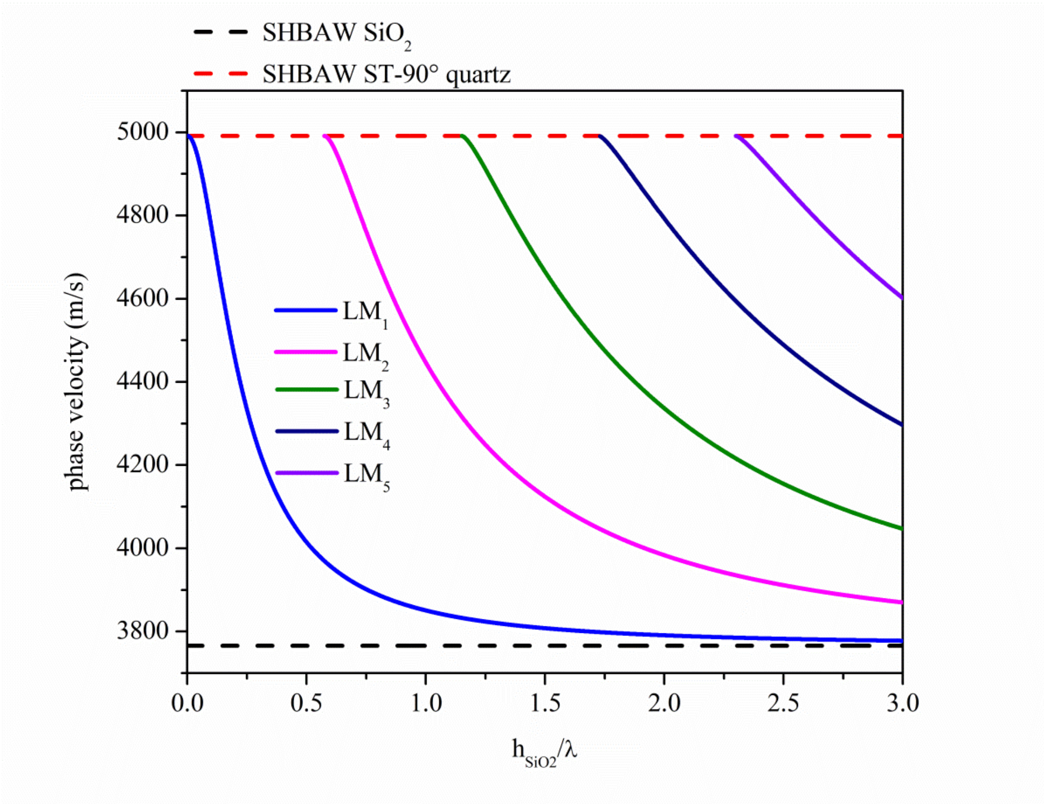

Figure 2.4: The phase velocity vs the layer normalized thickness of the first four LMs travelling in ST 90°-x quartz/SiO_2 substrate.

When the guiding layer is very thin, the velocity of the LM1 tends to the half-space SHBAW velocity; with increasing the layer thickness, the velocity of both the fundamental and higher order modes asymptotically reaches the layer SHBAW velocity. Love waves vanish if the frequency is lower than the cut-off frequency. Figure 2.5(a) and (b) show the time evolution of the SSBW and LM1 total displacement while propagating along the surface of the ST 90°-x quartz half-space, bare and covered by a SiO_2 trapping layer, 2 µm thick, and IDT with λ = 20 µm. The total displacement of the SSBW and LM1 was calculated by 3D COMSOL simulation: the time domain analysis was carried for 20 ns and the total displacement of the propagating medium was recorded at an interval of 1 ns. A bidirectional IDT positioned onto the quartz surface launches two waves in opposite directions: the signal applied at the transmitting IDT was a 10 V peak-to-peak sinusoidal signal at 231 and 217 MHz, for SSBW and LM1. The plot clearly shows that the acoustical displacement propagates into the depth of the substrate for the SSBW while it is more confined to the surface for the LM1.

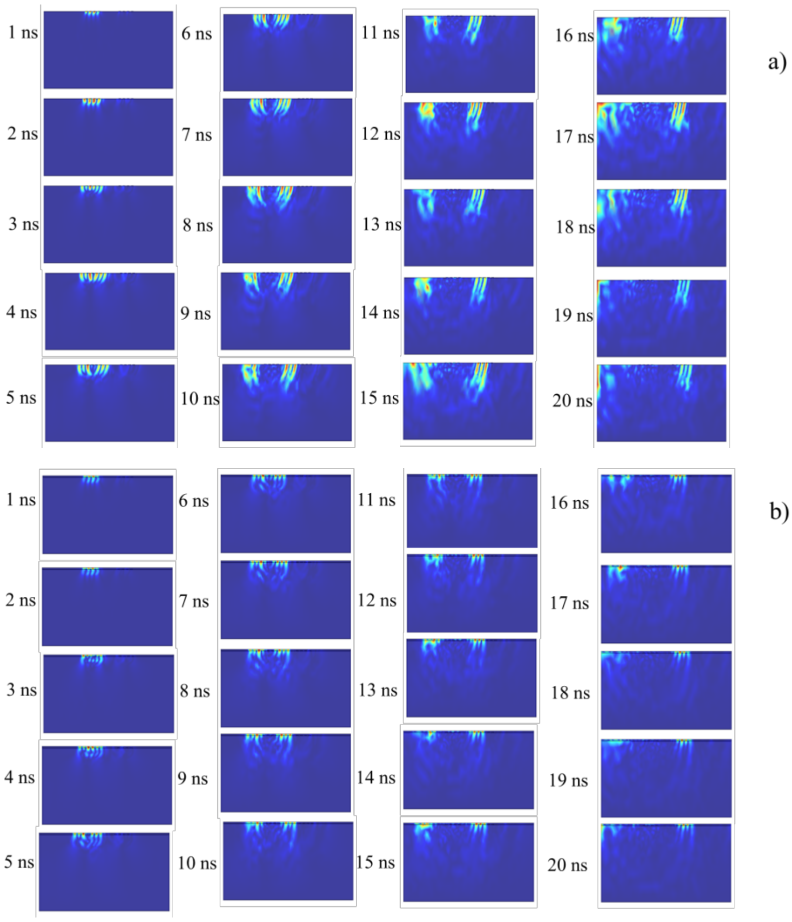

Figure 2.5 The time evolution of the total displacement of a) SSBW and b) LM1; the two waves propagate along the ST 90°-x quartz half-space, bare and covered by a SiO_2 guiding layer, 2 µm thick.

The time and frequency domain response analysis of a delay line based on the SSBW and LM1 propagation was performed by 3D COMSOL simulation assuming a pair of Al IDTs positioned onto the quartz surface; the distance between the transmitting and receiving IDT positioned onto the quartz surface was assumed to be equal to $3 \cdot \lambda$ (active gap region) and the fingers overlap $W = 1 \cdot \lambda$; the substrate propagation loss was not accounted in the calculation. The IDT number of finger pairs N was assumed to be equal to 2 for both the SSBW and LM1 devices. The aluminium electrodes were assumed to be 0.1 µm thick. The electrical voltage at the receiver electrode was recorded for 30 ns in the time domain analysis, as shown in figure 2.6(a) where the ratio V_{out}/V_{in} of the voltage at the receiver and transmitter IDT in time domain is shown. The insertion loss of the delay line is calculated by applying a unit impulse at the input IDT: the Fourier transformation of the device impulse response allowed the calculation of the scattering parameter of the SSBW and LM1 delay line, $S_{21} = 20 \cdot \log(\mathrm{Re}[V_{out}/Vin])$, shown in figure 2.6(b). V_{in} and V_{out} are the voltages at the alternate fingers of the transmitting and receiving IDTs respectively, while the remaining IDTs are grounded. The voltage V_{out} at the output IDT starts to rise in about 11 and 12.5 ns which corresponds to a SSBW and LM1 group velocity of 3636 and 3250 m/s.

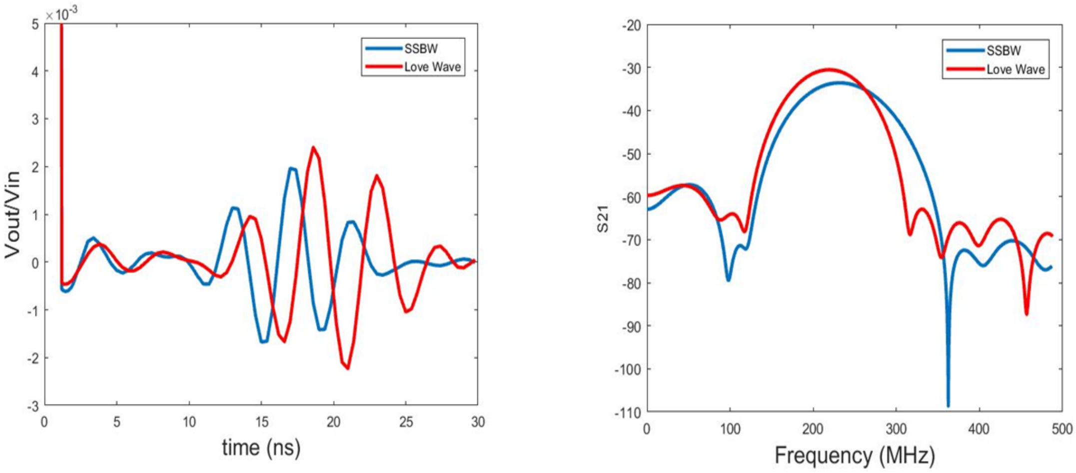

Figure 2.6(a) The ratio V_{out}/V_{in} of the voltage at the receiver and transmitter IDT in time domain; b) the scattering parameter S_{12} vs frequency, for the SSBW- and LM1-based delay line onto the ST-90°x quartz substrate, bare and covered by a SiO_2 guiding layer, 2 µm thick.

The presence of the guiding layer is fundamental to trap the Love wave energy: not any thickness value but a specific one guarantees enhanced device performances (such as minimum delay line insertion loss and maximum gravimetric sensitivity). Figure 2.7 shows the K^2 dispersion curve (the blue curve) and the derivative of the phase and group velocity, v_{gr} and v_{ph} respect to the SiO_2 layer thickness-to-wavelength ratio h_{SiO2}/λ (the black curves) vs the layer normalized thickness of the LM1 travelling along the ST 90°-x/SiO_2 substrate. The $h_{SiO2}/\lambda = 0.07$ corresponds to the maximum K^2; $h_{SiO2}/\lambda = 0.115$ and 0.08 correspond to the maximum mass sensitivity of the phase and group velocity of the LM1, as the derivative of the v_{gr} and v_{ph} is proportional to the gravimetric sensitivity $S_{grav} = \left({}^{\Delta v}/_{v_0}\right)/(\rho \cdot h_{SiO2})$, being ρ and h_{SiO2} the layer mass density and thickness, $\Delta v = v - v_0$, v_0 and v the wave velocity along the bare and covered half-space [35].

Both the LMs group and phase velocity can represent a sensor response: the phase velocity can be experimentally estimated by measuring the operating frequency $f = v_{ph}/\lambda$ of the sensing device at the minimum insertion loss of the scattering parameter S_{12}. The group velocity can be estimated by measuring the group time delay $\tau = L/v_{gr}$ of the sensing device at the minimum insertion loss of the scattering parameter S_{12} in the time domain, being L the acoustic wave delay path [36].

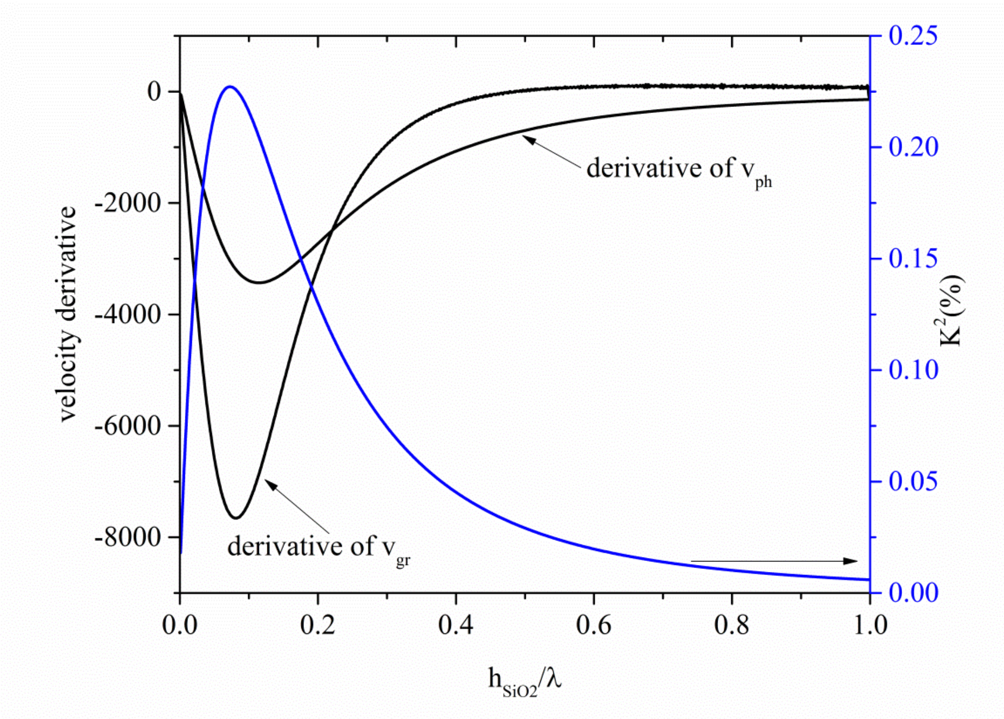

Figure 2.7: The K^2 and the derivative of the phase and group velocity vs the normalized SiO_2 layer thickness, h_{SiO2}/λ, of the fundamental LM1 travelling along the ST 90°-x/SiO_2 substrate.

In the most general cases the LMs devices consist of a semi-infinite piezoelectric substrate (for example 41°YX $LiNbO_3$, 36°YX $LiTaO_3$ and ST-90°X quartz) [37] covered by a thin slowing layer (for example ZnO, Au, PMMA or SiO_2) which traps the propagating wave to the surface of the substrate. The IDTs can be located only onto the piezoelectric substrate surface, under the overlayer, and thus they are isolate from the liquid environment. Table 2.1 lists some practical examples of LM sensors for application to liquid environment.

The LMs also propagate along a non-piezoelectric halfspace (such as Si, glass, BN, a-SiC.) covered by a piezoelectric layer (such as c-axis tilted ZnO or AlN) [36, 45-47]. For example, when the hexagonal ZnO film has its c-axis parallel to the substrate free surface, it is effective in the electroacoustic transduction of LMs in glass/ZnO substrate; when the c-axis is tilted at an angle μ with respect to the normal to the substrate surface, for wave propagation along the <100> direction, two types of surface modes propagate, the LM with predominant shear horizontal polarization, and the Rayleigh-like, with a prevailing sagittal polarization. Both the two modes are coupled to the electric field via the effective piezoelectric constants of the ZnO film. The LM and the SAW play two different roles onto the same sensing platform: the former is suitable for liquid environment characterization, while the latter is suitable for mixing and pumping small liquid volumes. LM sensors implemented on silicon or glass substrate materials offer the great advantage of the sensors integration with the surrounding electronic circuits.

Table 2.1. Some practical examples of LM sensors for application to liquid environment.

substrate	layer	Application	reference
ST-90° quartz	SiO_2	mass sensing in liquids	[38]
ST-90° quartz	PMMA	mass sensing in liquids	[39]
$LiTaO_3$	SiO_2, ZnO, gold, SU-8, and parylene-C	Comparison of electromechanical coupling coefficient, displacement profile and mass sensitivity	[40]
ST-90° quartz	ZnO	liquid viscosity and conductivity	[41]
ST-90° quartz	PMMA	detection of high molecular weight targets in liquid samples	[42]
36°-YX LiTaO3	ZnO	methanol in water	[43]
36°-YX LiTaO3	ZnO	antibody–antigen immunoreactions in aqueous solutions	[44]

The LM sensor based on a piezoelectric layer/non-piezoelectric substrate has a remarkable advantage over the counterpart based on piezoelectric halfspace/non piezoelectric layer, as well as over PSAW and HVPSAW-based sensors: four coupling configurations can be investigated to enhance the K^2 and to take advantage of the protecting role of the guiding layer if the IDTs are buried under it. The IDTs can be positioned at the layer/substrate interface (STF) or at the layer free surface (SFT), with or without a floating metal layer onto the opposite surface of the layer (STFM or SMFT), as shown in figure 2.8

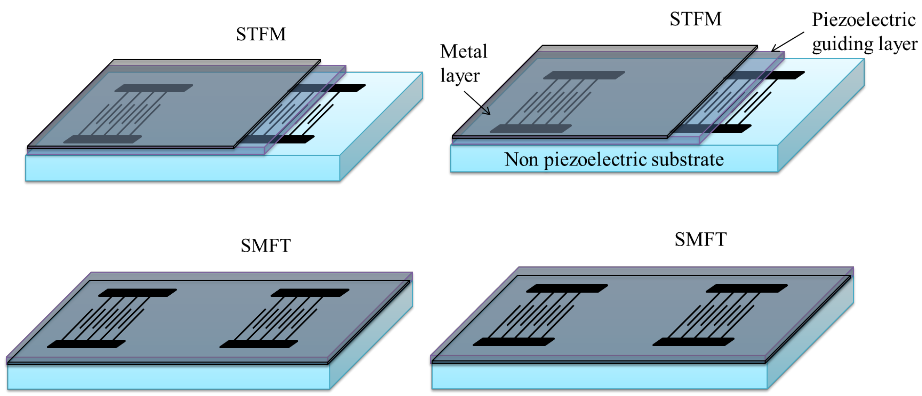

Figure 2.8. The four coupling configurations for the non piezoelectric halfspace/piezoelectric layer structure.

The K^2 of the LM device is affected by the mode order, the crystallographic orientation of both the halfspace and layer, the layer thickness, and also the coupling configuration. As an example, figure 2.9 shows the K^2 dispersion curves for the first Love mode (LM1) in ZnO/glass for the four coupling configurations and different ZnO c-axis tilt angle (from 10° to 90°) [36].

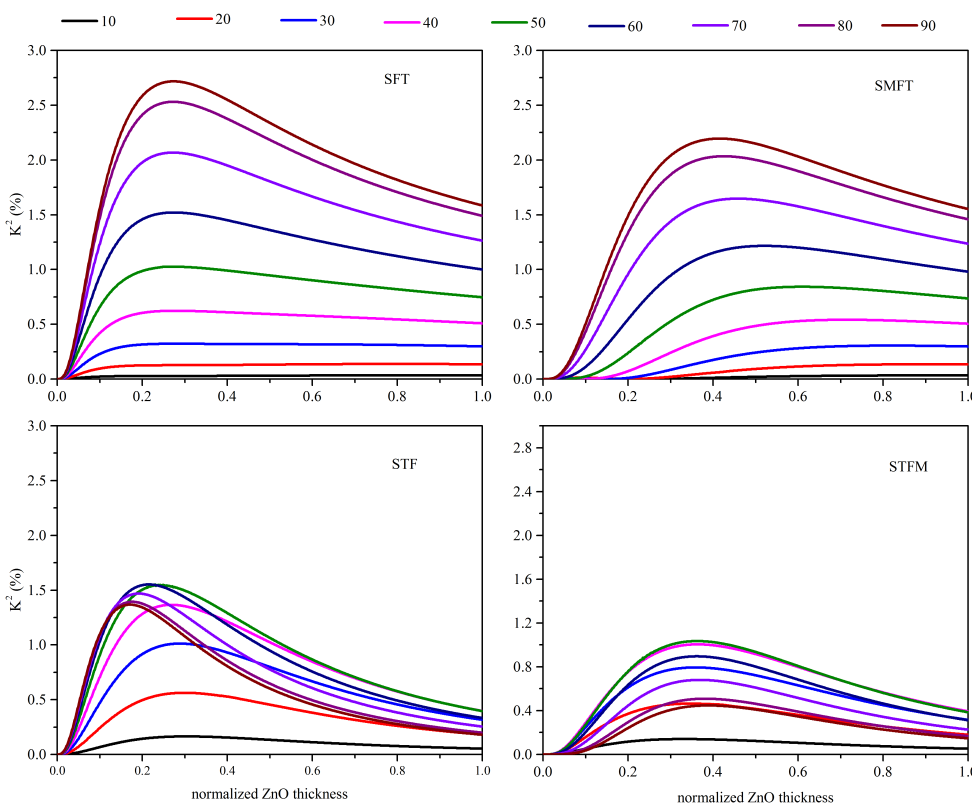

Figure 2.9: The K^2 dispersion curves for the first Love mode in ZnO/glass for the four coupling configurations and different ZnO c-axis tilt angle (from 10° to 90°).

The SFT (SMFT) configuration reaches the highest K^2 values for h/λ~0.3 (0.4) for large tilt angles; the STF and STFM configurations reaches their maximum value (~1.6 and 1.1 %) for 50° tilt angle. As an example, figure 3.9 shows the K^2 dispersion curves for the first four Love modes (LM1, LM2, LM3 and LM4) in 90°-tilted c-axis ZnO/wBN, for the four coupling configurations.

With increasing the Love mode order, ever decreasing K^2 values can be reached by the 4 coupling configurations. The remarkable advantage of the LM-based sensors fabricated onto silicon is the possibility to integrate the sensor with other devices.

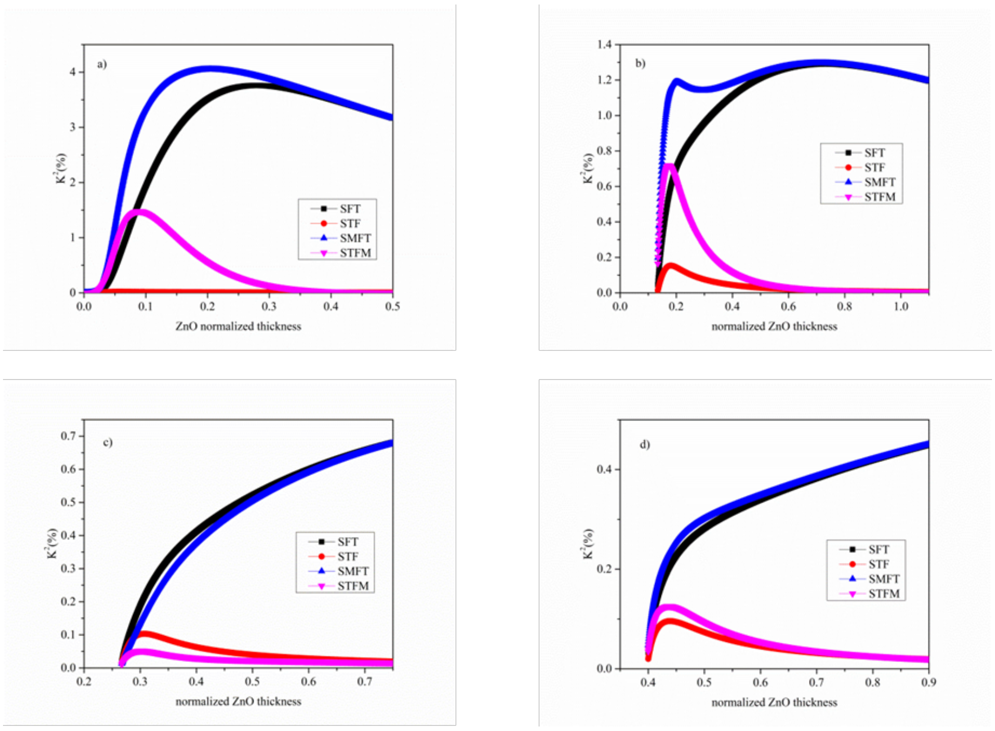

Figure 2.10: The K^2 dispersion curves for the a) LM1, b) LM2, c) LM3 and d) LM4 modes in 90°-tilted c-axis ZnO/wBN, for the four-coupling configuration

2.3 Shear Horizontal Acoustic Plate Mode sensors

Shear Horizontal Acoustic Plate Modes (SHAPMs) are waveguide modes that propagate in finite thickness plates with energy distributed throughout the bulk of the waveguide. The SHAPMs are shear horizontally polarized (U_1, U_3 = 0), hence the absence of the out-of-plane displacement component allows each mode to propagate in contact with a liquid without coupling excessive amounts of acoustic energy into the liquid. 3D eigenfrequency FEM analysis was performed using COMSOL Multiphysics® Version 5.2

to explore the field shape of the SH0, SH1, SH2 and SH4 travelling along the along a GaPO4 piezoelectric plate, 150 µm thick, with Euler angles (0° 5° 90°) and thickness to wavelength ration H/λ = 0.6, as shown in figure 2.11.

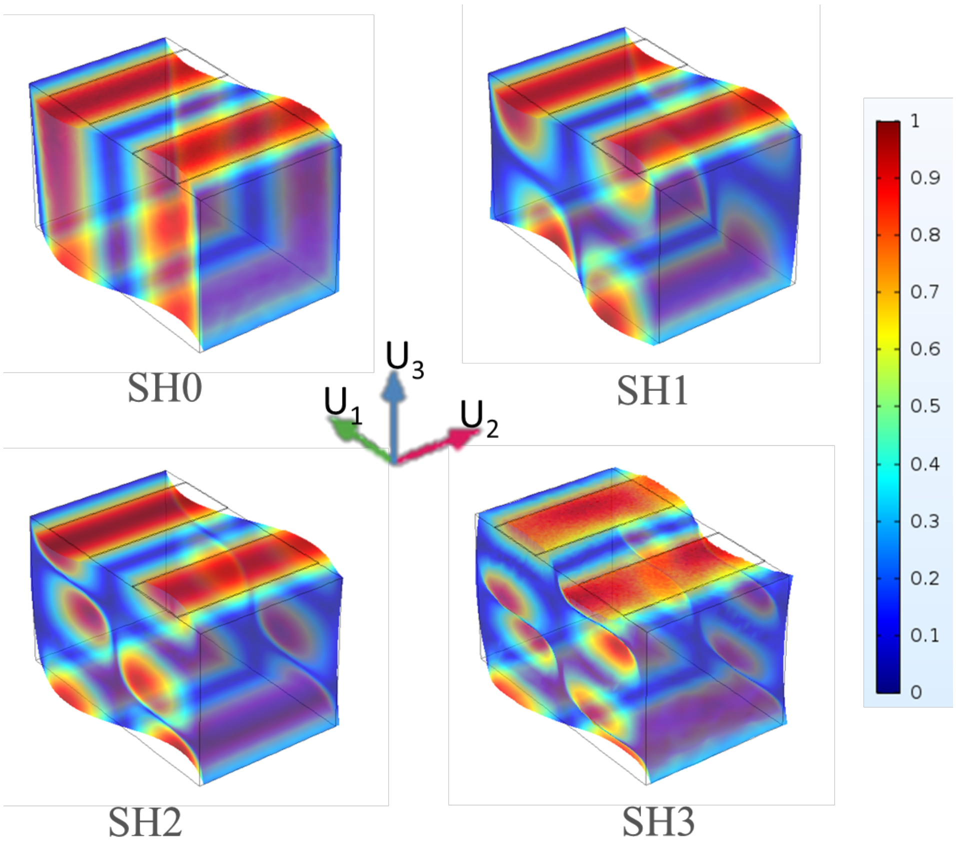

Figure 2.11: The field profile of the first four SHAPMs in $GaPO_4$ piezoelectric plate in contact with air.

The SHAPMs-based device employs input and output IDTs to launch and receive the acoustic wave, like for the SAWs–based devices. These modes energy is distributed between the two plate surfaces as for a standing wave in a BAW sensor but the SHAPMs travel along the plate like a SAW. The continuous exchange of energy between the two plate surfaces allows the signal between the two IDTs to be affected by any changes of the surrounding environment the opposite plate sides undergoes. For liquid sensing applications the plate itself can be employed as a physical barrier between the electronics and the liquid environment to be sensed. The IDTs may be placed on the plate opposite surface from the liquid solution, as shown in figure 2.12: the IDTs are naturally isolated from the (potentially corrosive) aqueous fluid environment without adding any protective layer to the device surface, as for the SAW-based sensors, and taking advantage of the entire sensor surface to maximize the interaction of the wave with the analyte. A metal film can be placed between the input and output IDTs to cancel any direct electromagnetic feedthrough. A sensing layer may be attached to the upper side of the plate that is selectively sensitive to a specific measurand contained into the test liquid solution contacting the sensor. Any interaction (mechanical and/or electrical) between the measurand and the sensing layer will cause a shift in the attenuation and/or velocity of the wave, which represent to the sensor response.

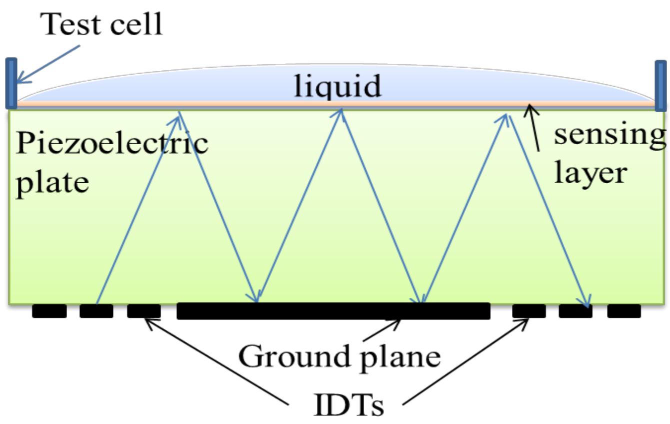

Figure 2.12: The schematic of the SHAPMs sensor.

The number of modes that propagate along the plate is dependent on the normalized thickness H/λ of the plate; the modes are excited at frequency $f_n = v_n/\lambda$ where v_n is the velocity of the n-th mode corresponding to the selected H value. As an example, Figure 2.13 shows the phase velocity dispersion curves of the SHAPMs travelling along an y-rotated $GaPO_4$ plate with Euler angles (0° 1° 90°); the data were obtained by using the McGill software [34]. As it can be seen, the fundamental mode, SH0, is a low-dispersive symmetric mode that travel at velocity equal to the transverse BAW velocity; the higher order modes can be symmetric and anti-symmetric: they are highly dispersive and their velocity asymptotically reaches the shear BAW velocity with increasing the plate thickness; they have a cut off thickness: below the cut-off frequency, the mode becomes evanescent, i.e., the wavenumber is imaginary. Higher order modes can reach very high velocity as near the cut off the slope of the dispersion curves is near to be infinite.

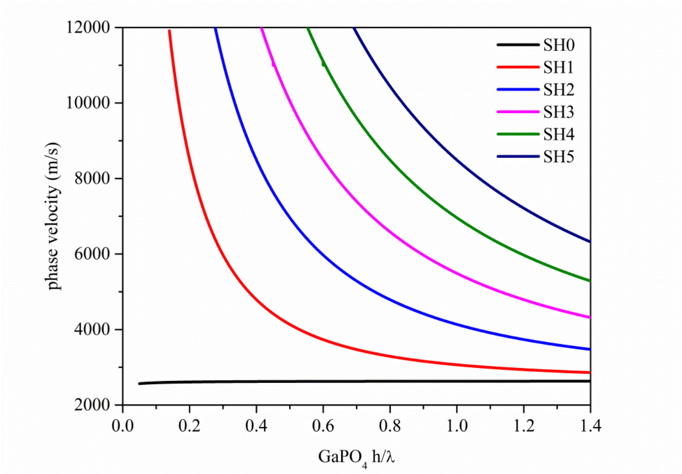

Figure 2.13: The phase velocity dispersion curves of $GaPO_4$ plate (0° 1° 90°) with H/λ=0.1.

SHAPMs have maximum displacements that occur on the top and bottom surfaces of the plate, with sinusoidal variation between the two sides. The field profile of the first four SHAPMs in ZnO (0° 90° 0°) H/λ=0.5 are shown in figure 2.14.

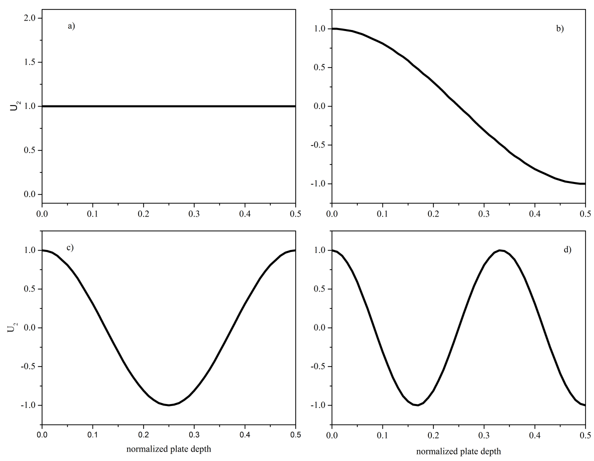

Figure 2.14: Cross-sectional displacement profiles for the four lowest-order SH plate modes in ZnO (0° 90° 0°) with normalized thickness H/λ=0.5.

SHAPM sensors sensitivity increases with increasing the mode order [1, 48, 49]: with increasing the mode order, the relative surface displacement (and particle velocity) increase as well as the viscosity sensitivity. Figure 2.15(a), (b) and (c) show the attenuation of the SH1, SH2 and SH3 modes vs the frequency thickness product for a glass plate immersed in ethylic alcohol (ρ = 790 kg/m^3, v_l = 1238 m/s, dynamic viscosity = $1.2\cdot10^{-3}$ Ns/m^2, kinematic viscosity = $1.52\cdot10^{-6}$ m^2/s), benzene (ρ = 881 kg/m^3, v_l = 1117 m/s, dynamic viscosity = $0.65\cdot10^{-3}$ Ns/m^2, kinematic viscosity =$7.38\cdot10^{-7}$ m^2/s) and kerosene (ρ = 822 kg/m^3, v_l =

1319 m/s, dynamic viscosity = $1.5 \cdot 10^{-3}$ Ns/m^2, kinematic viscosity =$1.82 \cdot 10^{-6}$ m^2/s). The viscosity of the liquids environment, being the mass density and the velocity quite similar.

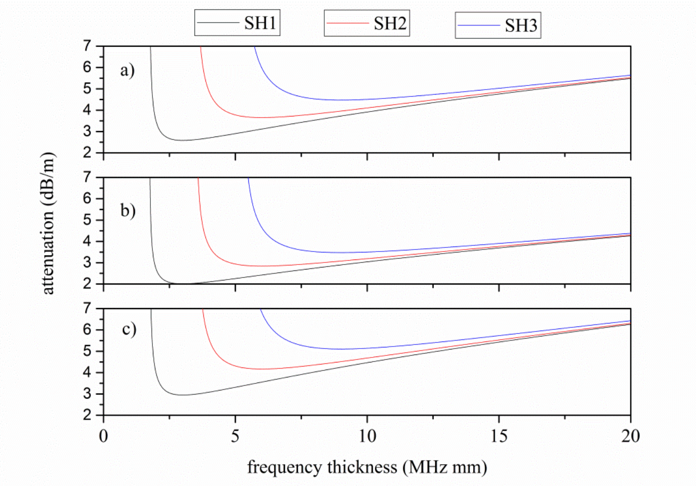

Figure 2.15: The attenuation of the SH1, SH2 and SH3 modes vs the frequency thickness product for a glass plate immersed in a) ethylic alcohol, b) benzene and c) kerosene.

The sensitivity also increases as the device is thinned: the lower limit of the plate thickness is limited by production processes and plate fragility. Figure 2.16(a) and (b) show the attenuation and the phase velocity of the SH1 mode vs frequency for three different thicknesses (1, 1.2 and 1.4 mm) of the glass plate immersed in kerosene: the curves move toward higher attenuation and velocity values with decreasing the plate thickness. The data of figure 2.15 and 2.16 were obtained by using the software Disperse [50].

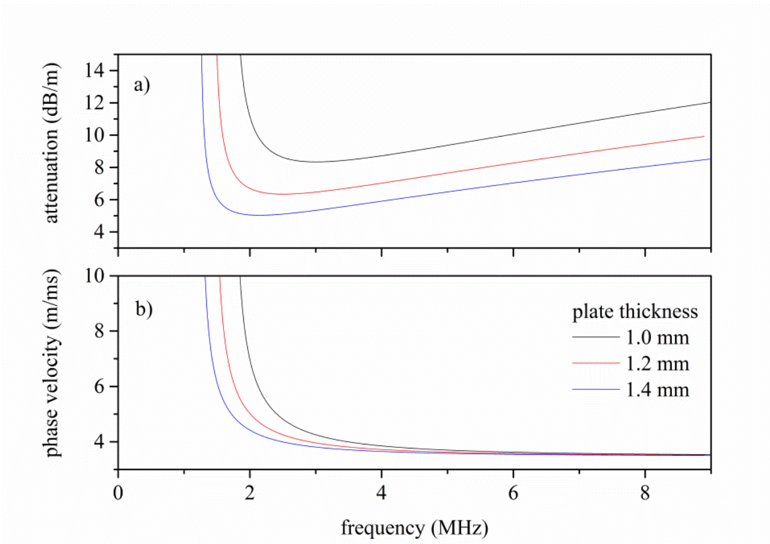

Figure 2.16: a) The attenuation and b) the phase velocity of the SH1 mode vs frequency for three different glass plate thicknesses: 1, 1.2 and 1.4 mm.

Martin et al. [51] were the first to use the SHAPM device as a fluid phase sensor in 42.75" rotated Y-cut (RYC) quartz (ST-quartz): they experimentally verified the ability of the sensor to monitor the conditions at the solid/liquid interface. A bare quartz plate was used to measure the viscosity of water/glycerol mixtures, while the plate with the sensing surface chemically modified by ethylenediamine ligands was used to detect low concentrations of Cu^{2+} ions in solution. After this paper, the SHAPM sensors have been successfully investigated for many applications. Some non-exhaustive examples of applications include the detection of mercury contamination in water, with (sub)- nanogram sensitivity, by using a ZX LNO and -65° Y rotated quartz plates covered by a gold sensing layer to accumulate the mercury via surface amalgamation [52]; the detection of potassium ions concentration in water with a relative frequency shift per unit potassium ions concentration was found equal to $-8.37 \cdot 10^{-4}$ for the fundamental mode, by using a ST-90° x quartz plate covered with a polyvinyl-chloride-valinomycin membrane [55]; the detection of concentration of NaCl and tris(hydroxymethyl)aminomethane (Tris) in aqueous solution [53] or to analyse the surface density changes associated with cell adhesion and proliferation *in vitro* condition, by using a STx quartz plate [54].

In reference [49] experimental results with various SHAPMs in ST 90°-x quartz plate concerning the influence of the temperature, the viscosity and the concentration of NaCl and tris(hydroxymethyl)aminomethane (Tris) in aqueous solution are presented: the higher order modes appeared to be more sensitive than the first ones, although having more transmission losses.

2.4 Lamb Wave sensors

Lamb waves (LWs) are elastic guided waves that travel in finite thickness plates, between stress-free plane and parallel boundaries; they are elliptically polarized in that they show in-plane and out-of-plane particle displacement components [56] LWs are divided into symmetric (S_n) and anti-symmetric (A_n) modes (where n is the mode order), depending on the symmetry with respect to the mid plane of the plate of the in-plane particle displacement. The velocity of the modes depends on the plate characteristics (material type, thickness, crystallographic cut and wave propagation direction); the higher the plate thickness and more and more LWs exist. LWs are highly dispersive: as an example, figure 2.17 shows the phase velocity v_{ph} vs the plate thickness-to-wavelength ratio curves of the S_n (red curves) and A_n (blue curves) LWs travelling in a Si(001)<100> plate of thickness h. The shape of the modes, the displacement components variation across the cross section of the plate, changes considerably with the plate thickness and with the mode order [57].

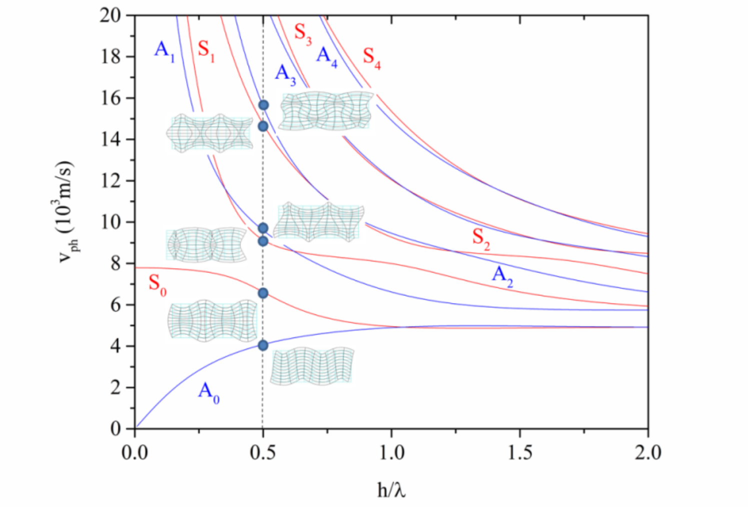

Figure 2.17: The v_{ph} dispersion curves of the S_n (red curves) and A_n (blue curves) Lamb modes travelling in a Si(001)<100> plate in air. The insets show the field profile of different modes at the same abscissa value (h/λ = 0.5) and are marked by a blue dot.

The insets of figure 2.17 show the mode shape of the first six modes travelling along the plate with fixed thickness (h/λ = 0.5); figure 2.18 shows the same v_{ph} dispersion curves as in figure 1 but the insets are related to the shape of one mode (S_2) at different h/λ (0.4. 1.0, and 1.8). The data of figure 2.17 and 2.18 were calculated using a software tool (DISPERSE) [50].

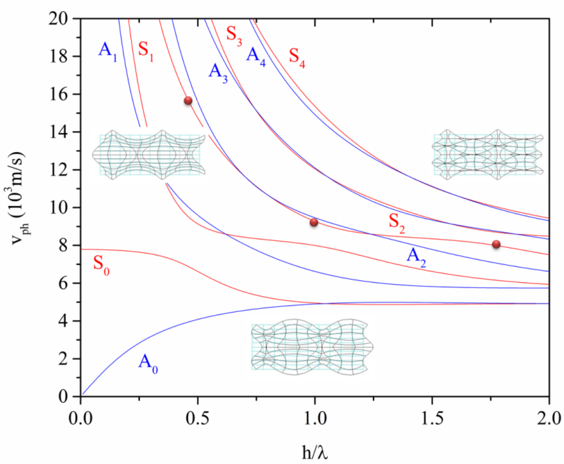

Figure 2.18: The v_{ph} dispersion curves of the S_n (red curves) and A_n (blue curves) Lamb modes travelling in a Si(001)<100> plate in air. The insets show the field profile of the S_2 mode at different abscissa values (0.4. 1.0, and 1.8) marked by a red dot.

As the LWs have velocity higher than that of the surrounding liquid medium and have both in-plane and out-of-plane displacement components, they are not suitable for sensing applications in liquids, except in some special cases. These cases include: (1) a branch of the fundamental *symmetric* S_0 mode dispersion region where the longitudinal particle displacement component, U_1, is dominant over the out-of-plane component U_3 at both the plate surfaces and in the plate depth (the mode is mostly linearly polarized and propagates at a velocity slightly lower than the velocity of the longitudinal bulk acoustic wave, v_{LBAW}); (2) a branch of the higher order *symmetric* modes dispersion curve, where the modes have U_3 ~0 at the plate surfaces (but not in the plate depth), and travel at velocity equal to v_{LBAW}; (3) a branch of the fundamental *anti-symmetric* A_0 mode dispersion curve, to which corresponds a velocity lower than that of the fluid.

2.4.1 Quasi-longitudinal symmetric modes

There are certain points of the symmetric LWs dispersion curves where the phase velocity is close to the longitudinal bulk acoustic wave (LBAW) velocity of the plate material, v_{LBAW}, and the field profile has particular characteristics, such as $U_3 << U_1, U_2$ at the plate surfaces. These waves, named *quasi-longitudinal* LWs (QL-LWs), can travel along the surface of the guiding plate while contacting a liquid environment without suffering large attenuation. Inside a small branch of the S_0 v_{ph} dispersion curve, corresponding to $h/\lambda<<1$, U_1 can even have a constant amplitude along the whole depth of the plate, while U_3 is at least 10 times less than U_1 at any plate depth [50]: the shape of the membrane particle movement is a flat ellipse and its longer axis is parallel to the surface of the plate. The higher order symmetric modes dispersion curves intersect the velocity of the LBAW in the plate material (v_{LBAW} = 8440 m/s for Si) and they show equal group velocity (v_{gr} = 7275 m/s). Figure 2.19 highlights the intersection of the LWs dispersion curves in a Si(001)<100> plate with the plate material v_{LBAW}: the mode shape of both the A_n and S_n modes at these points shows $U_3 = 0$ at the plate surfaces but, while the A_n curves are highly dispersive, the S_n modes show instead a flat dispersion region centred at the intersection point; this region corresponds to a h/λ band where the condition $U_3 << U_1$ is satisfied, thus preventing the sensor performances to be highly affected by possible errors in the fabrication technology of the sensor device.

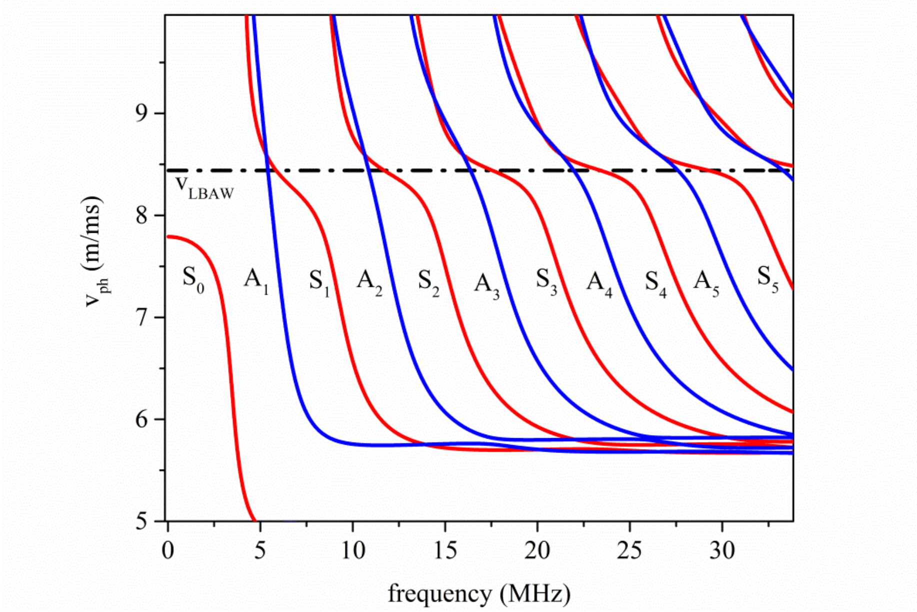

Figure 2.19: Dispersion curves for the LWs of a Si(001)<100> plate, 1mm thick, showing the intersections of the symmetric modes with a phase velocity equal to the LBAW velocity.

As an example, figure 2.20 shows the field profile of the first four symmetric QL-LWs of figure 2.19: QL-S_0 (f = 0.441 MHz), QL-S_1 (f·h = 5219 MHz), QL-S_2 (f = 11.642 MHz), and QL-S_3 (f = 17.537 MHz). For the QL-S_1 to QL-S_3 modes, U_3 is null only at the plate surfaces, but not inside the bulk of the plate; for QL-S_0 the U_3 vanishes on the plate surfaces and remains very small even in the plate depth, while U_1 is almost constant through the plate thickness. As it can be seen in figure 2.20, the through-thickness for U_1 and U_3 are symmetric and antisymmetric about the mid plane of the plate, and the number of the minima increases with increasing the mode order. Since the U_3 component of these higher order modes vanishes on the free surfaces of the plate, these modes are suitable for liquid sensing.

Figure 2.21 shows the v_{ph} and attenuation vs f·h curves for the first four symmetric modes (S_0, S_1, S_2 and S_3) for a Si plate immersed in water: when the velocity of the higher order modes reaches the v_{LBAW} (8440 m/s), the attenuation rapidly drops to zero, thus confirming the modes suitability to sensing applications in liquid environments. The dispersion curves of figure 2.21 were normalized with respect to the plate thickness by plotting them against the frequency thickness product

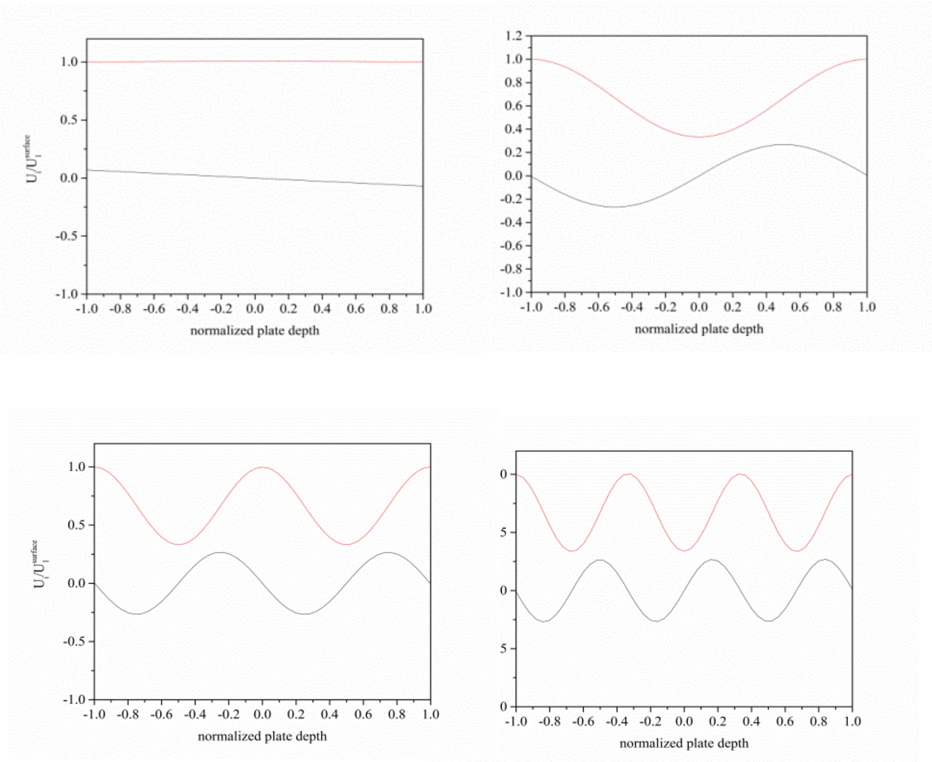

Figure 2.20 Cross-sectional normalized distribution of U1 and U3 displacement components for: a) QL-S0 at f = 0.441 MHz, b) QL-S1 (f = 5.8219 MHz), c) QL-S2 (f = 11.642 MHz), and d) QL-S3 (f = 17.537 MHz).

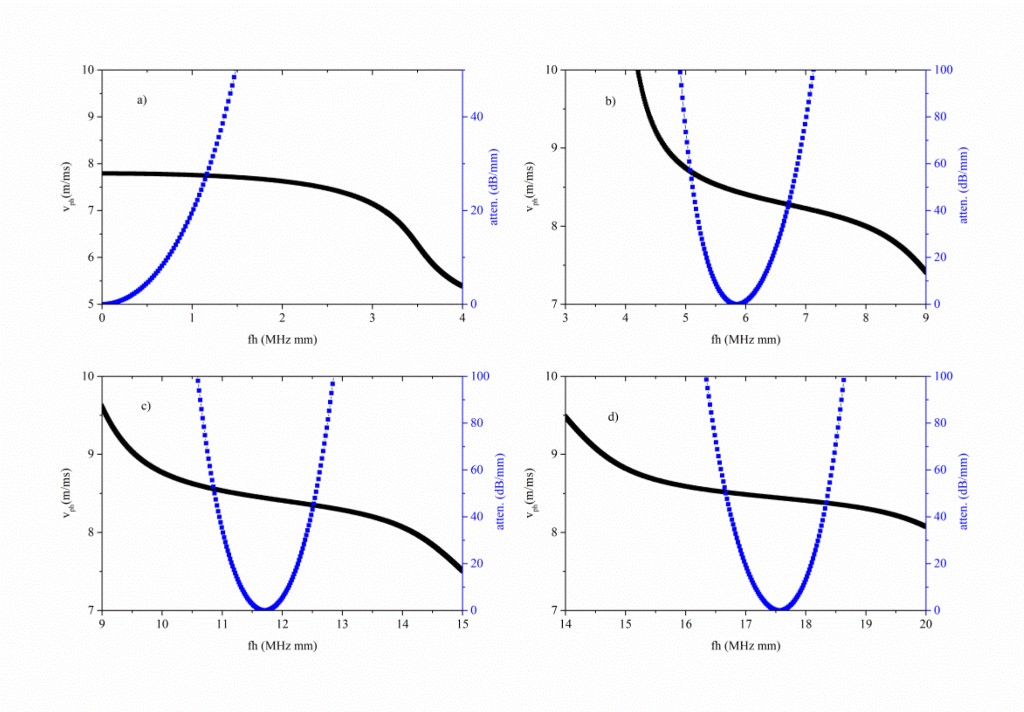

Figure 2.21 : The v_{ph} and attenuation vs f·h curves for the a) QL-S_0, b) QL-S_1, c) QL-S_2 and d) QL-S_3 modes travelling in a Si plate contacting a water half-space on both the two plate sides.

Table 2.2: The h/$\lambda_{threshold}$, h/λ_{range} and the K^2 values for two coupling configurations, for the QL-S_0 to QL-S_3 modes, for some piezoelectric materials. h/λ_{range} represents the normalized thickness range, centered in h/$\lambda_{threshold}$, where the condition $U_3/U_1 \leq 0.1$ at the plate surfaces is verified.

material		mode			
		QL-S_0	QL-S_1	QL-S_2	QL-S_3
BN	h/$\lambda_{threshold}$ h/λ_{range}	0.325 --	1 0.70-1.30	1.97 1.665 – 2.26	2.95 2.64 – 3.24
	K^2_{ST} (K^2_{MST}) (%)	0.09 (0.14)	0.035 (0.04)	0.018 (0.020)	0.012 (0.013)
ZnO	h/$\lambda_{threshold}$ h/λ_{range}	0.07 --	0.65 0.59 – 0.68	1.24 1.17 – 1.305	1.86 1.81 - 1.925
	K^2_{ST} (K^2_{MST}) (%)	0.47 (8.5)	0.42 (0.50)	0.22 (0.24)	0.15 (0.16)
AlN	h/$\lambda_{threshold}$ h/λ_{range}	0.11 --	0.79 0.75 - 0.89	1.58 1.5 – 1.67	2.37 2.29 – 2.46
	K^2_{ST} (K^2_{MST}) (%)	0.35 (3)	0.31 (0.37)	0.17 (0.19)	0.11 (0.13)
GaN	h/$\lambda_{threshold}$ h/λ_{range}	0.12 --	0.77 0.735 – 0.86	1.53 1.51 – 1.62	2.29 2.2 – 2.38
	K^2_{ST} (K^2_{MST}) (%)	0.26 (1.61)	0.18 (0.20)	0.095 (0.1)	0.06 (0.07)

The fundamental mode QL-S_0 exhibits a plate normalized thickness value, h/$\lambda_{threshold}$, beyond which U_3 is no more negligible ($U_3 > 10\% \cdot U_1$ while $U_1 = 1$ at the plate surfaces but it is no longer constant inside the plate). For h/λ< h/$\lambda_{threshold}$, the wave has $U_1 = 1$ and constant along the plate depth, and the U_3 component is less than 10% of U_1. The h/$\lambda_{threshold}$ has been calculated for several piezoelectric materials by using the McGill software [34] and the data are listed in table 5.1. For the higher order modes, the h/$\lambda_{threshold}$ values listed in table 5.1 have a different meaning with respect to QL-S_0: it is the plate thickness corresponding to the minimum value of U_3 at the plate surfaces (U_3/U_1 ~10^{-3}), for v_{ph} ~v_{LBAW}. By varying the thickness of the plate around h/$\lambda_{threshold}$, a h/λ range (h/λ_{range}) can be found inside which the condition $U_3/U_1 \leq 0.1$ at the plate surfaces is verified. Table 2.2 summarizes the h/$\lambda_{threshold}$ and h/λ_{range} of the fundamental and higher order quasi-longitudinal modes for some piezoelectric materials; the K^2 of the LWs have been evaluated for each material at the corresponding h/$\lambda_{threshold}$ for two coupling configuratio

The K^2 of both the two configurations are quite different for the QL-S_0 modes, but they become very similar with increasing the mode order. The K^2 decreases with increasing the mode order, and the MST configuration is always more efficient than the ST: this last effect is particularly evident for the QL-S_0 mode, while the K_{ST}^2 and K_{MST}^2 values become similar with increasing the mode order. Due to the small thickness value ($h/\lambda_{threshold} << 1$) of the QL-$S_0$-based plates, the IDTs fingers are quite close to the opposite metal floating electrode for the MST configuration and consequently the electric field is mainly perpendicular to the plate surfaces. This results in a coupling efficiency quite larger than that of the ST configuration [58].

2.4.1 Fundamental antisymmetric mode

Inside the LWs dispersion curves of figure 2.17, the A_0 mode is clearly identified by its reducing velocity as the plate thickness approaches zero. The A_0 mode, while being elliptically polarized, with U_3 not null at the plate surfaces, can travel along thin membranes that are in contact with a liquid if designed to travel at a velocity lower than that of most liquids, which lie in the range from 900 to about 1500 m/s, by choosing the proper plate thickness. At very small thickness-to-wavelength ratios, the phase velocity of the A_0 mode approaches zero; as the thickness increases, the velocity also increases, and reaches asymptotically from below the SAW velocity of the plate material.

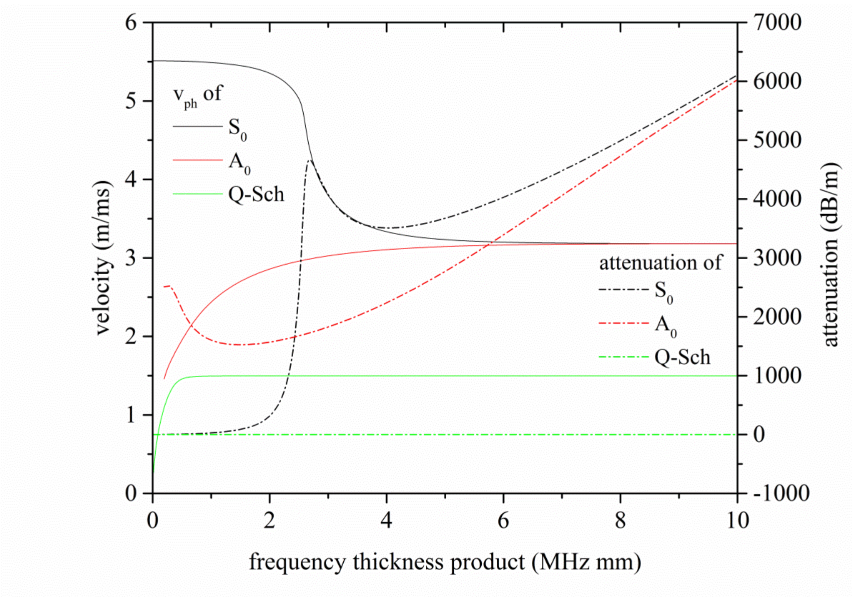

Figure 2.22: Phase velocity and attenuation dispersion curves of S_0, A_0 and SCH modes for a glass plate (h = 0.15 mm) thick immersed in water.

The Scholte mode, not shown in figure 2.17, is an anti-symmetric mode that propagates along the solid-fluid interface: its name comes from its similarity to the Scholte wave that is widely known in geophysics. The characteristic equation for the dispersion curve of this mode is obtained as a solution to the equations of continuity of stress and displacement at the solid-fluid interfaces to be solved for antisymmetric modes. In the low frequency limit, one solution is the A_0 mode and the other solution is the quasi-Scholte. The latter mode is characterized by an asymptotic behaviour of the phase velocity approaching the sound speed in the fluid at high frequencies; this non-dispersive branch of the quasi-Scholte mode dispersion curve is named Scholte mode. The polarisation of the mode is mostly parallel to the interface with a small out-of-plane displacement component. Figure 2.22 shows the phase velocity and attenuation curves versus the frequency for the S_0, A_0 and quasi-Scholte (Q-Sch) modes in a glass plate, 0.15 mm thick, immersed in water.

The S_0 mode attenuation starts from zero with the frequency and reaches a maximum value at 2.68 MHz·mm. In the limit as f·h tends to zero, the S_0 mode behaves basically as a longitudinally polarized wave, which explains its weak attenuation. When f·h tends to infinity the attenuation increases asymptotically with f^2: the mode is essentially concentrated at the surfaces of the plate and it radiates energy into the surrounding liquid in the same manner as a Rayleigh wave which is proportional to f^2. When the plate thickness becomes comparable with the acoustic wavelength, the A_0 mode behaves in the same way as the mode S_0 but it has an important attenuation in the low f ·h limit, caused by its flexural motion normal to the plate surface. The cut-off of the attenuation curve is at f·h =0.25 MHz·mm: below this limit, the phase velocity of the A_0 mode is smaller than the sound velocity in the liquid. As a result, no radiation of guided waves is allowed by the Snell law.

The phase velocity of the Q-Sch plate mode rises with frequency from zero and gradually asymptotes to the velocity of the liquid half spaces. Its attenuation is affected by the_fluid bulk velocity, viscosity and bulk longitudinal attenuation. Q-Sch mode travels unattenuated in the direction of the phase velocity (if the fluid has no longitudinal attenuation); as it travels at velocity lower than the bulk velocity of the fluid, it is consequently evanescent in the direction orthogonal to the interface. The wave amplitude decays in an exponential manner with distance from the interface. The extent to which the wave penetrates into the fluid depends on the frequency, as shown in figure 2.21 where U_1,

U_3 and the strain energy density (SED) of the Q-Sch mode travelling in a glass plate (1 mm thick) immersed in water at f = 107.602 and 454.186 kHz are shown.

The Q-Sch mode energy distribution between the fluid and the plate depends on the frequency, as shown in figures 2.23 (a) and (b): the out of plane displacement component at 107.602 kHz is almost constant across the section of the plate and the strain energy density indicates that the energy travels predominantly in the plate. At frequency 454.186 kHz a relevant part of the energy is travelling in the fluid, while at higher frequencies (> 1MHzmm) most of the energy travels in the fluid: the displacements decay away from the surfaces and are a minimum at the centre of the plate.

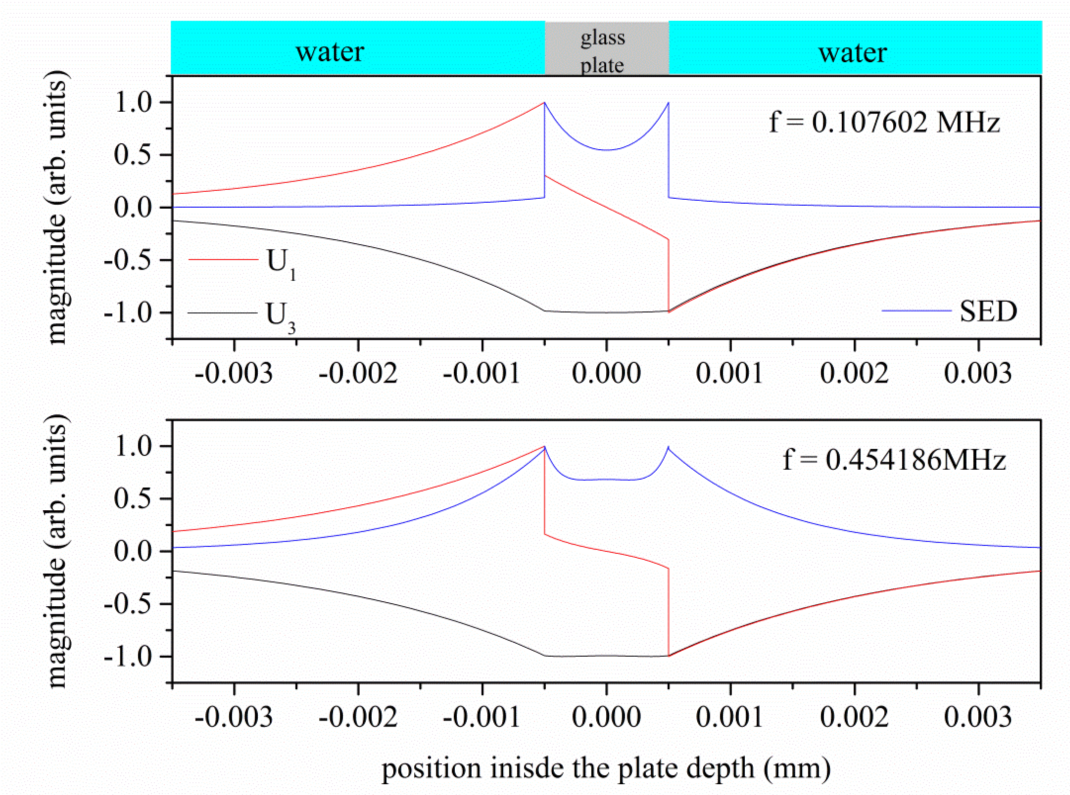

Figure 2.23: U_1, U_3 and the strain energy density (SED) of the Q-Sch mode travelling in a glass plate (1 mm thick) immersed in water at a) f = 107.602 and b) f = 454.186 kHz.

Q-Sch waves find application in liquid sensing as its attenuation, phase and group velocity are affected by the fluid viscosity, longitudinal bulk attenuation and bulk velocity, their measure can be used to characterize the fluid properties [59]. In reference [60] the effect of the waveguide material (steel, aluminium and brass) on the Q-Sch mode phase and group velocity sensitivities to the liquid parameters (longitudinal velocity and density) is theoretically studied. This review concluded that higher waveguide material density leads to higher sensitivities, and higher waveguide acoustic velocities lead to an extended effective sensing range. As an example figure 2.24 shows Scholte mode phase and group velocity dispersion curves in Al plate (1 mm thick) immersed in water (ρ = 1000 kg/m^3, v =1500 m/s), benzene (ρ = 881 kg/m^3, v = 1117 m/s, dynamic viscosity η = 0.65·10-3 Ns/m^2) and diesel (ρ = 800 kg/m^3, v =1250 m/s).

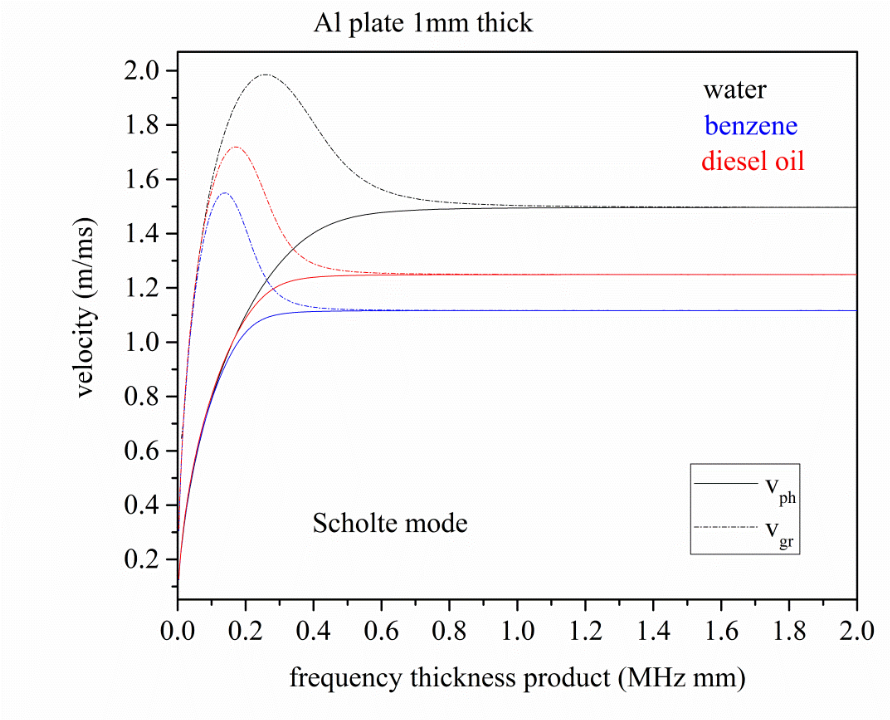

Figure 2.24: Scholte mode phase and group velocity dispersion curves in Al plate (1 mm thick) immersed in water (ρ = 1000 kg/m^3, v =1500 m/s), benzene (ρ = 881 kg/m^3, v = 1117 m/s, dynamic viscosity η = 0.65·10-3 Ns/m^2) and diesel (ρ = 800 kg/m^3, v =1250 m/s).

In reference [61] the sensitivity of the quasi-Scholte mode for fluid characterization was assessed experimentally by measuring the phase velocity values for the quasi-Scholte mode in distilled water and in different ethano-water concentrations. In reference [62] a Q-Sch mode-based device (a glass plate 0.15 mm thick) was used to arrange microbeads and living cells into regular arrays, to form plasma-enriched regions in whole blood and to rotate cells (pattern lines or arrays of cells, trigger spinning of living cells, and separate plasma from red blood cell in a whole blood microdroplet). In reference [63] a preliminary sensitivity analysis is performed for application to simultaneous multi-sensing physical quantities of liquids such as temperature, viscosity and density using interface waves.

The A_0 mode attenuation is larger than that of the S_0 mode due to its faster decay over the propagation distance, as shown in figure 2.21: the maximum attenuation (1106 dB/m = 1106*0.115129255 Nepers/m =127.33 Nepers/m) happens when f·h equals 0.15 MHz mm, when the A_0 Lamb wave phase velocity is close to the water sound speed. When the A_0 phase velocity is less than the water sound speed, there is still attenuation that approaches to zero slowly as h/λ comes to zero. Figures 2.25(a) and (b) show the A_0 and S_0 mode velocity and attenuation dispersion curves in Si plate (1mm thick) immersed in glycerol ($\rho = 1258\ kg/m^3$, $v = 1860\ m/s$, dynamic viscosity $\eta = 1.49\ Ns/m^2$), water ($\rho = 1000\ kg/m^3$, $v = 1500\ m/s$), benzene ($\rho = 881\ kg/m^3$, $v = 1117\ m/s$, dynamic viscosity $\eta = 0.65 \cdot 10^{-3}\ Ns/m^2$) and diesel ($\rho = 800\ kg/m^3$, $v = 1250\ m/s$); the longitudinal attenuation is set to zero.

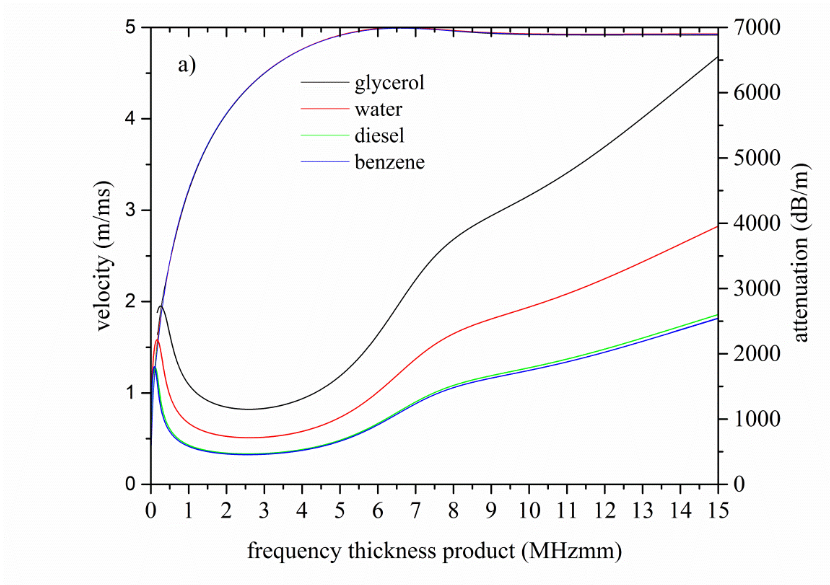

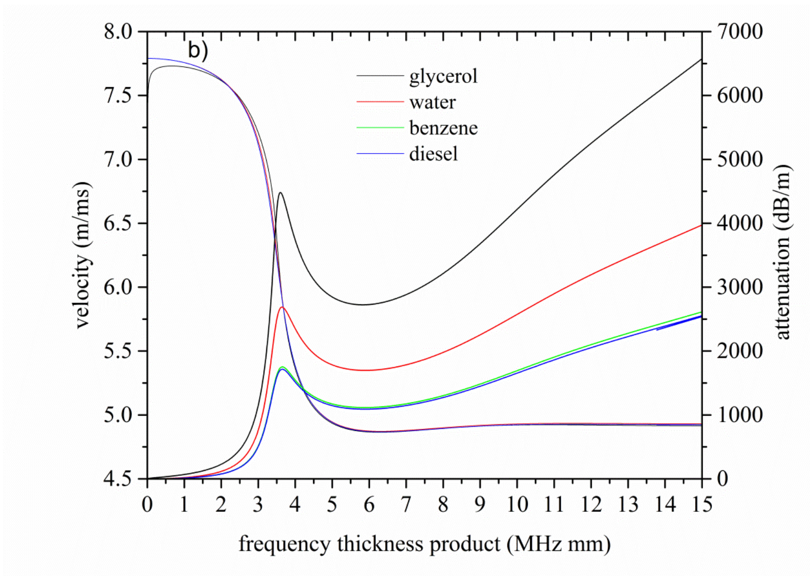

Figure 2.25: a) the A_0 mode and b) the S_0 mode velocity and attenuation dispersion curves in Si plate (1 mm thick) immersed in glycerol ($\rho = 1258\ kg/m^3$, $v = 1860\ m/s$, dynamic viscosity $\eta = 1.49\ Ns/m^2$), water ($\rho = 1000\ kg/m^3$, $v = 1500\ m/s$), benzene ($\rho = 881\ kg/m^3$, $v = 1117\ m/s$, dynamic viscosity $\eta = 0.65 \cdot 10^{-3}\ Ns/m^2$) and diesel ($\rho = 800\ kg/m^3$, $v = 1250\ m/s$).

In the low viscosity range, the amplitude response of the sensor is also affected by other parameters, such as temperature, pressure and density which can play more important roles than the viscosity. In the case of water and diesel, the sensor responses to these two liquids are well distinguishable and are affected only by the mass density and velocity of the liquids, being the viscosity assumed to be equal to zero. On the contrary, the sensor responses to benzene and diesel, which have quite similar ρ and v_l but different (and very low) η, are very similar.

The devices based on the A_0 mode suffer some limitations, such as the low operating frequency ($f = v_{ph}/\lambda$) due to the v_{ph} of A_0 mode which must be lower than the liquid velocity; thus, the A_0-based device is not suitable to achieve high frequencies that is a prerequisite to enhance the sensor sensitivity [1]. If the device frequency is increased by reducing the IDT width, two technological problems are met: 1. if the sensor is implemented onto a single crystal piezoelectric substrate, the plate thickness must be scaled down together with the wavelength, thus increasing the fragility of the thinned plate; 2. If the sensor is implemented onto a thin suspended piezoelectric membrane, the layer structural quality imposes an upper limit to the maximum (and minimum) thickness. Another limitation is the achievable efficiency of electrical excitation of the acoustic wave. The K^2 of A_0 mode is dispersive as it depends on the membrane thickness. The theoretical K^2 dispersion curve of the A_0 mode is reported in reference [50] for various piezoelectric plates (BN, ZnO, InN, AlN and GaN), for two coupling structures: the Substrate/Transducer and Metal/Substrate/Transducer configurations. Table 2.3 lists the threshold plate thickness for operation in water ($v_{ph} \leq v_{water}$ = 1480 m/s) and the corresponding K^2 of the ST and MST structures at the threshold [58].

Table 2.3: the A_0 mode $h/\lambda_{treshold}$ for operation in water (vph ≤ v_{water} = 1480 m/s) and the corresponding K^2 of the ST and MST structures at $h/\lambda_{treshold}$.

material	$h/\lambda_{treshold}$	K_{ST}^2 (%)	K_{MST}^2 (%)
ZnO	0.19	2.63	0.7
BN	0.05	0.011	0.0
AlN	0.087	0.25	0.02
GaN	0.12	0.35	0.06
InN	0.2	1.77	0.58

Even thou the ZnO K^2 is relatively high, it is significantly smaller than that of the QL-S_0 mode (8.5% for MST structure).

The experimental result of fluid loading of a Lamb wave sensor employing A_0 mode was firstly reported by R.M White and S.W. Wenzel in 1988 [64]. Furthermore, the same group reported the experimental result of viscosity and density sensing using the same device [65] consisting of a composite SiN and ZnO membrane with the thicknesses range from 2.8 um to 6.0 μm and the IDT periodicity of 100 μm. In this configuration, the membrane normalized thickness is thin enough to obtain A_0 phase velocity lower the sound velocity in water. For 0.06 h/λ, they obtained A_0 and S_0 modes with velocity of 470 m/s and 7850 m/s respectively. The effect of viscous fluid loading on A_0 mode is reported which show linear relationship between the attenuation loss and the square root of the product of fluid mass density and viscosity. Moreover, the authors demonstrated that simultaneous measurement of frequency shift and attenuation loss allows a fluid's viscosity and density to be determined.

In reference [66] experimental results on A_0-based sensor on PZT are described. The device was fabricated by deposition of low-pressure chemical-vapor deposition (LPCVD) silicon nitride, 1 μ thick, a metal ground plane of Ta/Pt (10 nm/150 nm), and a 750-nm-thick layer of sol-gel-derived PZT on silicon wafer, followed by the lift off process of Ta/Pt (10 nm/150 nm) IDTs. The KOH was used for anisotropic etching of the back side of the silicon wafer to release the composite membranes structure. They obtained A_0 mode phase velocities in between 295–312 m/s and group velocities in between 414–454 m/s. A frequency shift of 850 kHz and an insertion loss as low as 3 dB are observed when the back side of the membrane is in contact with a column of 15-mm height of deionized water.

The theoretical study based on the Rayleigh's perturbation approach to compare the A_0 and S_0 Lamb wave sensors sensitivity in liquid is reported [67]: it is shown that the sensitivity of the A_0 mode is much greater than that of S_0 mode. In reference [68] the experimental test of the A_0, S_0 and SH_0 sensors demonstrate that the A_0 mode frequency shift caused by the presence of liquid is quite larger than that of the S_0 and SH_0 modes.

The most recent experimental result of S_0 mode to measure the mechanical and electrical liquid properties is reported by Miera et. Al. [69]: using two AlN-based S_0 sensor topologies, with floating bottom metallic layer and without, the influence of mechanical and electrical properties of different aqueous mixtures was experimentally assessed.

Bibliography

[1] Acoustic Wave Sensors: Theory, Design and Physico-Chemical Applications, Series Editors: Moises Levy Richard Stern, Authors: D. Ballantine, Jr. Robert White S. Martin Antonio Ricco E. Zellers G. Frye H. Wohltjen, Academic Press 1997.

[2] C. Caliendo, A. D'Amico, P. Verardi, E. Verona, Surface acoustic wave H2 sensor on silicon substrate, 1988 IEEE Ultrasonics Symposium Proc., Chicago (IL), 2-5 Oct. 1988, p. 569-574, vol.1.

[3] C. Caliendo, A. D'Amico, E. Verona, Surface acoustic gas sensors, in Gas sensors: Principles, Operation and Developement, cap: VIII, Ed. G. Sberveglieri, (Kluver Academic Publisher, Dordrecht 1992), pp. 281-306.

[4] A.J. Ricco, S.J. Martin, T.E. Zipperian, Surface acoustic wave gas sensor based on film conductivity changes, Third International Conference on Solid-State Sensors and Actuators (Transducers '85), Philadelphia, PA, U.S.A., June 11 - 14, 1985,

[5] R. Arsat, M. Breedon, M. Shafiei, K. Kalantar-zadeh, W. Wlodarski, P. G. Spizziri, S. Gilje, R. B. Kaner , Graphene-like nano-sheets for surface acoustic wave gas sensor applications, Chemical Physics Letters, ISSN: 0009-2614, Vol: 467, Issue: 4, Page: 344-347, 2009,

[6] Adnan Mujahid and Franz L. Dickert, Surface Acoustic Wave (SAW) for Chemical Sensing Applications of Recognition Layers, Sensors (Basel). 2017 Dec; 17(12): 2716, doi: 10.3390/s17122716.

[7] C. Caliendo, A. D'Amico, A. Furlani, G. Iucci, M.V. Russo, E. Verona, A new surface acoustic wave humidity sensor based on a polyethynyl-fluorenol membrane, Sensors and Actuators, B 18, 82 (1994).

[8] Li, Z., Jones, Y., Hossenlopp, J., Cernosek, R., and Josse, F. (2005) Analysis of liquid-phase chemical detection using guided shear horizontal-surface acoustic wave sensors. Anal. Chem., 77: 4595–4603.

[9] X.C.Zhou, S.C.Ng, H.S.O.Chan, S.F.Y.Li, Piezoelectric sensor for detection of organic amines in aqueous phase based on a polysiloxane coating incorporating acidic functional groups, Analytica Chimica Acta, Volume 345, Issues 1–3, 20 June 1997, Pages 29-35,

[10] Steffen Rösler, Ralf Lucklum, Ralf Borngräb, Sensor system for the detection of organic pollutants in water by thickness shear mode resonators, 1998 Sensors and Actuators B Chemical 48(1):415-424, DOI: 10.1016/S0925-4005(98)00079-3.

[11] Berkenpas E., Millard P, Pereira da Cunha M., Detection of Escherichia coli O157:H7 with langasite pure shear horizontal surface acoustic wave sensors, Biosens Bioelectron. 2006 Jun 15;21(12):2255-62. Epub 2005 Dec 13.

[12] Howe E, Harding G., A comparison of protocols for the optimisation of detection of bacteria using a surface acoustic wave (SAW) biosensor.. Biosens Bioelectron. 2000;15(11-12):641-9.

[13] Kerstin Länge & Bastian E. Rapp & Michael Rapp, Surface acoustic wave biosensors: a review, Anal Bioanal Chem (2008) 391:1509–1519, DOI 10.1007/s00216-008-1911-5

[14] Advances in surface acoustic wave technology, systems and applications, Vol.2, Ed. C. W. Ruppel and Tor A. Fjeldly, 2001 World Scientific Singapore, book chapter "Pseudo and High Velocity Pseudo SAWs", M. P. da Cunha, pp. 203-244.

[15] F. S. Hickernell, E. L. Adler, "The experimental and theoretical characterization of SAW modes on ST-X quartz with a zinc oxide film layer", Proc. IEEE Int. Freq. Contr. Symp., pp. 852-857, 1997-May.

[16] L. A. Francis, J.-M. Friedt, C. Bartic and A. Campitelli, A SU-8 liquid cell for surface acoustic wave biosensors, Proc. SPIE 5455, MEMS, MOEMS, and Micromachining, (16 August 2004); doi: 10.1117/12.544779;

[17] M. P. da Cunha, Pseudo and High velocity Pseudo SAW, in Advances in Surface Acoustic Wave Technology, Systems and Applications, Volume 2, Editors Clemens C. [18] W. Ruppel and Tor A. Fjeldly, 2001 World Scientific Publishing, Singapore, New Jersey, London, Hong Kong, pp. 203-243.

[18] M. Pereira da Cunha, PSAW and HVPSAW behaviour in layered structures, Proceedings of the International Conference Microwave and Optoelectronics 1997 SBMO/IEEE MTT-S 11-14 Aug., Natal, Brazil

[19] M. Pereira da Cunha, Effects of layer thickness for GSAW, PSAW and HVPSAW devices, 1997 IEEE Ultrasonics Symposium Proceedings, (Cat. No.97CH36118) 1997, Volume: 1, Pages: 239 – 244, DOI: 10.1109/ULTSYM.1997.663018.

[20] Eric L. Adler , SAW, pseudo SAW, and hvpseudo SAW in langasite, 1998 Proceedings of the IEEE Ultrasonics Symposium pp. 307 - 310 vol.1, DOI10.1109/ULTSYM.1998.762152.

[21] Michio Kadota, Jun Nakanishi, Takeshi Kitamura and Makoto Kumatoriya, Properties of Leaky, Leaky Pseudo, and Rayleigh Surface Acoustic Waves on Various [10] Rotated Y-cut Langasite Crystal Substrates, 1999 The Japan Society of Applied Physic, Japanese Journal of Applied Physics, Volume 38, Part 1, Number 5B .

[22] M. Pereira da Cunha ; D.C. Malocha ; D.W. Puccio ; J. Thiele ; T.B. Pollard, LGX pure shear horizontal SAW for liquid sensor applications, IEEE Sensors Journal, Vol. 3, Issue: 5, Oct. 2003, pp. 554 – 561, 2003, DOI: 10.1109/JSEN.2003.817163.

[23] J. Hechner , W. Soluch, Pseudo surface acoustic wave dual delay line on 41◦YX LiNbO3 for liquid sensors, Sensors and Actuators B 111–112 (2005), pp. 436–440.

[24] Jun Kondoh, Shohei Tabushi, Yoshikazu Matsui, Showko Shiokawa, Development of methanol sensor using a shear horizontal surface acoustic wave device for a direct methanol fuel cell, Sensors and Actuators B 129 (2008) 575–580.

[25] Marshall S. Smith ; Donald C. Malocha, High frequency characterization of leaky waves for liquid delay line sensors, SENSORS, 2016 IEEE, 30 Oct.-3 Nov. 2016, DOI: 10.1109/ICSENS.2016.7808402.

[26] F. S. Hickemell, E. L. Adler, Pseudo-SAW Propagation on Layered Piezo-Substrates:Experiments and Theory Including Film Viscosity, Ultrasonics Symposium, 1996. Proceedings., 1996 IEEE, 3-6 Nov. 1996, San Antonio, TX, USA, USA, DOI: 10.1109/ULTSYM.1996.583805.

[27] Showko Shiokawa and Toyosaka Moriizumi, Design of SAW Sensor in Liquid, 1988 Japanese Journal of Applied Physics, Volume 27, Supplement 27-1.

[28] X.J. Tong ; D. Zhang ; Y.C. Li ; Y.A. Shui, Investigation of longitudinal leaky surface acoustic wave on lithium niobate and quartz, Ultrasonics Symposium, 1997. Proceedings., 1997 IEEE 5-8 Oct. 1997, DOI: 10.1109/ULTSYM.1997.663000.
[29] X.J. Tong ; D. Zhang, Novel propagation direction of quasi-longitudinal leaky surface acoustic wave on quartz and its potential as liquid sensors, Sensors and Actuators A Physical 78(2-3):160-162 DOI 10.1016/S0924-4247(99)00221-6.
[30] Yingmin Fan, Zhenghui Liu, Gengzhao Xu, Haijian Zhong, Zengli Huang, Yumin Zhang, Jianfeng Wang, and Ke Xu, Surface acoustic waves in semi-insulating Fe-doped GaN films grown by hydride vapor phase epitaxy, Appl. Phys. Lett. 105, 062108 (2014); https://doi.org/10.1063/1.4893156.
[31] Fumiya Matsukura, Masato Uematsu, Keiko Hosaka and Shoji Kakio, Longitudinal-Type Leaky Surface Acoustic Wave on LiNbO3 with High-Velocity Thin Film, 2013 The Japan Society of Applied Physics, Japanese Journal of Applied Physics, Volume 52, Number 7S .
[32] E. Gizelli, A.C. Stevenson, N.J. Goddard, C.R. Lowe, Surface skimming bulk waves: a novel approach to acoustic biosensors, TRANSDUCERS '91: 1991 International Conference on Solid-State Sensors and Actuators. Digest of Technical Papers, 24-27 June 1991 San Francisco, CA, USA, USADOI: 10.1109/SENSOR.1991.148975.
[33] María Isabel Rocha Gaso, Yolanda Jiménez, Laurent A. Francis and Antonio Arnau, Love wave Biosensors: A Review, Intech 2013, chapter 11, doi.org/10.5772/53077.
[34] E. L. Adler, J. K. Slaboszewics, G. W. Farnell, and C. K. Jen, IEEE Trans. Ultrason. Ferroelectr. Freq. Control 37, 215 (1990).
[35] Fabrice Martin, Glen McHale, and Michael I. Newton, Experimental Study of Love wave Sensor Response by Phase and Group Velocity Measurement, IEEE SENSORS JOURNAL, VOL. 4, NO. 2, APRIL 2004, pp. 216-220.
[36] Cinzia Caliendo, Muhammad Hamidullah, A Theoretical Study of Love wave Sensors Based on ZnO–Glass Layered Structures for Application to Liquid Environments, Biosensors (Basel). 2016 Dec; 6(4), 59.
[37] Z.N. Danoyan, G.T. Piliposian, Surface electro-elastic Love waves in a layered structure with a piezoelectric substrate and a dielectric layer, International Journal of Solids and Structures, 44 (2007), pp. 5829-5847.
[38] Gizeli E, Goddard NJ, Lowe CR, Stevenson AC. A Love plate biosensor utilising a polymer layer. Sens. Actuators, B 1992;6 131-137, https://doi.org/10.1016/0925-4005(92)80044-X
[39] Shyam Trivedi Harshal B. Nemade, Simulation of a Love wave device with ZnO nanorods for high mass sensitivity, Ultrasonics, Volume 84, March 2018, pp. 150-161.
[40].Sheng-Yuan Chu, Walter Water, Jih-Tsang Liaw, An investigation of the dependence of ZnO film on the sensitivity of Love mode sensor in ZnO/quartz structure, Ultrasonics, Volume 41, Issue 2, March 2003, pp. 133-139, https://doi.org/10.1016/S0041-624X(02)00430-4.
[41] Mihaela Puiu, Ana-Maria Gurban, Lucian Rotariu, Simona Brajnicov, Cristian Viespe, and Camelia Bala, Enhanced Sensitive Love wave Surface Acoustic Wave Sensor

Designed for Immunoassay Formats, Sensors (Basel). 2015; 15(5): 10511–10525, doi: 10.3390/s150510511.

[42] David A. Powell, Kourosh Kalantar-zadeh, Samuel Ippolito and Wojtek Wlodarski , A Layered SAW Device Based on ZnO/LiTaO3 for Liquid Media Sensing Applications, 2002 IEEE Ultrasonics Symposium, pp. 493-496.

[43] Feng-mei Zhou, Zhe Li, Li Fan, Shu-yi Zhang, Xiu-jiShui, Experimental study of Love-wave immunosensors based on ZnO/LiTaO3 structures, Ultrasonics, Volume 50, Issue 3, March 2010, Pages 411-415, https://doi.org/10.1016/j.ultras.2009.09.024.

[44] Santanu Manna, Santimoy Kundu and Shishir Gupta, Propagation of Love type wave in piezoelectric layer overlying non-homogeneous half-space, Electronic Journal of Mathematics and Technology, vol. 8, no. 1, 2014.

[45] Santanu Manna, Santimoy Kundu and Shishir Gupta, Propagation of Love type wave in piezoelectric layer overlying non-homogeneous half-space, Electronic Journal of Mathematics and Technology, vol. 8, no. 1, 2014.

[46] Cinzia Caliendo, Smail Sait and Fouad Boubenider, Love-Mode MEMS Devices for Sensing Applications in Liquids, Micromachines 2016, 7(1), 15;

[47] M. Hamidullah, C. Caliendo, F. Laidoudi, Love wave sensor based on PMMA/ZnO/Glass structure for liquids sensing, in: Proceedings of the Third Int. Electron. Conf. Sens. Appl., 15-30 November 2016; Sciforum Electronic Conference Series, 3, 2017, p. 20, doi:10.3390/ecsa-3-C005.5pp.

[48] C Caliendo, A D'Amico, P Verardi, E Verona, K+ detection using shear horizontal acoustic modes, Ultrasonics Symposium, 1990. Proceedings., IEEE 1990, 383-387]

[49] Corinne Dejous, Michel Savart, Dominique Rebiere, Dominique Rebiere, J. Pistre, J. Pistre, A shear-horizontal acoustic plate mode (SH-APM) sensor for biological media, 1995, Sensors and Actuators B Chemical 26(1-3), pp. 452-456.

[50] N. Pavlakovic, M. J. S. Lowe, D. N. Alleyne, and P. Cawley, Disperse: A general purpose program for creating dispersion curves, in D. O. Thompson and D. E. Chimenti editors, Review of Progress in Quantitative NDE, vol.16, pp. 185-192, Plenum Press, New York, (1997).

[51] S.J. Martin, A.J. Ricco and G.C. Frye, J. Appl. Phys. 64 (10), 5002-8 .1988; S. Martin, A. Ricco, T. Niemczyk, and G. Frye, “Characterization of SH acoustic plate mode liquid sensors,” Sens. Actuators, vol. 20, pp. 253-268, 1989.

[52] M.GSchweyer , J.Candle , D.JMcAllister, J.FVetelino , An Acoustic Plate Mode Sensor for Aqueous Mercury, Sensors and Actuators B: Chemical, Volume 35, Issues 1–3, September 1996, Pages 170-175, https://doi.org/10.1016/S0925-4005(97)80049-4.

[53] J. Andle, M. Schweyer, J. Munson, R. Roderick, D. McAllister, L. French, J. Vetelino, C. Watson, J. Foley, A. Bruce, M. Bruce, Electrochemical Piezoelectric Sensors for trace Ionic Contaminants, IEEE Transactions on Ultrasonics, Ferroelectrics, and Frequency Control, Vol. 45, Issue: 5, 1998, Page(s): 1408 – 1415,

[54] F.G. Tseng ; K.C. Leou ; L.C. Pan ; Y.Y. Lai ; Y.C. Liang ; L.D. Chen , Acoustic plate mode tissue sensor, SENSORS, 2002 IEEE, 12-14 June 2002, Orlando, FL, USA, USA

[55].F.G. Tseng ; K.C. Leou ; L.C. Pan ; Y.Y. Lai ; Y.C. Liang ; L.D. Chen , Acoustic plate mode tissue sensor, SENSORS, 2002 IEEE, 12-14 June 2002, Orlando, FL, USA, USA, DOI: 10.1109/ICSENS.2002.1037099.

[56] Viktorov, I., A. Rayleigh and Lamb Waves. Plenum Press New York, 1967.
[57] J.L. Rose, Ultrasonic Waves in Solid Media, Cambridge University Press, 1999.
[58] C. Caliendo, Longitudinal Modes along Thin Piezoelectric Waveguides for Liquid Sensing Applications, Sensors 2015, 15, 12841-12856; doi:10.3390/s150612841.
[59] Cegla, Frederic Bert, Ultrasonic waveguide sensors for fluid characterisation and remote sensing, Thesis (Ph.D.), Imperial College London, London UK. (2006), p. 248
[60[52] Onursal Önen, Dispersion and Sensitivity Analysis of Quasi-Scholte Wave Liquid Sensing by Analytical Methods, Hindawi, Journal of Sensors, Volume 2017, Article ID 9876076, 9 pages
[61] A. Takiy, S. Granja, R. Higuti, C. Kitano, L. Elvira, O.Martinez-Graullera and F. Montero de Espinosa, et al., Theoretical Analysis and Experimental Validation of the Scholte Wave Propagation in Immersed Plates for the Characterization of Viscous Fluids, 2013 Ieee International Ultrasonics Symposium, 21-25 July 2013, Prague, Czech Republic, pp.1610–1613, DOI: 10.1109/ULTSYM.2013.0411.
[62] Vivian Aubert, Régis Wunenburger, Tony Valier-Brasier, David Rabaud, Jean-Philippe Kleman and Cédric Poulain, A simple acoustofluidic chip for microscale manipulation using evanescent Scholte waves, *Lab Chip*, 2016,16, 2532-2539
[63] Onursal Onen,Yusuf Can Uz, Investigation of Scholte and Stoneley Waves in Multi-layered Systems, Physics Procedia Volume 70, 2015, Pages 217-221, part of Special Issue Proceedings of the 2015 ICU International Congress on Ultrasonics, Metz, France, Edited by Nico F. Declercq, doi.org/10.1016/j.phpro.2015.08.138.
[64] White, R. M., and S. W. Wenzel. "Fluid loading of a Lamb- wave sensor." Applied Physics Letters 52.20 (1988), pp. 1653-1655.
[65] Martin, Bret A., Stuart W. Wenzel, and Richard M. White. "Viscosity and density sensing with ultrasonic plate waves." Sensors and Actuators A: Physical 22.1-3 (1990), pp. 704-708.
[66] Luginbuhl, Philippe, et al. "Microfabricated Lamb wave device based on PZT sol-gel thin film for mechanical transport of solid particles and liquids." Journal of Microelectromechanical systems 6.4 (1997), pp.337-346.
[67] Wu, Junru, and Zhemin Zhu. "Sensitivity of Lamb wave sensors in liquid sensing." IEEE transactions on ultrasonics, ferroelectrics, and frequency control 43.1 (1996): 71-72.]
[68] Laurent, Thierry, et al. "Lamb wave and plate mode in ZnO/silicon and AlN/silicon membrane: Application to sensors able to operate in contact with liquid." Sensors and Actuators A: Physical 87.1 (2000), pp. 26-37.
[69] Mirea, Teona, et al. "Influence of liquid properties on the performance of S0- mode Lamb wave sensors II: Experimental validation." Sensors and Actuators B: Chemical 229 (2016): 331-337.

CHAPTER 3

HIGHER ORDER QUASI-LONGITUDINAL LAMB WAVES: FINITE ELEMENT ANALYSIS

This chapter focuses on the study of the propagation of higher order quasi-longitudinal Lamb modes and on the simulation of the electroacoustic devices based on these modes, both in air and contacting a liquid environment. The eigenfrequency analysis using COMSOL Multiphysics was performed to obtain the Lamb waves dispersion curves, followed by frequency domain analysis of Lamb wave resonator to obtain the frequency response. The time domain analysis was performed to simulate the Lamb waves delay line devices. The liquid model was developed by using viscoelastic models to obtain the resonator and delay line response when one free surface of the device is in contact with liquid. Finally, the frequency and the loss of the devices were simulated for different water and glycerol concentrations in order to estimate the devices sensitivity to the liquid viscosity-density product.

Related Publications:

Caliendo, Cinzia, **Muhammad Hamidullah**, and Farouk Laidoudi. "Amorphous SiC/c-ZnO-Based Quasi-Lamb Mode Sensor for Liquid Environments." Sensors 17.6 (2017): 1209.

Caliendo, Cinzia, Ennio Giovine, and **Muhammad Hamidullah**. "Theoretical Study of Quasi-Longitudinal Lamb Modes in SiN/c-AlN Thin Composite Plates for Liquid Sensing Applications." Multidisciplinary Digital Publishing Institute Proceedings. Vol. 2. No. 3. 2017.

As previously mentioned in chapter 2, the devices based on fundamental Lamb modes, A_0 and S_0 , are suitable for sensing applications in liquid environment when the plate thickness-to-wavelength (h/λ) ratio is small enough so that the phase velocity of A_0 is lower than the compressive wave velocity of the liquid (e.g. 1500 m/s in water), and when the longitudinal displacement component of the S_0 mode is dominant over the other components. Because of the h//λ << 1 limitation, the IDT wavelength must be significantly larger than the thickness of the plate, thus resulting in low operating frequency and large footprint of the devices. The A_0 and S_0 has been extensively studied theoretically and experimentally [1-3]. The most recent work from Mirea et al. reported the in-depth study on the influence of liquid properties on the performance of S_0-mode Lamb wave sensors including the finite element analysis and experimental result [4-5]. The low frequency and large IDT periodicity limitations can be overcome by exploiting higher order quasi-longitudinal Lamb waves (qL-LW) that have characteristics very similar to those corresponding to the S_0 mode (I.e., longitudinal polarization and velocity close to that of the LBAW) but they correspond a higher h/λ ratio [6]. However, as to our knowledge, only little work has been reported on qL-LWs , especially the use of simulation and finite element method (FEM) to explore qL-LWs for liquid sensing applications.

Lamb modes velocity dispersion curves are strongly dependent upon the material type, its crystallographic orientation, the wave propagation direction, and the plate composition (single material or multilayered plates). In the simple case of a homogeneous isotropic plates, the dispersion equations of the S_i and A_i modes can be expressed as:

$$\boldsymbol{S_i}: \quad \frac{tan\,(\frac{\beta h}{2})}{tan\,(\frac{\alpha h}{2})} = -\frac{(k^2-\beta^2)}{4\alpha\beta k^2} \tag{3.1}$$

and

$$\boldsymbol{A_i}: \quad \frac{tan\,(\frac{\beta h}{2})}{tan\,(\frac{\alpha h}{2})} = -\frac{(\beta^2-k^2)}{4\alpha\beta k^2} \tag{3.2}$$

where $\alpha^2 = \frac{\omega^2}{v_l^2} - k^2$ and $\beta^2 = \frac{\omega^2}{v_t^2} - k^2$, h is the plate thickness, ω is the angular frequency, k the wave number, vl and vt the plate material longitudinal and transverse bulk waves velocities. In case of anisotropic or for composite plates the modes dispersion equations cannot be explicitly written: there are so many materials constants involved that it is necessary to use an iterative numerical technique to determine the velocity and the h/λ combination that make the boundary conditions determinant to be zero. The commercial software DISPERSE [7] is a very useful tool suitable to obtain the Lamb wave dispersion curves for anisotropic (but non-piezoelectric) materials with up to 9 independent elastic constants. For materials with a more than 9 independent constants, as well as for piezoelectric materials, the accuracy of the calculation is obviously low. To account for the piezoelectricity of the material plate, the stiffened elastic constants can be provided to the software to increase the calculations accuracy. The McGill software [8] is another very important tool for the theoretical calculation of Lamb waves phase velocity dispersion curves of lossless anisotropic materials. However, obtaining the dispersion curve for several fundamental and higher order modes can be very tedious and since the mode shape cannot be extracted instantly, the mistake can occur in identifying the mode order.

In this chapter, COMSOL Multiphysics software is employed to investigate the dispersion curves and to identify the mode shapes of qL-LWs by using eigenfrequency study. The main advantage of the COMSOL software, in comparison with DISPERSE and McGill software, is the capability to obtain device-level simulations, where the *frequency domain* and the *time domain study* can be used to simulate the SAW resonator and delay line performances. However, the main drawback of FEM software in general is the requirement of very high computing power and simulation time. While there is no a "perfect" software to satisfy all need of theoretical calculation and simulation of Lamb waves, the use of COMSOL software accompanied by DISPERSE and McGill software is the best method for completing the study of Lamb waves and any other acoustic modes in general.

3.1 Higher Order Quasi-Longitudinal Lamb Waves in Single Crystal Piezoelectric Materials

The first theoretical study on the existence of higher order qL-LW in ST-cut Quartz is reported by Gulyaev [10], following the earlier report by Ivan Anisimkin [11]: the higher order qL-LW modes were found at h/λ =1.36±30%, 2.70±14%, and 4.04±10%. The author here clarify the characteristics of the higher order qL-LW modes: the phase velocity is equal or close to the velocity of bulk longitudinal wave (V_{LBAW}) and the phase velocity vs h/ λ. curve is slowly dispersive, meaning that the group velocity is close to the phase velocity. The presented dispersion curves in the report doesn't differentiate symmetric and antisymmetric modes: the mode shapes are presented but the group velocity dispersion curves are not reported.

In this subchapter of the present thesis, the COMSOL eigenfrequency study is used to verify the existence of qL-LW modes and to investigate the modes shape, followed by device level simulation of resonators and delay lines using frequency domain and time domain study, respectively.

3.1.1 Eigenfrequency analysis

Figure 3.1 shows the schematic of the COMSOL model for eigenfrequency study referred to a ST-cut quartz plate, with thickness h and width equal to the wavelength λ. In this simulation, h = 350 um and the wavelength is varied to achieve the h/λ values ranging from 0.05 to 2, with the step of 0.05. To obtain the Lamb waves solution, appropriate mechanical boundary conditions (BC) is applied: the continuity BC is applied in the left and right sides of the plate, and free boundary condition is applied on the top and bottom sides of the plate. The elasticity, piezoelectricity, and permittivity matrices of y-rotated Quartz (i.e., the ST-cut quartz) are calculated by MATLAB software. Then the simulation was performed firstly for open-open configuration, without applying any electrical boundary condition as shown in figure 3.1(a). then the simulation of short-open configuration was performed by applying shorted floating electrode BC on the top of the plate, as shown in figure 3.1(b). Finally, the short-short simulation is performed by applying shorted floating electrode BC on both top and bottom sides of the plate, as shown in figure 3.1(c). The different configurations are used to calculate the K^2 for film-transducer (ft) and metal-film-transducer (mft) configurations.

Figure 3.2 shows the phase velocity v_{ph} dispersion curves of the ST-cut Quartz for open-open configuration. The dispersion curve of the first higher order symmetric mode (S_1) shows v_{ph} equal to V_{LBAW} for h/λ in the range from 0.8 up to 1.9. This result agreed with reference [10] where the first qL-LW is obtained at h/λ =1.36±30%. From the graph, we can also observe several other modes (A_1, S_2, and A_2) with v_{ph} close to V_{LBAW} at h/λ =1.36. To verify whether those modes have also dominant longitudinal components, the dispersiveness of the waves can be observed by comparing the v_{ph} with group velocities v_g.

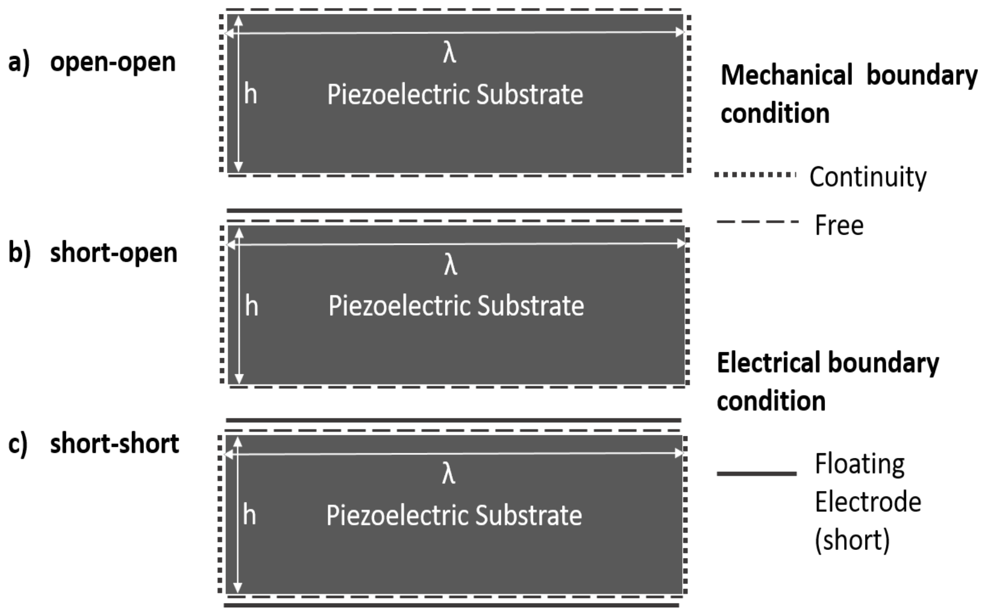

Figure 3.1 The COMSOL eigenfrequency simulation model for (a) open-open, (b) short-open and (c) short-short coupling configuration

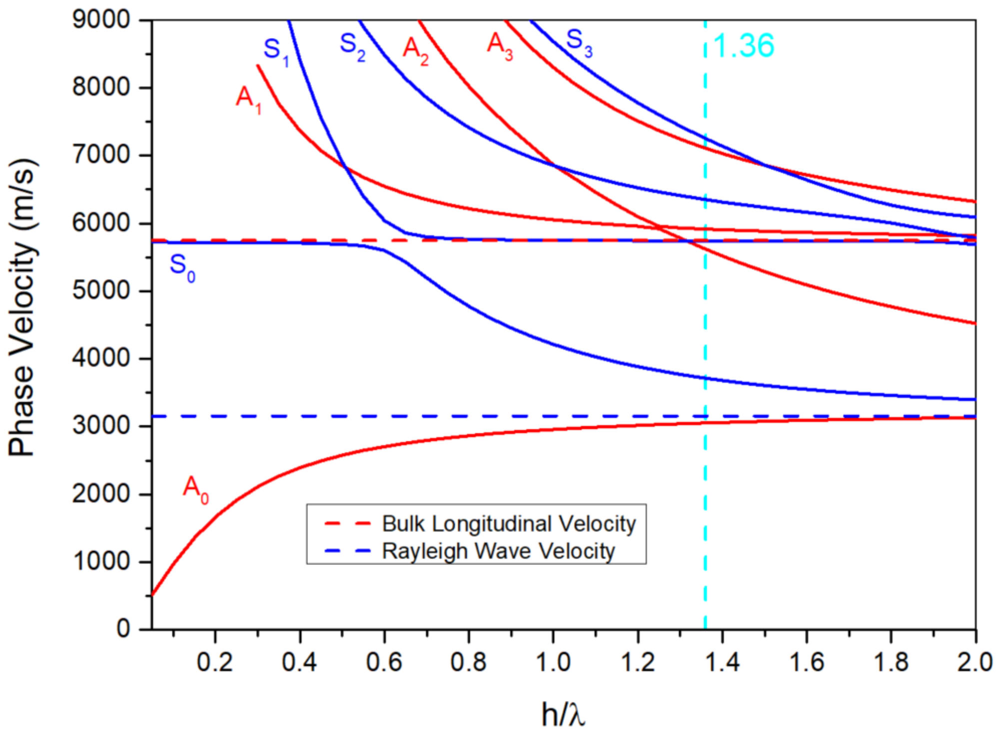

Figure 3.2 The dispersion curve of ST-cut Quartz with open-open coupling configuration

The v_{ph} and v_g dispersion curves for S_1, A_1, S_2, and A_2 modes are shown in figure 3.3. As we can see, at h/λ =1.36, the S_1 has v_g very closed to v_{ph}. The A_1 mode is also slowly dispersive because the v_g is quite closed to v_{ph}. S_2 and A_2 modes are quite dispersive with A_2 as the most dispersive. The difference between v_{ph} and v_g is 9.45, 340.2, 1228.5, 2721.6 m/s for S_1, A_1, S_2 and A_2, respectively. Due to the low-dispersive branch of the dispersion curve of the S_1 and A_1 modes, the fabrication of the S_1 and A_1-based devices is less sensitive to the accuracy of the technological processes.

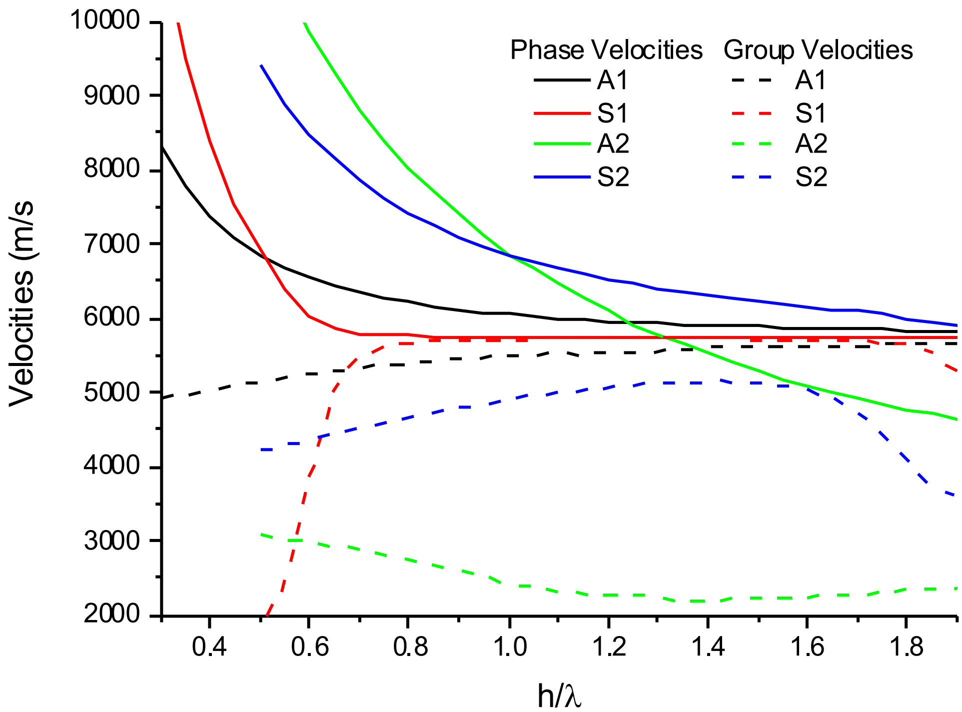

Figure 3.3 The phase and group velocities dispersion curve of A_1, S_1, A_2, S_2 modes

The mode shapes of the first 4 *symmetric* modes is shown in figure 3.4; the mode shapes of the first 4*antisymmetric* modes is shown in figure 3.5: both figures show the mode total displacement, i.e. the longitudinal and shear vertical displacement components U_3 and U_1. At it can be clearly seen, the S_1 and A_1 modes have dominantly longitudinal component.

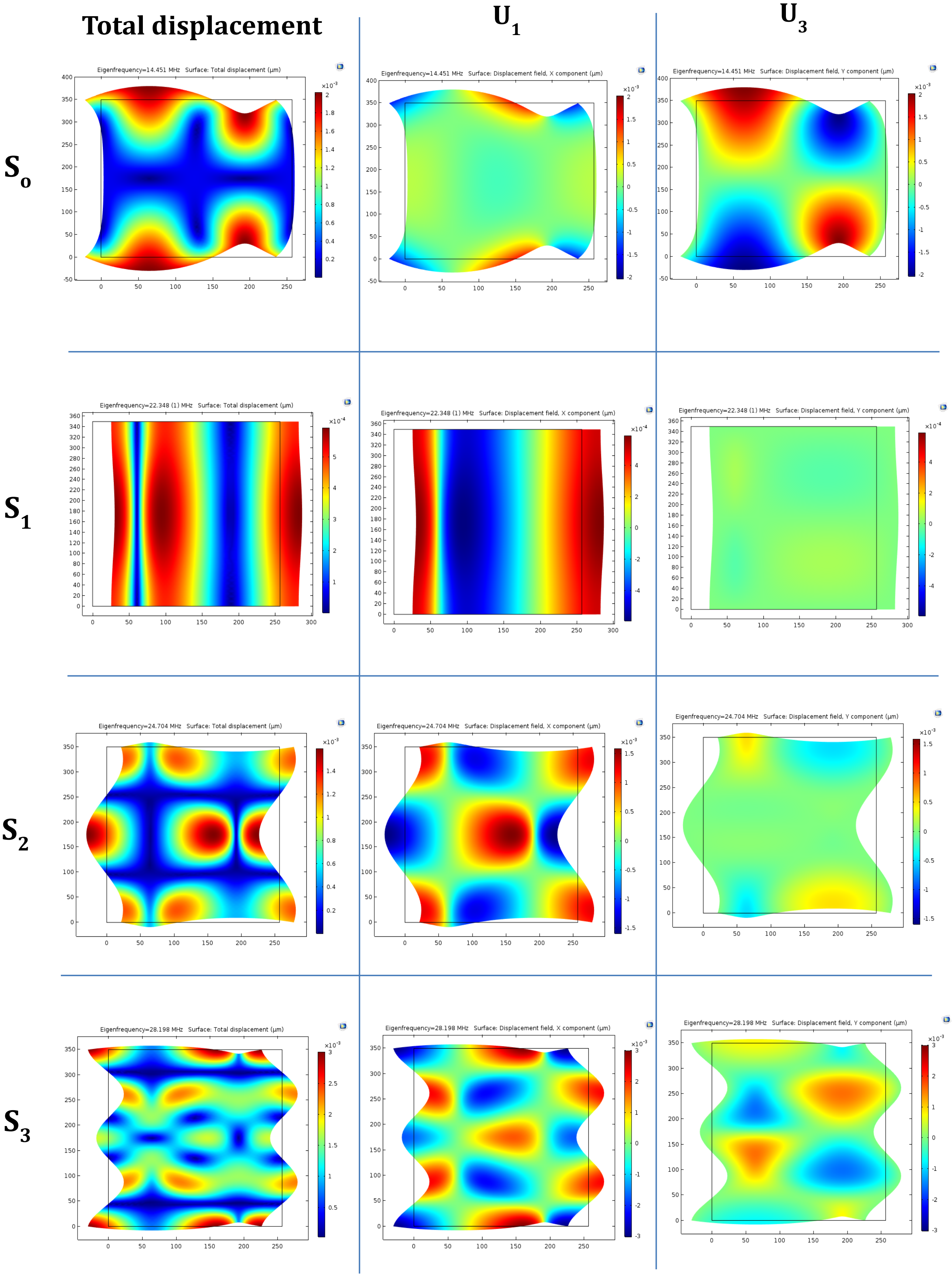

Figure 3.4: the mode shapes of the first 4 symmetric modes in quartz.

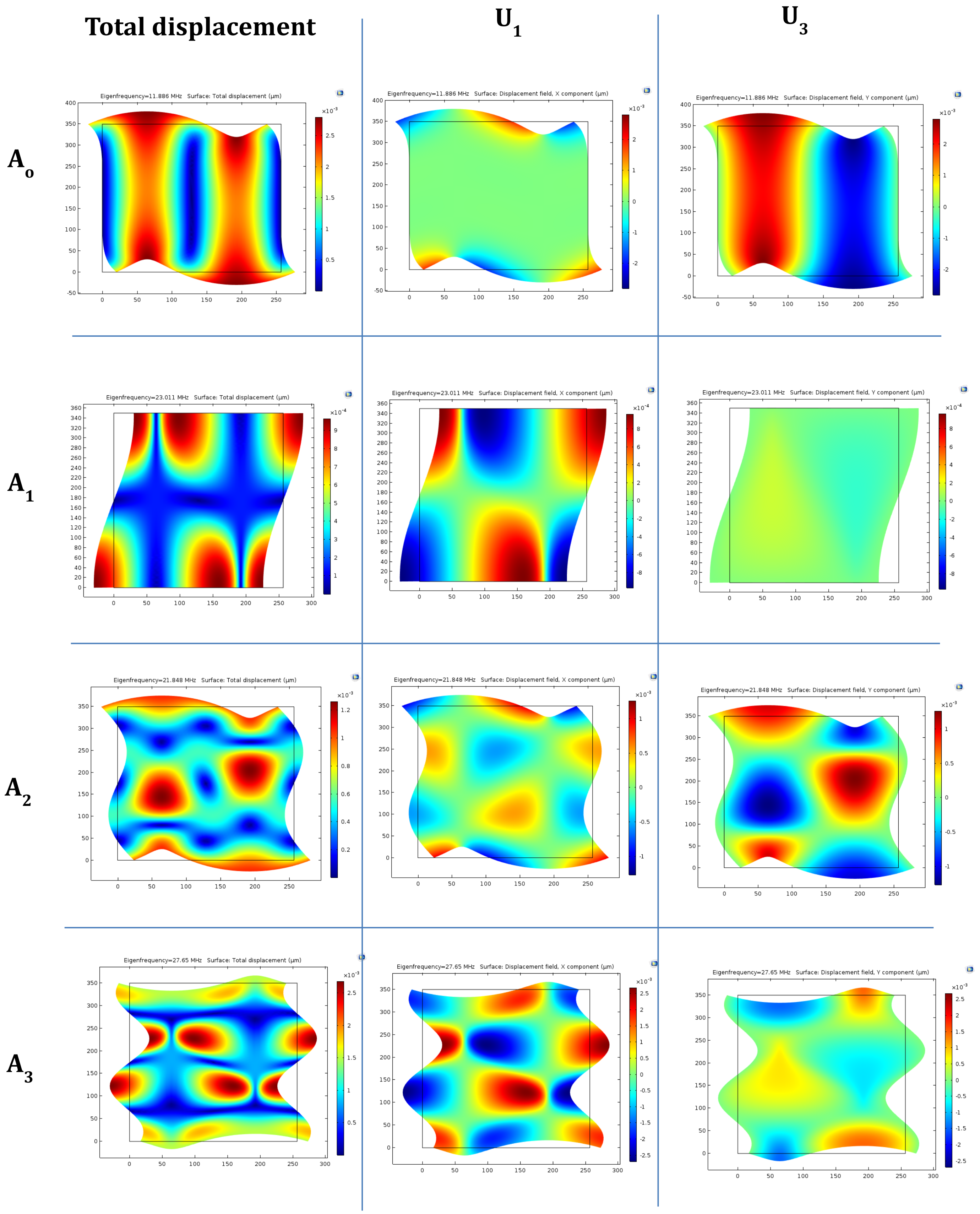

Figure 3.5: the mode shapes of the first 12 anti-symmetric modes in quartz

3.1.2 Frequency Domain analysis

Frequency-domain analysis is a widely used tool that shows how a signal energy is distributed over a range of frequencies. A time domain signal can be converted into a frequency domain signal and vice versa by using a mathematical operator called the Fourier transform and inverse Fourier transform. The former decomposes a function into the sum of sine wave frequency components: the 'spectrum' of frequency components is the frequency domain representation of the signal. The inverse Fourier transform converts the frequency domain function back to a time function. Figure 3.6 shows the frequency domain model adopted to study the frequency response of a Lamb modes-based one port resonator for two different coupling configurations, named “ft” and “mft”. The “ft” configuration includes only the IDT onto the upper side of the plate; the “mft” configuration also includes a metal floating layer on the lower side of the plate.

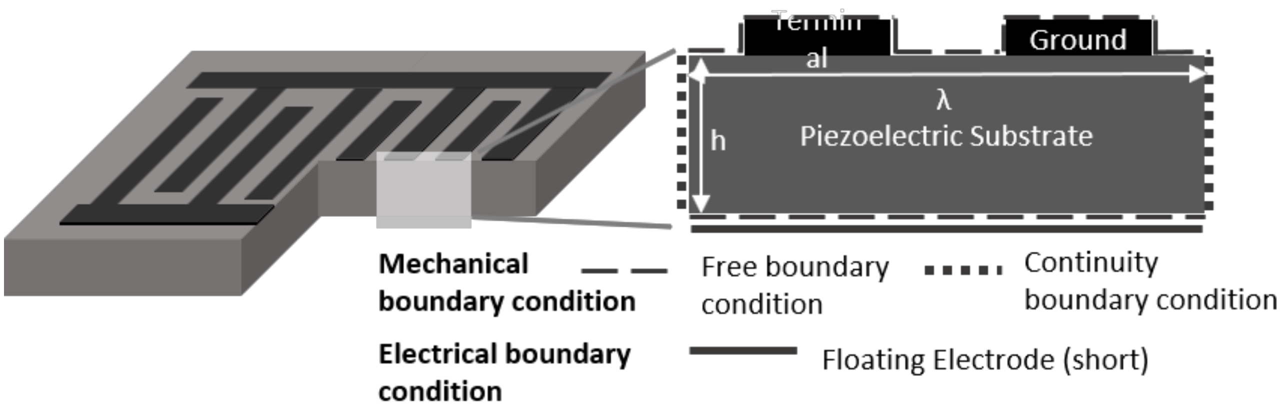

Figure 3.6 Frequency domain model for the ST-cut quartz, with h/λ =1.36

Figure 3.7 shows the frequency response, i.e. the absolute impedance vs frequency curves, of both the two coupling configurations, in the ~11 to 29 MHz range. As it can be noticed, the floating metal layer corresponds to a higher Q factor and a lower absolute impedance values as it offers a better confinement of the electric field across the thickness of the plate: this effect is visible for all the excited modes except for S_2 mode.

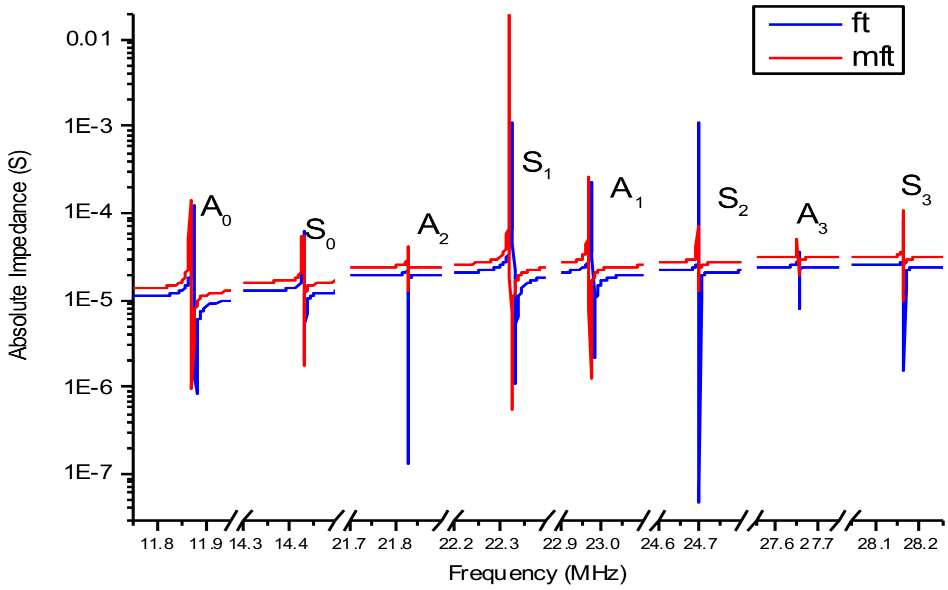

Figure 3.7 Frequency response for ft and mft configuration

3.1.3 Time Domain Analysis

The time domain response of a Lamb mode-based delay line was studied for the first four modes travelling on ST-quartz for h= :350 um, λ = 257 um, which correspond to the h/λ of 1.36. The distance between the IDTs (delay line) is 40 mm. The IDTs have 23 finger pairs with aperture of 20λ.Figure 3.8 shows the model adopted to study the time domain response of a delay line onto ST-quartz.

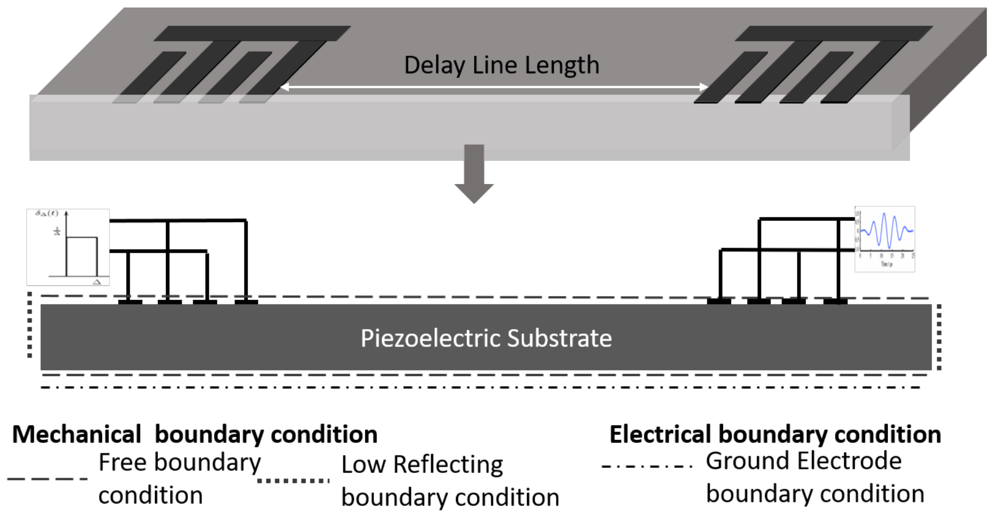

Figure 3.8 Time domain model for a delay line device on ST-cut quartz

Figure 3.9 shows the time response of the first four Lamb modes travelling in the ST-quartz plate: the output voltage at the receiving IDT allows to calculate the group velocity, $v_{gr} = L/\tau$ where τ is the time delay of the mode, and the displacement components of the first eight modes delay line. Figure 3.9(a) shows the output voltage of different mode. The amplitude of output voltage correspond to the electromechanical coupling constant, meaning that the higher the output voltage, the more electrical energy is converted into acoustic energy by the transmitter IDT, and then the acoustic energy is converted back to electrical energy by receiver IDT. Figure 3.9(b) shows the amplitude of longitudianal U1 and transversal U3 on the receiver IDT. As we can see, the S1 mode has dominantly longitudinal component. The A1 mode is also dominantly longitudinal even though it has also noticeable transversal displacement component.

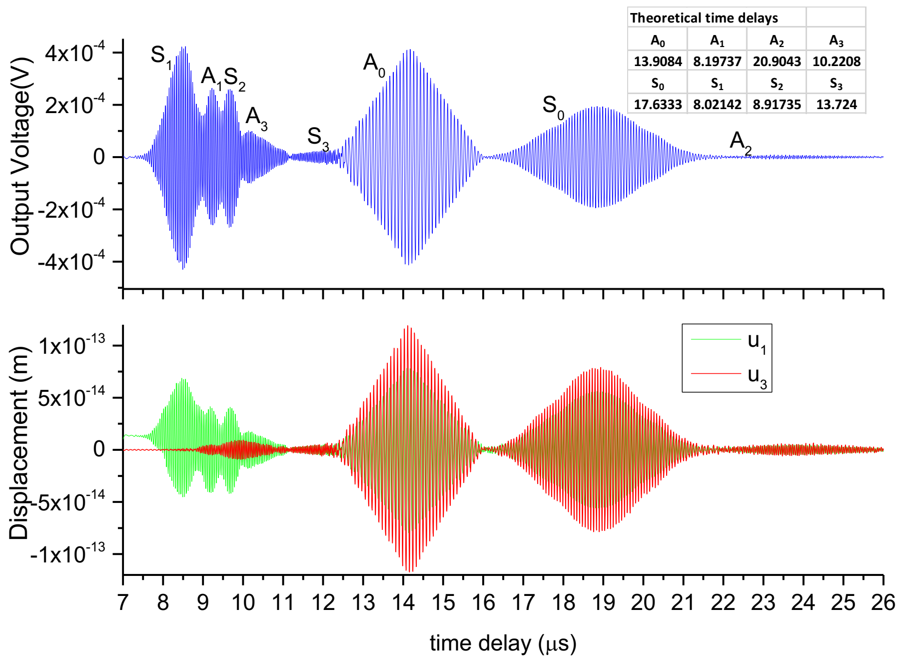

Figure 3.9 Time domain response of the first four modes of a Lamb mode-based delay line onto ST-quartz.

The time domain response is transformed into frequency domain by Fourier transform in MATLAB program, as shown in figure 3.10. The S21 scattering parameter correspond to the ratio between the output and input voltage. The less negative S21 value indicates more energy are transmitted into the receiver IDT, which is related to the K2 and propagation loss. In this simulation, the material is assumed to be lossless, so the K2 is the dominant factor.

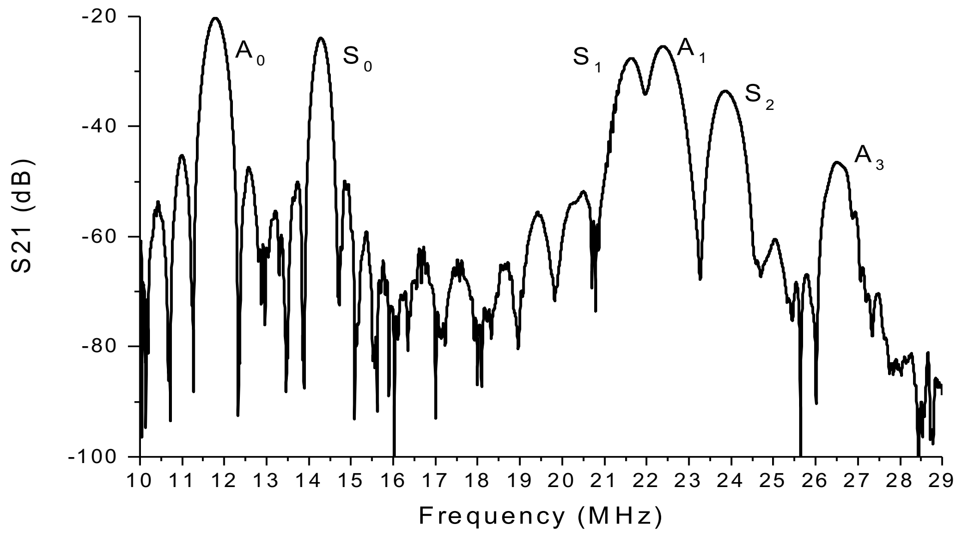

Figure 3.10 Fourier transform of time domain response into frequency domain

3.1.4 Liquid Model

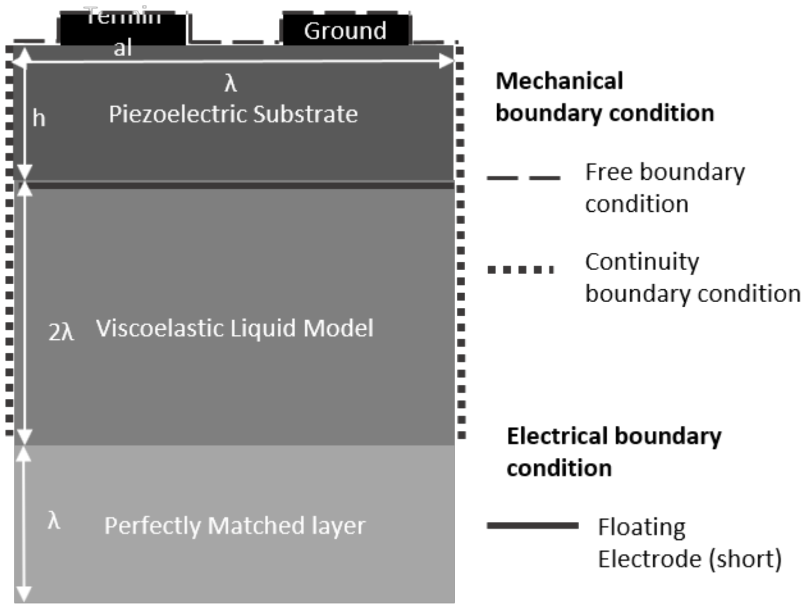

Figure 3.11 Liquid contact model

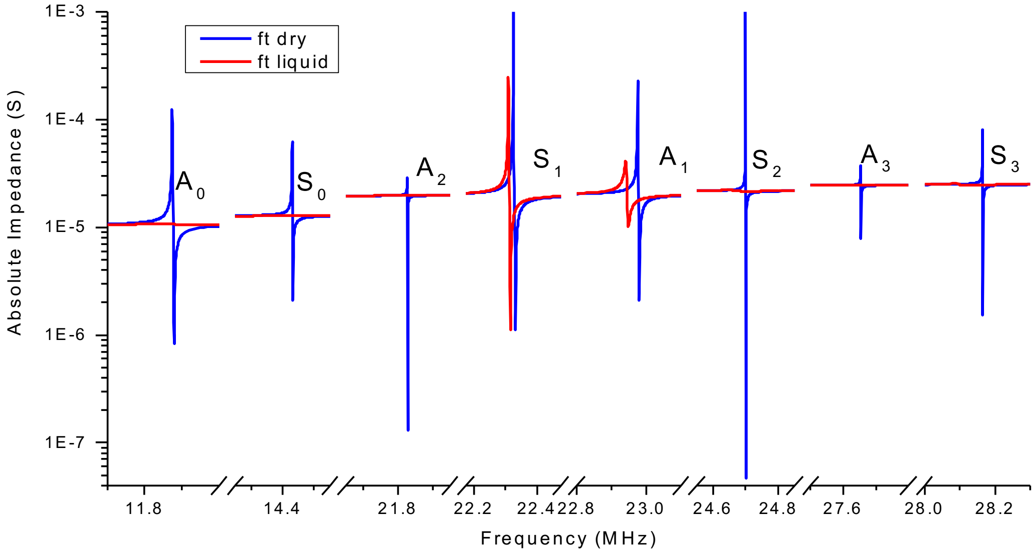

Figure 3.12 Resonator Frequency domain response of dry and liquid

3.1.5 Viscosity Sensor

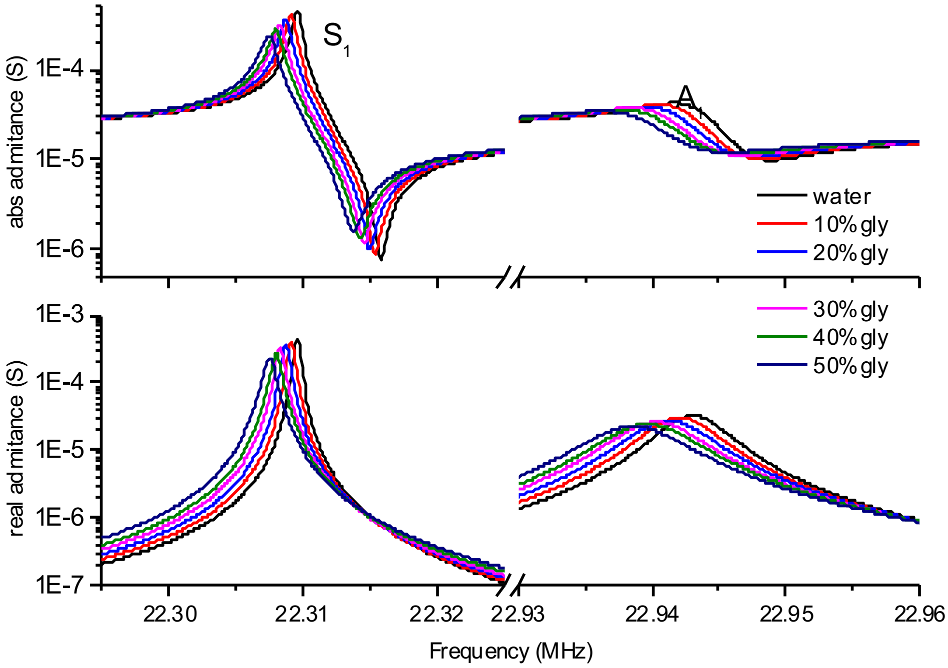

Figure 3.13 Frequency response VS the mass density vs viscosity

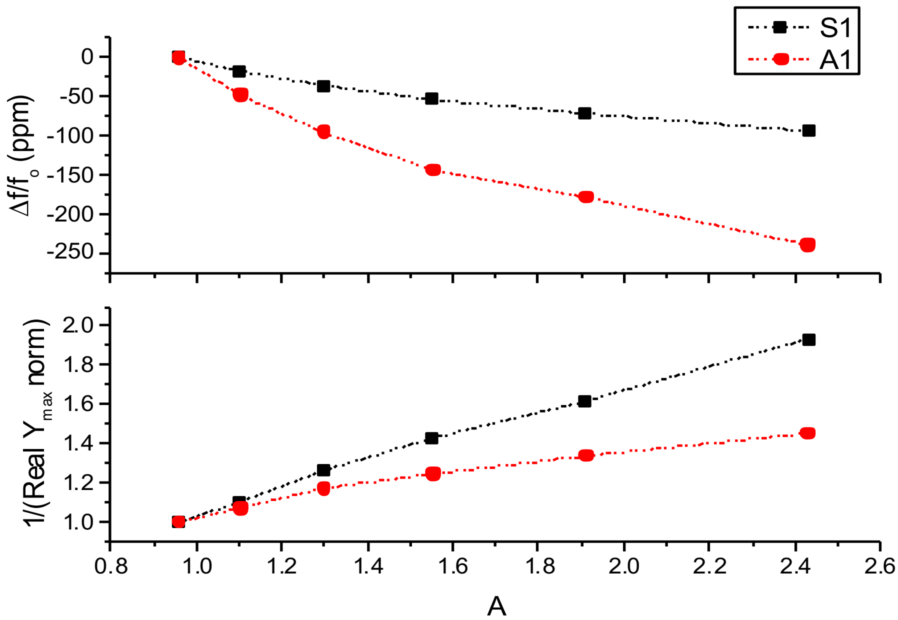

Figure 3.14 Viscosity sensor

3.2 Higher Order Quasi-Longitudinal Lamb Waves in Composite Thin Film Membrane

3.2.1 a-SiC/ZnO

The a-SiC films deposition onto Si(100) substrates from a sintered SiC target by a radio frequency magnetron sputtering system has been demonstrated [11-13] and has the advantage of being compatible with the integrated circuit technology [14]. Piezoelectric wurtzite ZnO thin film technology has been widely used for many years for the fabrication of surface acoustic wave (SAW) devices onto non piezoelectric substrates, such as silicon, glass, and sapphire, to name just a few. When the piezoelectric ZnO film is grown onto high-velocity materials, such as diamond or SiC, it is a promising candidate for high frequency, high sensitivity micro sensors [15]. The aim of the present theoretical calculations and simulations is to investigate the influence of the thickness of both ZnO and a-SiC layers on the performances of a Lamb wave device for liquid sensing applications.

Figure 1a shows the phase velocity dispersion curves of the fundamental and higher order Lamb modes propagating along the isotropic homogeneous a-SiC plate with a thickness of h = 5 μm in contact with air. These modes are represented by two sets of curves, the symmetric (Si) and anti-symmetric (Ai) modes, with i representing the mode order; the blue and red curves refer to the symmetric and anti-symmetric modes. For very small plate thicknesses, the S0 mode velocity approaches the longitudinal bulk acoustic wave velocity in a-SiC. With increasing the plate thickness, the plate becomes a half-space and the A0 and S0 mode velocities tend to approach the velocity of the Rayleigh wave in a-SiC, while the velocities of the non-fundamental modes asymptotically reach the a-SiC transverse bulk acoustic wave velocity.

Lamb-like waves propagate in a homogeneous anisotropic plate and can show three displacement components (longitudinal, shear horizontal, and shear vertical components), depending on the plate crystallographic cut and wave propagation direction. When considering a composite bi-layered plate, the symmetry of the particle displacement components with respect to the mid-plane of the plate is lost, unlike the homogeneous isotropic and anisotropic plate, and the shape of each mode changes with respect to the frequency. As mentioned in Reference [16], the fundamental modes can be considered as quasi-S0 and quasi-A0 (qS0 and qA0) for a limited plate thickness range, while all the other modes can be generically labelled as ith mode.

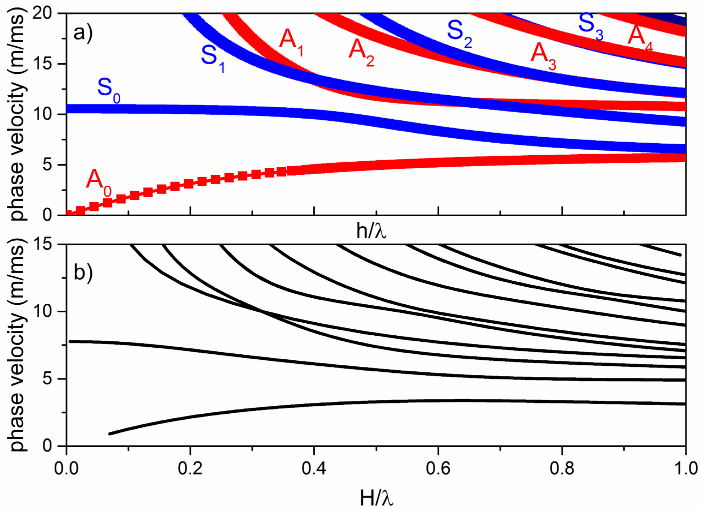

Figure 3.15(a) The phase velocity vs. the plate normalized thickness h/λ of the Lamb modes propagating in a single material plate (a-SiC plate with a thickness of h = 5 µm); (b) The phase velocity vs. the plate normalized thickness H/λ of the Lamb-like modes propagating in a bi-layered plate with a thickness of H = 10 µm (a-SiC/ZnO plate with layers of equal thicknesses).

Figure 3.15b shows the phase velocity dispersion curves of the fundamental and higher order modes propagating along a composite a-SiC/ZnO plate with a total thickness of H = 10 µm. This plate is no longer symmetric with respect to the middle plane, even if the two layers have equal thicknesses (5 µm). The two materials have different physical constants (mass density, elastic, piezoelectric and dielectric constants) and crystal symmetry, thus the mode displacement profiles are no longer simply anti-symmetric or symmetric with respect to the neutral axis. When a ZnO layer is attached to a thick a-SiC plate, the displacement profiles of the Lamb modes in the isotropic a-SiC plate are distorted due to the presence of the ZnO layer; the phase velocity dispersion curves of the composite plate, shown in Figure 1b, have equal color as the distinction between mode types is somewhat artificial. The theoretical phase velocity dispersion curves were calculated utilizing the ZnO and a-SiC material constants available in the literature [12,13,17] and using the COMSOL, DISPERSE [7], and MATLAB software. The shape of the modes travelling in a bi-layered plate are no longer simply anti-symmetric or symmetric with respect to the neutral axis, but are distorted. The mode shape at different points along the same dispersion curve evolves continuously from symmetric to anti-symmetric and vice versa, thus it would be incorrect to label the dispersion curves as quasi symmetric or quasi anti-symmetric. We decided to assign each dispersion curve a number in the order in which they appear along the frequency axis. We investigated the fundamental quasi symmetric mode and two higher order modes that show, for specific thickness-to-wavelength ratio values, a predominant longitudinal polarization (U3 << U1) on the a-SiC layer-free side of the plate. These modes were studied with the aim to design a high frequency electroacoustic device suitable to work in a liquid environment. The latter modes are hereafter named quasi longitudinal modes, qL1 and qL2.

The qS_0 Mode

When a thin ZnO layer is added to the a-SiC plate, the qS0 mode field profile results quite unperturbed for a very small ZnO thickness range. The power transported by the mode along the plate per unit length perpendicular to the propagation direction and per unit time, , was calculated for waves propagating along the x1 direction of the plate, with U1 and U3 being the longitudinal and transverse particle displacement components normalized to the power flow evaluated at the x3 = h/2 surface; ω = 2π·f is the angular frequency, f = vph/λ, ρ is the plate mass density, n is the mode order, and vgr is the group velocity of the mode. The P distribution inside the plate gives information about the location of the peaks of acoustic energy transmission. Figure 3.16 shows the qS0 mode field profile and power flow distribution into the plate depth for a-SiC and ZnO normalized thicknesses equal to 0.1 and 0.05 (λ = 50 μm), respectively; the mode travels at velocity v = 8293 m/s. As can be seen, the longitudinal displacement component U1 is almost constant across the composite plate depth, while U3 is negligible on the a-SiC side of the plate, and it increases slowly up to the ZnO side where it reaches a non-negligible value.

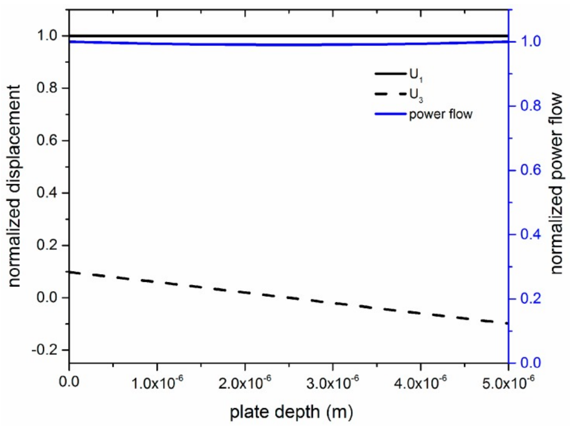

Figure 3.16 The power flow, and the longitudinal and shear vertical particle displacement components, U1 and U3, of the qS0 mode propagating along an a-SiC plate with haSiC/λ = 0.1, covered by a ZnO layer with hZnO/λ = 0.05.

The qL1 and qL2 Modes

As an example, Figure 3.17 and 3.18 show the field profile and the in-plane power flow per unit area for the modes named quasi-longitudinal modes, qL1 and qL2, propagating at a velocity equal to 11,456 and 12,346 m/s, respectively, along the composite plate with a-SiC and ZnO fixed thicknesses (5 and 2.5 µm), for λ = 16.7 and 8.8 µm. The displacement components as well as the power flow have been normalized to their maximum values. As can be seen, these two modes have a very small U3 component at the a-SiC-free surface where U1, as well as the power flow, are at maximum values, thus confirming that these modes are suitable for the development of electroacoustic devices for applications to a liquid environment

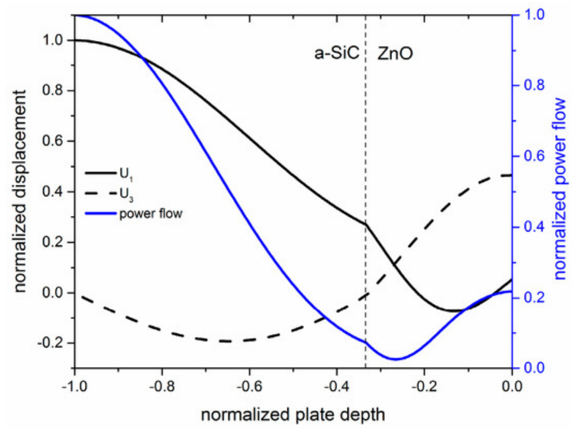

Figure 3.17 The field profile and in-plane power flow per unit area for the qL$_1$ mode propagating along a-SiC and ZnO thicknesses equal to 5 and 2.5 µm, for λ = 16.7 µm.

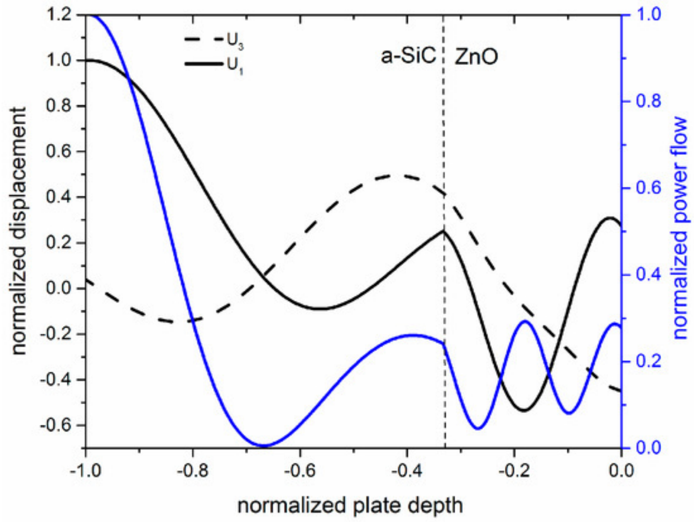

Figure 3.18 The field profile and in-plane power flow per unit area for the qL$_2$ mode propagating along a-SiC and ZnO thicknesses equal to 5 and 2.5 µm, for λ = 8.8 µm.

COMSOL FEM Multiphysics software was employed to simulate the resonance mode shape of the three modes, qS0, qL1, and qL2, propagating in the a-SiC/ZnO composite plate, with and without the liquid contacting the plate surface. 2D piezoelectric device simulation with solid mechanics and electrostatic modules was used for eigen-frequency analysis of the composite plate. The number of degrees of freedom to solve for the mode is minimized by providing periodic boundary conditions to the transmitting interdigital transducer which is a one-finger structure with a total width of one wavelength. Figure 3.19 shows the schematic of the COMSOL model with boundary conditions; as the liquid was modeled as a half space layer, a perfectly matched layer (PML) was added so that the wave propagating in the liquid was not reflected back to the plate. Figure 3.20 shows the U1 and U3 components of the three modes travelling along the composite plates in air; the a-SiC and ZnO thicknesses are fixed (5 and 2.5 μm), and the wavelength is λ = 50, 16.7 and 8.8 μm for the three modes.

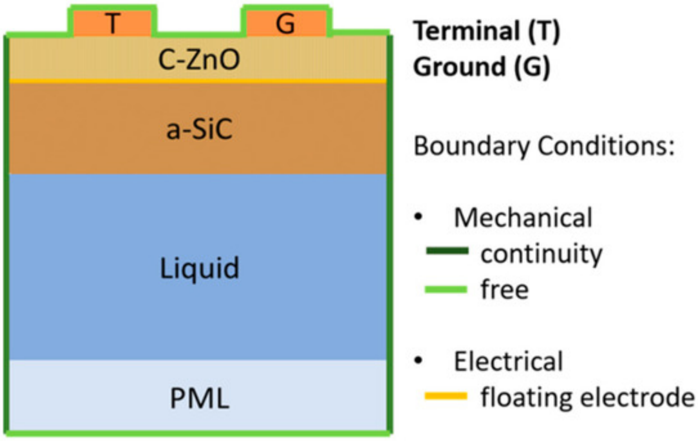

Figure 3.19. The FEM schematic.

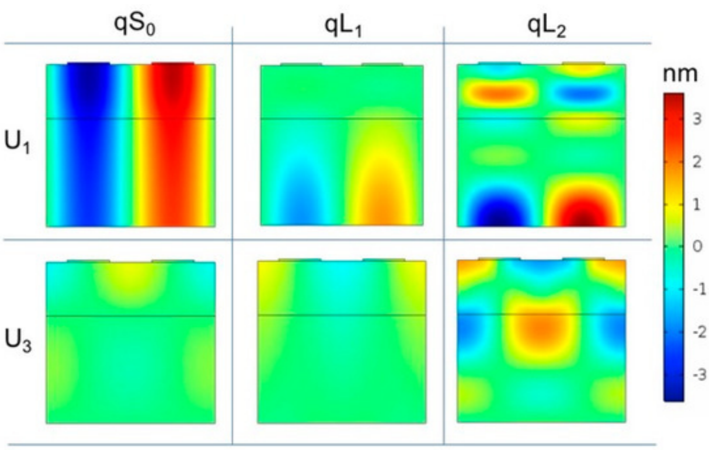

Figure 3.20 The U_1 and U_3 components of the three modes travelling along the composite plate in air with a-SiC and ZnO fixed thicknesses (5 and 2.5 μm), the plate width equal to one λ, and λ = 50, 16.7, and 8.8 μm for qS_0, qL_1, and qL_2, respectively.

Figure 3.21 shows the displacement components U1 and U3 of the three modes propagating along the a-SiC/ZnO plate that contacts the liquid environment from the a-SiC side of the plate. As can be seen, the acoustic energy is confined inside the plate. The liquid was modelled as a linear isotropic viscoelastic material with independent elastic constants, the bulk (K) and shear (G) moduli, and two independent bulk (η_b) and shear viscosities (η_v) from Reference [18].

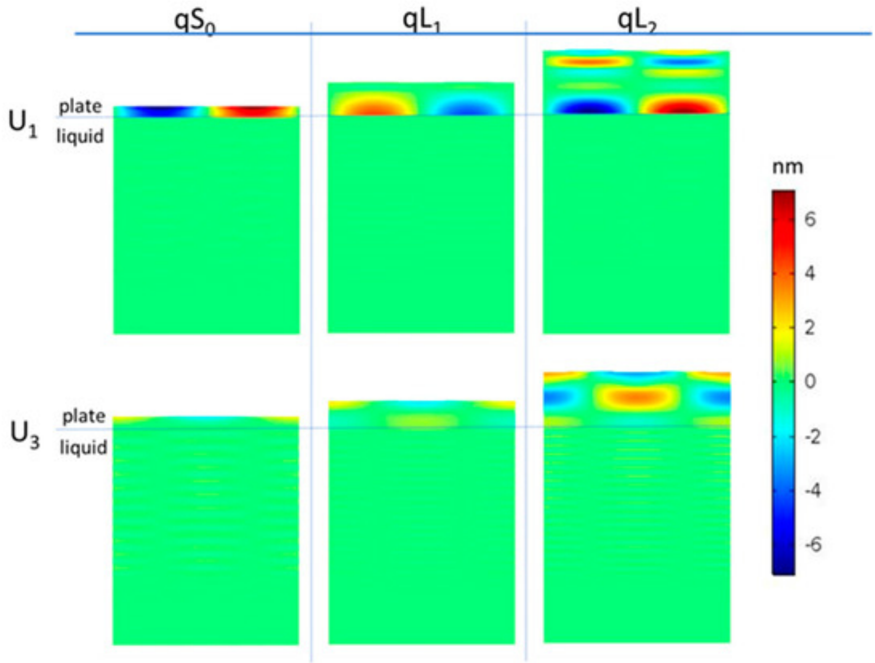

Figure 3.21 The displacement components U_1 and U_3 of the three modes propagating along the a-SiC/ZnO plate that makes contact with the liquid. The a-Sic and ZnO layers have a thickness equal to 5 and 2.5 µm; the plate width is equal to one λ; the H/λ = 0.15, 0.45, and 0.85, for qS_0, qL_1, and qL_2, respectively.

<u>Viscosity Sensor</u>

When a liquid contacts the acoustic waveguide, the in-plane particle displacement component of the acoustic mode couples to a very thin viscous boundary layer of thickness, where η and are the liquid viscosity and mass density. The viscous liquid was supposed to be a mixture of water and glycerol; the fraction of glycerol by volume ranged from 0 (only water) to 0.6, and the ranged from 0.95 to about 15 kg·m−2·s−0.5 [18]. The effects of both the viscosity η and the mass density of the water/glycerol mixture on the wave velocity and IL was analyzed numerically. The real and imaginary parts of the phase velocity (vi and vr) of the three modes were calculated for different concentrations of the water/glycerol mixtures. The relative changes of the phase velocity Δv/v0 and the IL as a function of are shown in Figure 3.22(a) and (b). It was assumed that the examined glycerol-water mixture was in contact with the a-SiC surface of the composite plate.

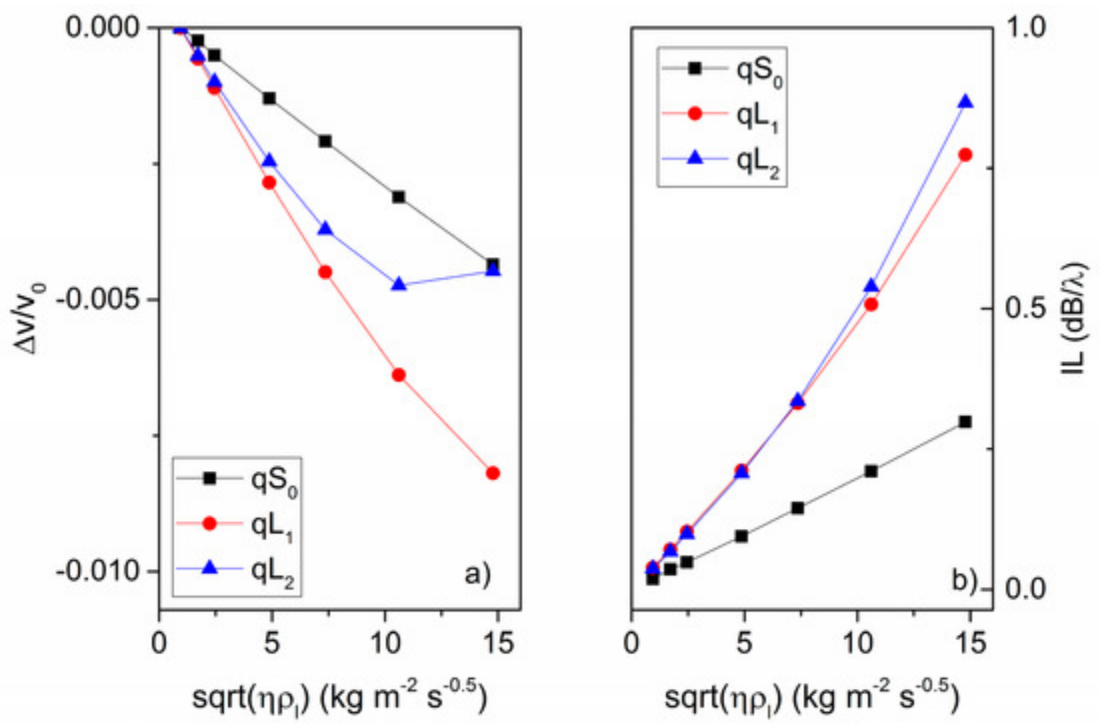

Figure 3.22 (a) The wave relative velocity change and (b) the IL vs. the ηρl−−−√, where η and ρl are the viscosity and density of a water/glycerol mixture contacting the a-SiC side of the composite plate.

As shown in Figure 3.22, at low values of viscosity, the fluid behaves as a Newtonian liquid with Δv/v0 and IL proportional to . This is observed for the qS0 and qL1 modes, whose time scale (wave period equal to about 6 and 1.5 ns) is far larger than the fluid relaxation time τ = η/μ (where μ the liquid shear modulus) for the = 0.9 to 15 abscissa range. The relative velocity shift of the qL2 mode is linearly dependent on for low viscosity values, and is reversed for glycerol/water percentage ≥44%, as τ becomes close to the wave period (0.8 ns) of the mode [24,25]. The relative resonant frequency shift and the IL shift per unit change in the square root of the density-viscosity product are equal to = −316 ppm·m2·s0.5·kg−1 and = 0.02 dB/λ·m2·s0.5·kgr−1 over the range of 0 to 60% glycerol in water, for the qS0 mode; = −702 ppm m2·s0.5·kgr−1 and = 0.045 dB/λ for the qL1 mode, and = −579 ppm·m2·s0.5·kgr−1 and = 0.046 dB/λ·m2·s0.5·kgr−1 for the qL2 mode, in the low viscosity region from 0 to 44% glycerol in water. For a Lamb wave delay line with two IDTs with Nopt finger pairs, 3Nopt·λ IDTs center-to-center distance, a unit change in the square root of the density-viscosity product will produce an IL increase equal to 0.3, 1.35, and 2.76 dB·m2·s0.5·kg−1.

3.2.2 SiN/AlN

Matlab, Disperse, and COMSOL Multiphysics simulations were used to study the dispersion curves and the acoustic field profile of the fundamental and higher order modes traveling in SiN/AlN thin suspended membranes, for fixed SiN and AlN thicknesses (200 nm and 1.4 μm) and variable wavelength λ. Two higher order modes, qS1 and qS2, were found that are slowly dispersive and have dominant longitudinal particle displacement component, at AlN thickness-to-wavelength ratio hAlN/λ = 0.8 and 1.6 respectively. Figure 3 shows the dispersion curves of the Lamb modes travelling along the composite plate AlN/SiN with total thickness Htotal = 1.6 μm, being 1.4 μm and 0.2 μm the AlN and SiN thicknesses. Figure 3.23 shows the dispersion curves of the Lamb modes travelling along the composite plate AlN/SiN with total thickness Htotal = 1.6 μm, being 1.4 μm and 0.2 μm the AlN and SiN thicknesses.

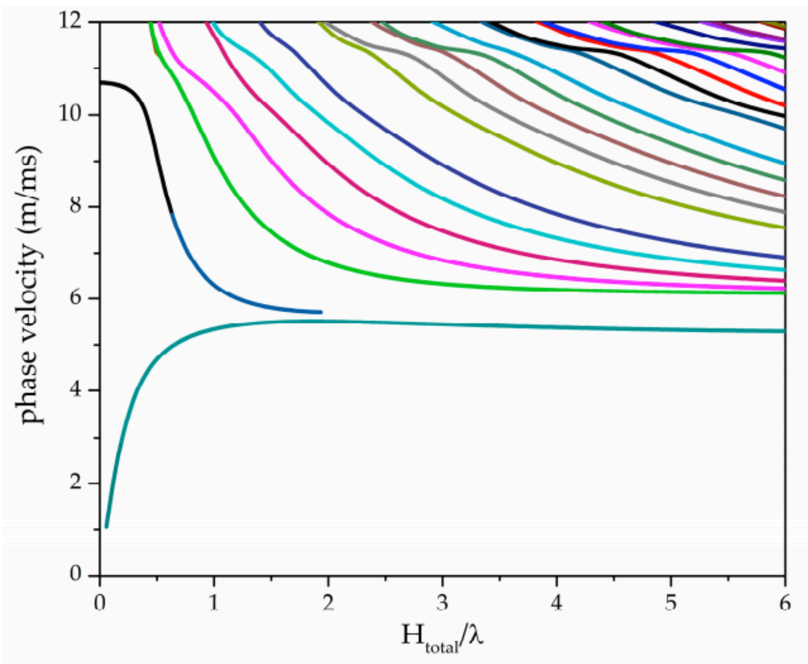

Figure 3.23 The dispersion curves of the Lamb modes travelling along the composite plate AlN/SiN with total thickness 1.6 μm, being 1.4 μm and 0.2 μm the AlN and SiN thicknesses.

Three modes were identified that travel along the SiN/AlN composite plate and that are suitable for liquid sensing applications. Figure 3.24a–c shows the field profile of these three quasi symmetric modes, qS0, qL1, and qL2: the corresponding Htotal/ λ values are 0.08, 0.80 and 1.6. As it can be seen, U3 is very low with respect to U1 (U3 << U1) on one plate side that is thus the one suitable for contacting a liquid environment.

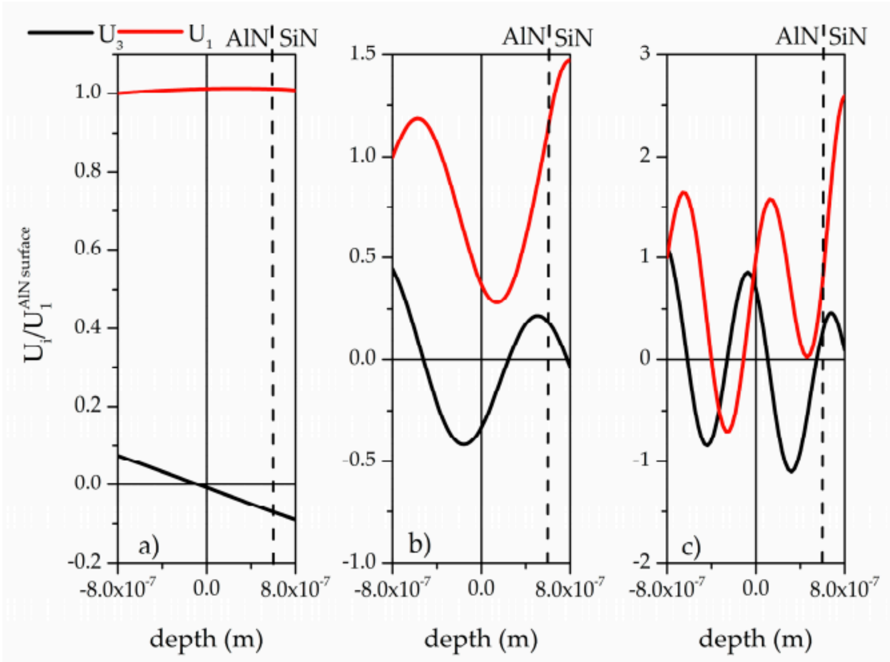

Figure 3.24 The field profile of the (a) qS0; (b) qL1; and (c) qL2 modes in air.

COMSOL FEM Multiphysics software was employed to simulate the three modes propagation along the composite plate with the liquid (water) contacting the plate surface. 2D piezoelectric device simulation with solid mechanics and electrostatic modules was used for eigen-frequency analysis of the composite plate. The number of degrees of freedom to solve for the mode is minimized by providing periodic boundary conditions to the transmitting IDTs which is a one-finger structure with a total width of one λ. Figure 5 shows the field profile of the three modes in the SiN/AlN plate contacting the liquid environment (water) from the SiN side of the plate. As can be seen, the acoustic energy is confined inside the plate.

COMSOL FEM Multiphysics software was employed to simulate the three modes propagation along the composite plate with the liquid (water) contacting the plate surface. 2D piezoelectric device simulation with solid mechanics and electrostatic modules was used for eigen-frequency analysis of the composite plate. The number of degrees of freedom to solve for the mode is minimized by providing periodic boundary conditions to the transmitting IDTs which is a one-finger structure with a total width of one λ. Figure 3.25 shows the field profile of the three modes in the SiN/AlN plate contacting the liquid environment (water) from the SiN side of the plate. As can be seen, the acoustic energy is confined inside the plate.

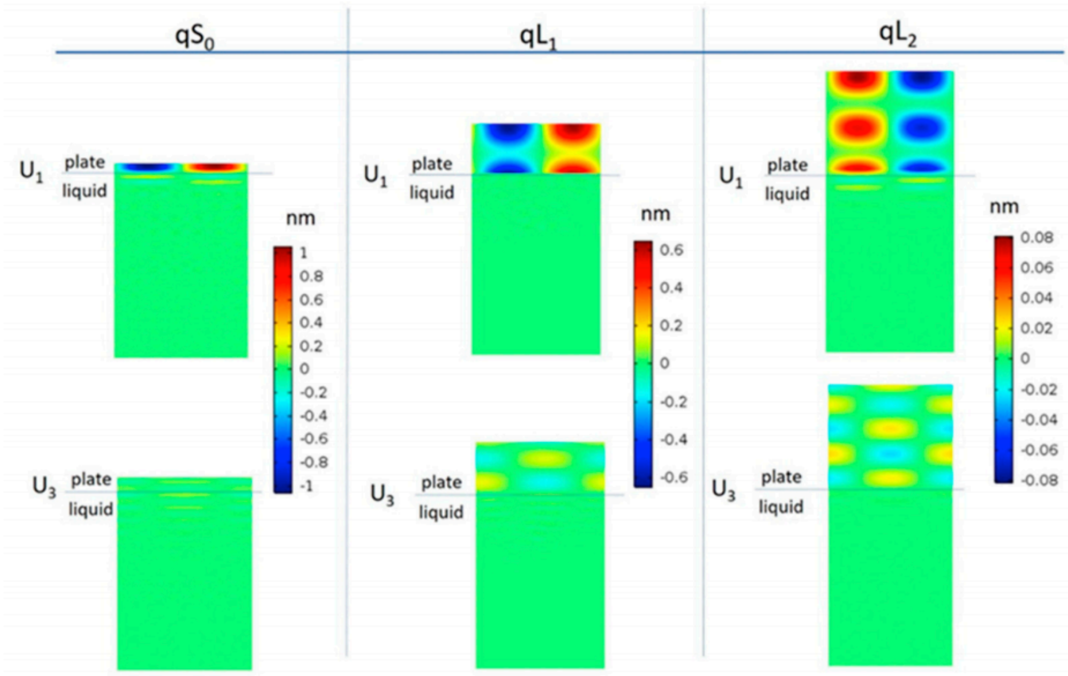

Figure 3.25. The FEM of the field profile for the qS0, qL1 and qL2 modes.

__Viscosity Sensor__

When a liquid contacts the acoustic waveguide, the in-plane particle displacement component of the acoustic mode couples to a very thin viscous boundary layer of thickness $\delta = (2\eta/\omega\rho l)0.5$, where η and ρl are the liquid viscosity and mass density. The viscous liquid was supposed to be a mixture of water and glycerol; the fraction of glycerol by volume ranged from 0 (only water) to 0.53, and the ꝏçρη□ ranged from 0.95 to about 11 kg·m−2·s−0.5. The real and imaginary parts of the phase velocity of the three modes were calculated for different concentrations of the water/glycerol mixtures. The relative changes of the phase velocity $\Delta v/v0$ and the IL as a function of ꝏçρη□ are shown in Figure 3.26a,b where it is assumed that the examined glycerol-water mixture contacts the SiN surface of the composite plate. The qS0 mode has a linear IL and relative velocity shift behavior vs. the ꝏçρη□ values in the studied viscosity range: its time period (2.06 ns) is far larger than the fluid relaxation time $\tau = \eta/\mu$ (where μ is the liquid shear modulus) for the 0.9 to 11 abscissa value. The qS0 velocity and attenuation sensitivities are −0.0015 m2 s0.5 kg−1 and 0.1038 dB/λ m2 s0.5 kg−1. The relative velocity shift of the qL1 mode is linearly dependent on ѡçρη□ only for low viscosity values, and its slope is reversed for glycerol/water percentage ≥ 20%, as τ becomes close to the wave period (0.2 ns) of the mode. The relative velocity shift of the qL2 mode is linearly dependent on ѡçρη□ for very low viscosity values, and is reversed for glycerol/water percentage ≥ 10%, as τ becomes close to the wave period (0.099 ns) of the mode.

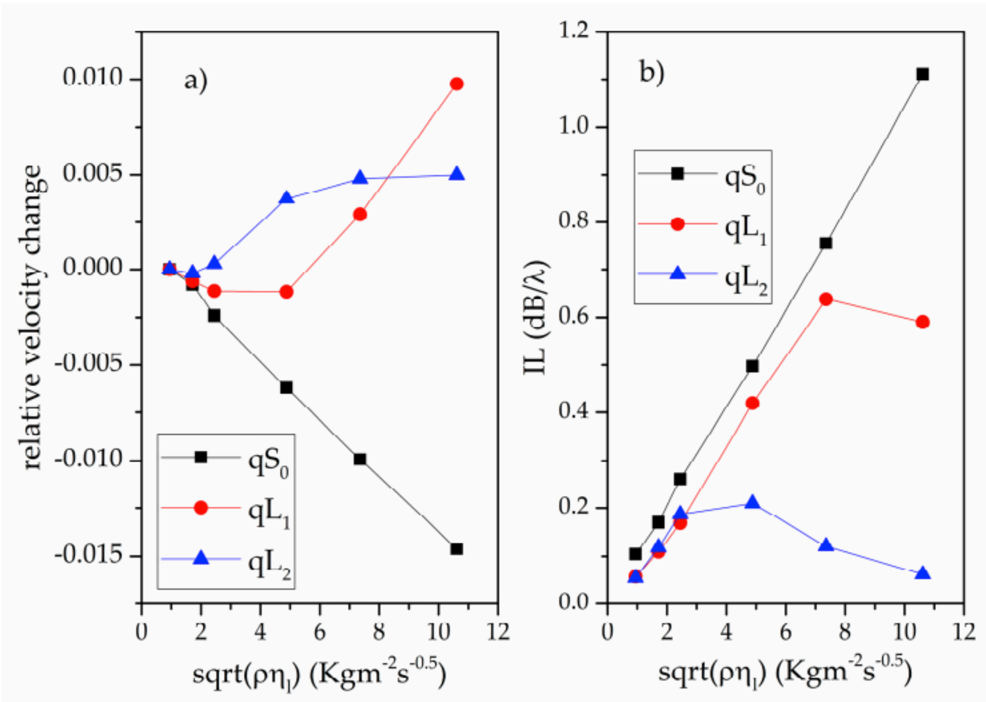

Figure 3.26. (a) The wave relative velocity change and (b) the IL vs. the square root of the viscous liquid mass density-viscosity product; the water/glycerol mixture is supposed to contact the SiN side of the composite plate.

Bibliography

[1] White, R. M., and S. W. Wenzel. "Fluid loading of a Lamb-wave sensor." Applied Physics Letters 52.20 (1988), pp. 1653-1655.

[2] Wu, Junru, and Zhemin Zhu. "Sensitivity of Lamb wave sensors in liquid sensing." IEEE transactions on ultrasonics, ferroelectrics, and frequency control 43.1 (1996): 71-72.]

[3] Laurent, Thierry, et al. "Lamb wave and plate mode in ZnO/silicon and AlN/silicon membrane: Application to sensors able to operate in contact with liquid." Sensors and Actuators A: Physical 87.1 (2000), pp. 26-37.

[4] Mirea, Teona, and Ventsislav Yantchev. "Influence of liquid properties on the performance of S0-mode Lamb wave sensors: A theoretical analysis." Sensors and Actuators B: Chemical 208 (2015): 212-219.
[5] Mirea, Teona, et al. "Influence of liquid properties on the performance of S0-mode Lamb wave sensors II: Experimental validation." Sensors and Actuators B: Chemical 229 (2016): 331-337.
[6] Caliendo, Cinzia. "Longitudinal Modes along Thin Piezoelectric Waveguides for Liquid Sensing Applications." Sensors 15.6 (2015): 12841-12856.
[7] N. Pavlakovic, M. J. S. Lowe, D. N. Alleyne, and P. Cawley, Disperse: A general purpose program for creating dispersion curves, in D. O. Thompson and D. E. Chimenti editors, Review of Progress in Quantitative NDE, vol.16, pp. 185-192, Plenum Press, New York, (1997).
[8] E. L. Adler, J. K. Slaboszewics, G. W. Farnell, and C. K. Jen, IEEE Trans. Ultrason. Ferroelectr. Freq. Control 37, 215 (1990).
[9] Gulyaev, Yury V. "Properties of the Anisimkin Jr.'modes in quartz plates." IEEE transactions on ultrasonics, ferroelectrics, and frequency control 54.7 (2007).
[10] Anisimkin, Ivan V. "New type of an acoustic plate mode: Quasi-longitudinal normal wave." Ultrasonics 42.10 (2004): 1095-1099.
[11] Caliendo, C. Theoretical investigation of high velocity, temperature compensated Rayleigh waves along AlN/SiC substrates for high sensitivity mass sensors. Appl. Phys. Lett. 2012, 100, 021905.
[12]Vashishta, P.; Kalia, R.K.; Nakano, A. Interaction potential for silicon carbide: A molecular dynamics study of elastic constants and vibrational density of states for crystalline and amorphous silicon carbide. J. Appl. Phys. 2007, 101, 103515.
[13] Nalwa, H.S. Silicon-Based Material and Devices, Properties and Devices, Vol. 1 Materials and Processing, Chapter 1, Optical, Structural and Electrical Properties of Amorphous Silicon Carbide Films; Academic Press: Cambridge, MA, USA, 2001
[14] Zamani, H.; Lee, S.W.; Avishai, A.; Zorman, C.A.; Sankaran, R.M.; Feng, P.X.L. Focused Ion Beam (FIB) Nanomachining of Silicon Carbide (SiC) Stencil Masks for Nanoscale Patterning. Mater. Sci. Forum 2012, 717–720, 889–892
[15] Caliendo, C.; Castro, F. Advanced Bulk and Thin Film Materials for Harsh Environment MEMS Applications. In Anti-Abrasive Nanocoatings: Current and Future Applications; Aliofkhazraei, M., Ed.; Woodhead Publishing Reviews, Mechanical Engineering; Woodhead Publishing: Sawston, UK, 2015
[16] Lin, C.-M.; Chen, Y.-Y.; Felmetsger, V.V.; Senesky, D.G.; Pisano, A.P. AlN/3C-SiC composite plate enabling high-frequency and high-Q micromechanical resonators. Adv. Mater. 2012, 24, 2722–2727.
[17] Slobodnik, A.J., Jr.; Conway, E.D.; Delmonico, R.T. Air Force Cambridge Research Laboratories; Report No. AFCRL-TR-73-0597; U.S. Department of Commerce: Washington, DC, USA, 1973.
[18] Slie, W.M.; Donfor, A.R., Jr.; Litovitz, T.A. Ultrasonic Shear and Longitudinal Measurements in Aqueous Glycerol. J. Chem. Phys. 1966, 44, 3712.

CHAPTER 4

DEVICES BASED ON HIGHER ORDER QUASI-LONGITUDINAL LAMB WAVES: EXPERIMENTAL RESULT

In this chapter, the microfabrication techniques are described, specifically for the EBL for the IDT patterning and sputtering of piezoelectric thin film. The fabrication process flow of ST-cut Quartz and SiN/AlN Lamb waves devices are described followed by the characterisation result.

Related Publications:

Caliendo, Cinzia, **Muhammad Hamidullah**, and Farouk Laidoudi. "Amorphous SiC/c-ZnO-Based Quasi-Lamb Mode Sensor for Liquid Environments." Sensors 17.6 (2017): 1209.

Caliendo, Cinzia, Ennio Giovine, and **Muhammad Hamidullah**. "Theoretical Study of Quasi-Longitudinal Lamb Modes in SiN/c-AlN Thin Composite Plates for Liquid Sensing Applications." Multidisciplinary Digital Publishing Institute Proceedings. Vol. 2. No. 3. 2017.

4.1 Microfabrication Techniques

Various fabrication techniques have been performed during this thesis. The two most important fabrication tools and techniques for this thesis are the use of electron beam lithography (EBL) to pattern the IDT and the deposition of c-axis piezoelectric thin film with RF magnetron sputtering system.

4.1.1 Electron Beam Lithography

The EBL is a microfabrication process technique of scanning a focused beam of electrons into a surface covered with an electron sensitive film, called electron beam resist or e-resist. Similar with the photoresist in photolithography process, the e-resist is sensitive to the electron beam depending on the type of the e-resist. For positive e-resist, such as Polymethyl methacrylate (PMMA), the exposed area is becoming more soluble to the chemical developer, while for the negative e-resist such as ma-N 2400, the exposed area is becoming harden and becoming less soluble to the chemical developer. In opposed to photolithography process, the EBL process is direct writing process thus doesn't require mask as in photolithography process. EBL capable to achieve 20nm resolution, much higher resolution than photolithography process with typical minimum resolution in a range of one micrometer. This is because the electron wavelength is much smaller than ultraviolet (UV) light that is used for lithography process. The drawback of EBL process is it require process time especially when larger area is required for patterning, thus it is not really suitable for large-scale manufacturing. However, since the mask is not needed, the EBL process is suitable for small volume and device prototyping.

The EBL system in the Institute for Photonic and Nanotechnologies, CNR Rome is used for device fabrication in this thesis, as shown in figure 4.1. The EBL is based on field emission gun (FEG) system with the 100kV acceleration voltage. It has 8nm beam diameter with overlay accuracy of less than 50nm. The maximum block size for exposure is 560nm with 10 MHz frequency. The system is also equipped with laser interferometer (λ/120-5nm), a pull-in system and the laser height sensor. It can process up to 4 inch wafer and can also be used for mask writing and marker alignment.

Figure 4.1 EBL system

In this thesis, a process to do EBL on a thin film suspended membrane is developed to be able to fabricate a thin film Lamb wave device without deep reactive ion etching (DRIE) process to etch the backside silicon (more detail in the subchapter 4.1.3). The 200nm silicon nitride (SiN) suspended membrane on silicon frame samples were purchased from Silson as shown in figure 4.2(a). The size of the silicon frame is 5x5 mm^2 with the centre membrane size of 1.5x1.5 mm^2. Since the EBL process is performed under vacuum pressure, it is important to maintain equal pressure above and below the membrane to prevent the bending of the thin film. To do so, the sample was placed on the chuck with the groove as shown in figure 4.2(b). After the e-beam writing, the PMMA is developed, followed by the deposition of 10 nm titanium and 90 nm gold (Au). Figure 4.3(c) shows the IDT patterned on the SiN thin film after lift-off process.

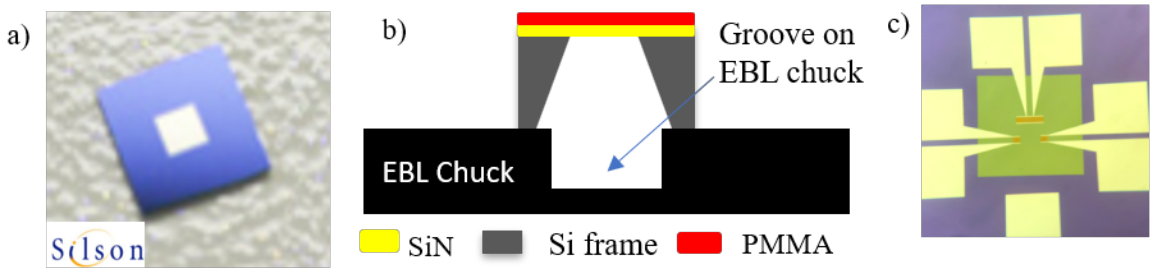

Figure 4.2 EBL on SiN thin film

4.1.2 Radio Frequency Magnetron Sputtering

Another important microfabrication technique and tool during the thesis is the radio frequency (RF) magnetron sputtering system for thin film deposition. Magnetrons are a class of cold cathode discharge devices used generally in a diode mode. In this system, the plasma is initiated between the cathode and the anode at pressures in the mTorr range by the application of a RF high voltage. The plasma is sustained by the ionization caused by secondary electrons emitted from the cathode due to ion bombardment which are accelerated into the plasma across the cathode sheath. The system is suitable for low-cost and easy control method for film growth, especially suitable for large-scale film deposition.

The RF magnetron sputtering system in IFN-CNR Rome is shown in figure 4.3. The vacuum sputtering system was prepared by ONVAC Process company with 4 RF magnetron source so that for different targets can be uploaded and deposited in the same vacuum cycles. The system has two pump system, the first system is a primary rotary pump system work up to 10^{-3} Torr, which will be followed by the turbomolecular pump system to achieve a very low vacuum in range of 10^{-3} Torr. The system has three gas line10-3 Torr: Argon (Ar), Oxygen (O_2) and Nitrogen (N_2). Both metal and dielectric thin film can be deposited using this system. Piezoelectric thin film of aluminium nitride (AlN) can be deposisted by using Al target and a reaction with N_2 gas at specific sputtering condition. Similarly, the zinc oxide (ZnO) can be also deposited using Zn target and O_2.

Figure 4.3 RF Magnetron Sputtering System

The thin film deposition process was performed to obtain the c-axis inclined AlN and ZnO film. The films were deposited on silicon substrate and Scanning Electron Micrsocope (SEM) was used to inspect the structure of the film. Composite thin film of a-SiC and ZnO layer is shown in figure 4.4 and AlN thin film deposited on silicon substrate is shown in figure 4.5.

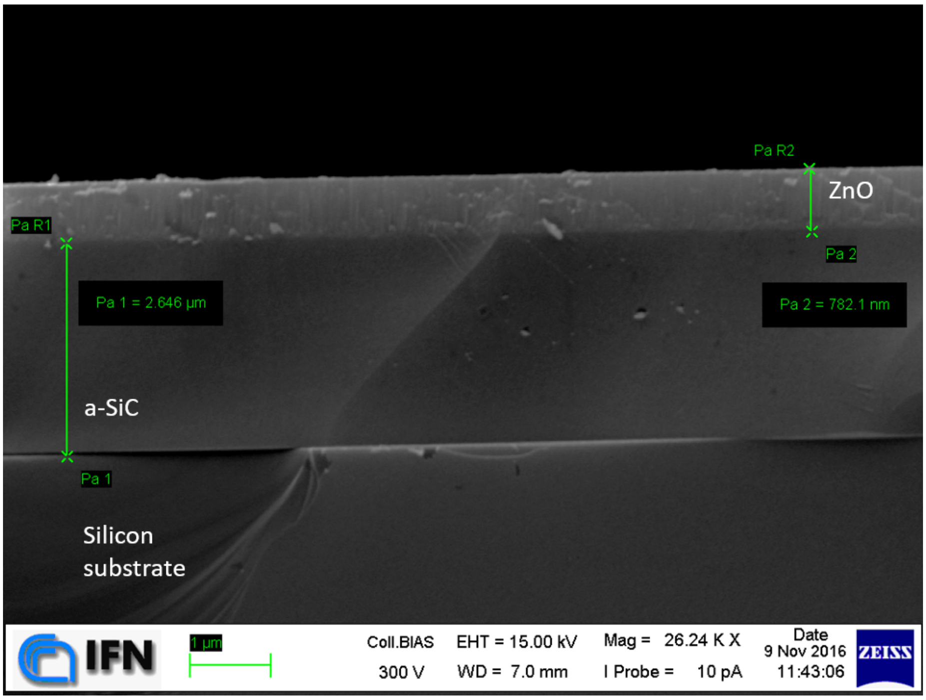

Figure 4.4 SEM of a-SiC/ZnO

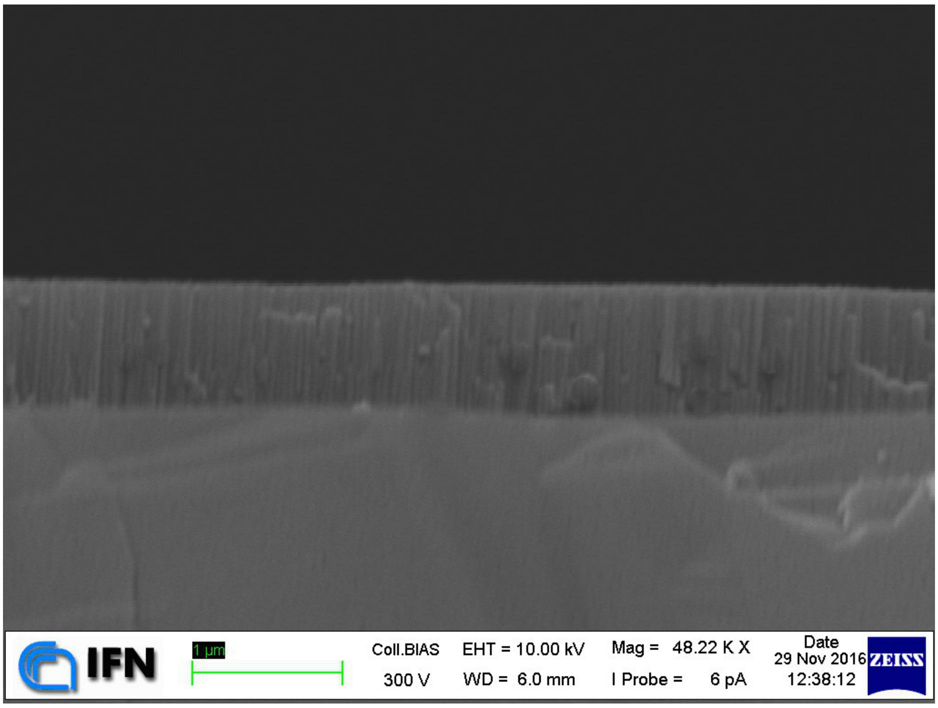

Figure 4.5 SEM of AlN on Silicon

Furthermore, a process to deposit AlN piezoelectric thin film on a thin 200 nm suspended SiN membrane was developed to obtain a stress-free "island" of AlN thin film. As shown in figure 4.6(a), a deposition of AlN on the SiN membrane creates a large stress especially on the edges of the membrane connected to the silicon frame. Hard mask was used to deposit an "island" structure as shown in figure 4.6(b). The more detail on thin film lamb wave fabrication process will be described in subchapter 4.1.3

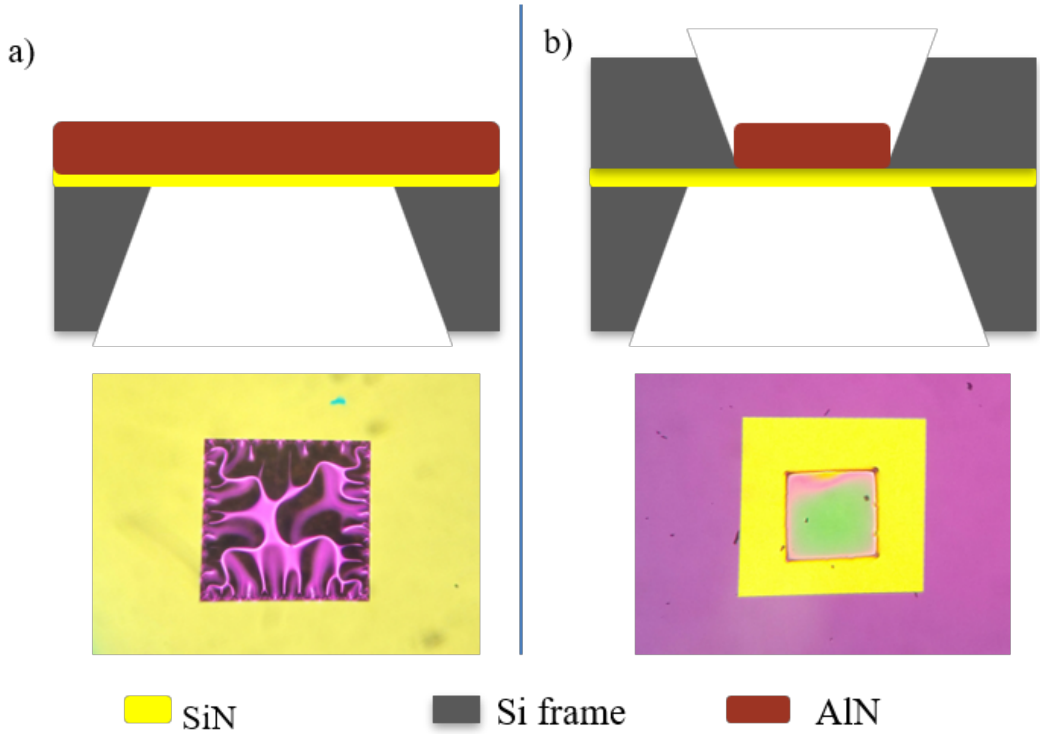

Figure 4.6 AlN deposition on SiN suspended membrane

4.1.3 Device Fabrication Process flow

The first fabrication of Lamb waves devices was performed on ST-cut Quartz propagation with the process flow shown in figure 4.7. Firstly, 3 inch ST-cut Quartz substrate with the thickness of 350 um was cleaned by Piranha cleaning (figure 4.7(a)), followed by the spin coating of PMMA at the speed of 3000 rpm to achieve the thickness of 500nm (figure 4.7(b)). The PMMA was placed on the hot plate at the temperature of 170C for 5minutes. The EBL was used to pattern the IDT The IDTs for delay line was designed to obtain the h/λ ratio of 1.36, equal to the wavelength of 257 um, and the equal finger and space with of $\lambda/4$= 64.25 um. The IDTs have 23 fingers pairs with the aperture of 20λ. The delay line distance is 40mm.

After the development process using MBIK: IPA solution with 1:2 ratio for 120s (figure 4.7(c))., the short 02 plasma cleaning process was performed to remove the PMMA residue, followed by the deposition of 10nm Ti and 90nm Au by sputtering process (figure 4.7(d)). The lift-off process was performed by immersing the substrate into acetone solution to remove the remaining PMMA and to obtain the final IDTs pattern on the ST-cut Quartz substrate (figure 4.7(e)). The final fabricated IDTs micrograph image is shown in figure 4.6

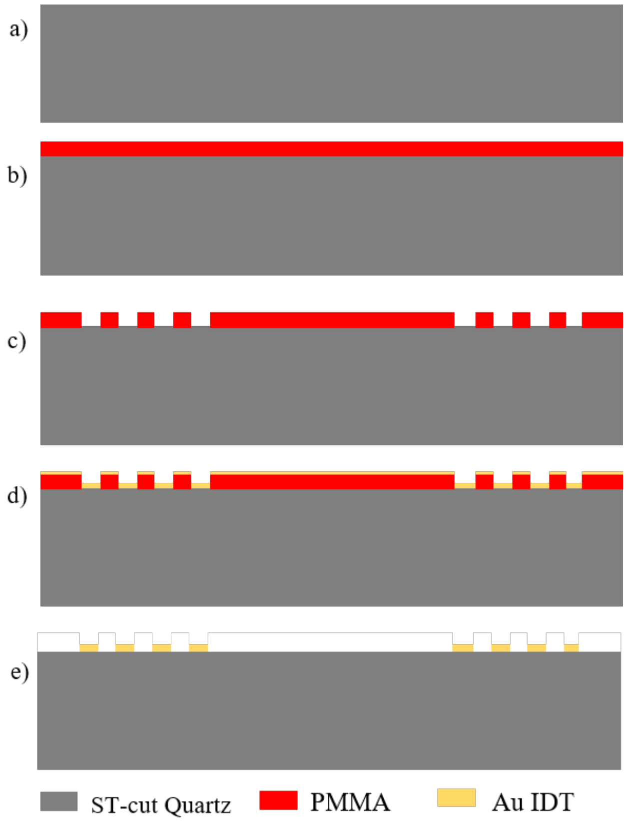

Figure 4.5 Process flow of ST-cut Quartz Lamb waves devices

4.6 The delay line on ST-cut Quartz substrat

The second fabrication process was performed to obtain the thin film Lamb wave devices with the process flow shown in figure 4.6 and the fabricated device shown in figure 4.7

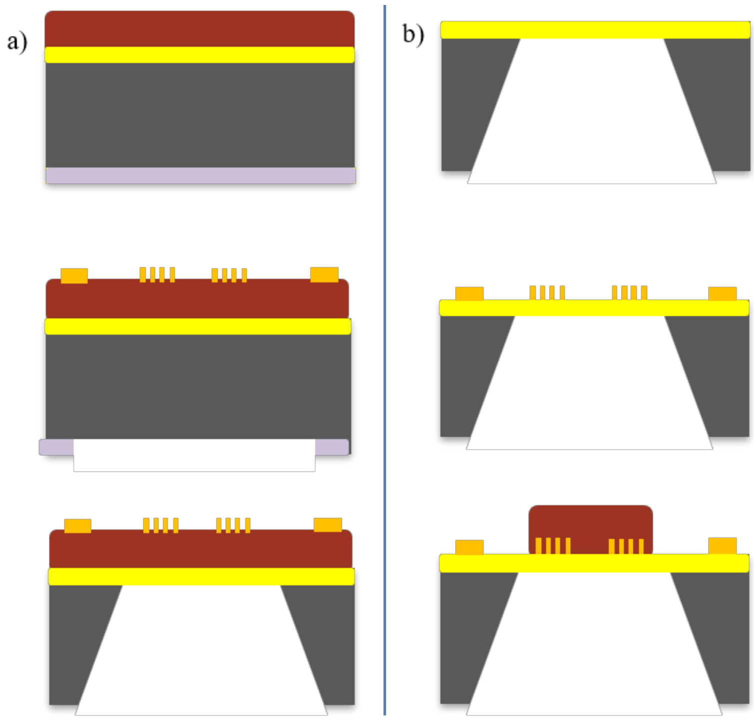

Figure 4.6 Process flow of SiN/AlN

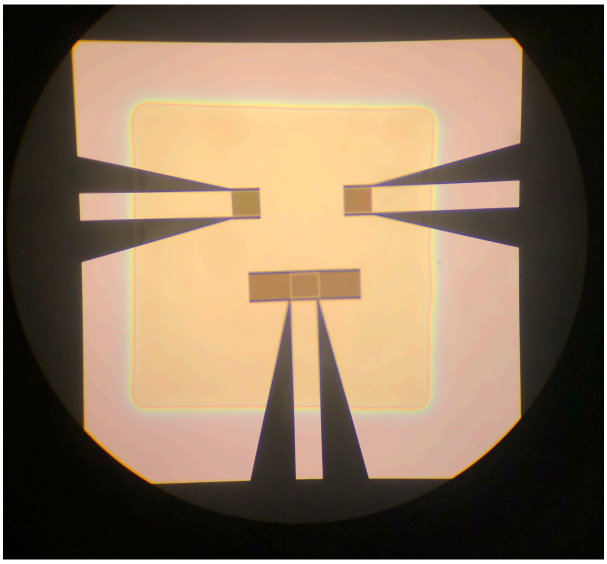

Figure 4.7 Fabricated SiN/AlN Lamb waves devices

4.2 Characterisation Result

4.2.1 ST-cut Quartz Lamb waves

The device was mounted on a PCB with a rectangular through hole (x mm by y mm) in the center: the quartz plate is sealed by silicone to the PCB in order to separate the two plate sides and to prevent the IDTs to be wetted by the liquid under test. The test cell designed to confine the liquid was sealed to the PCB side corresponding to the quartz plate surface opposite to the IDTs. The IDTs pads are electrically connected to the SMA through 50 ▶ characteristic impedance strips into the PCB upper side. The liquid under test is injected inside the test cell and contacts the bottom plate surface. The device test is performed by measuring the S12 scattering parameter by using a HP8753A network analyser at ambient temperature: the modes phase velocity and insertion loss, in the time and frequency domain, are recorded through a data acquisition system from National Instruments. The test cell containing the devices and the network analyser is shown in figure 4.8

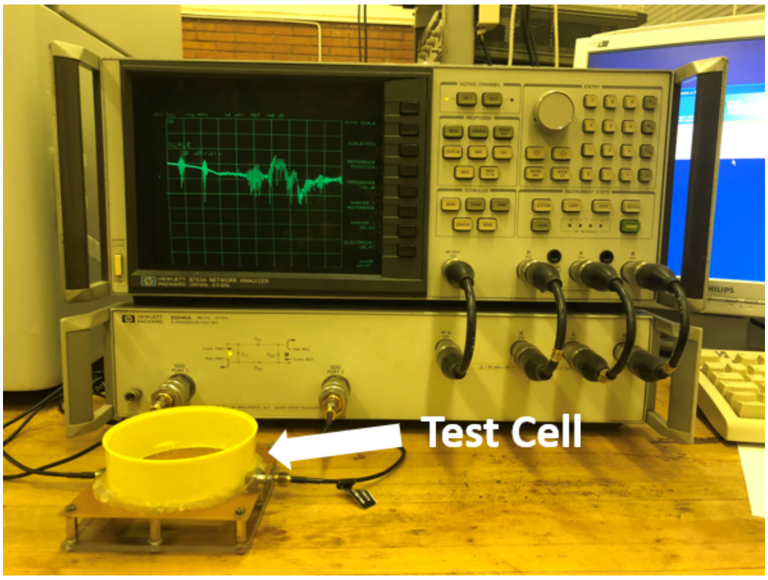

Figure 4.8 The characterisation setup of ST-cut Quartz Lamb waves

Firstly, the characterisation was performed in dry environment. The S21 scattering parameter of is shown in figure 4.9 with comparison with the COMSOL simulation result

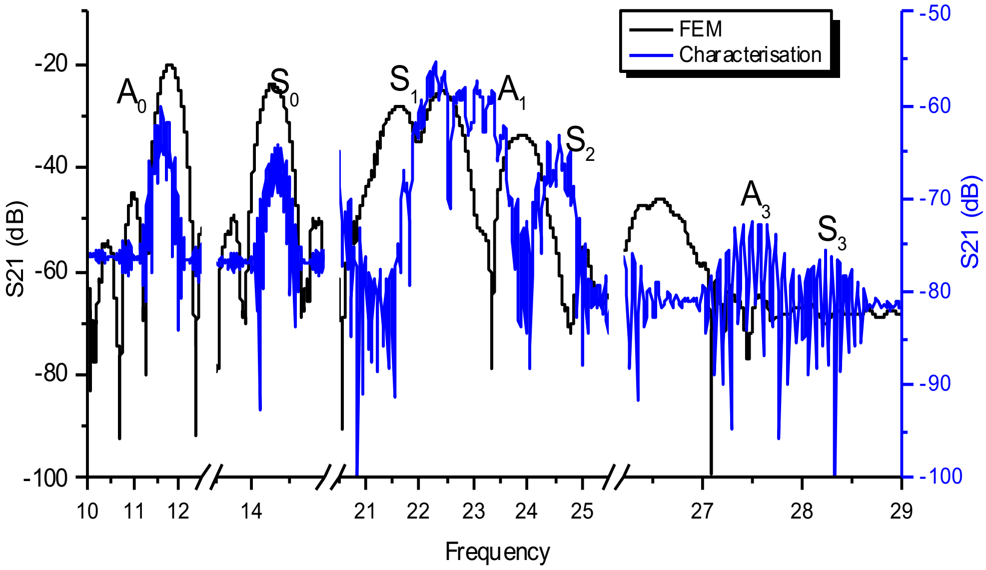

Figure 4.9 Delay Line Frequency Response VS Simulation

The liquid was placed inside the test cell so that the quartz surface opposite to the IDTs are in contact with liquid. Figure 4.10 shows the comparison of frequency responses in air and water

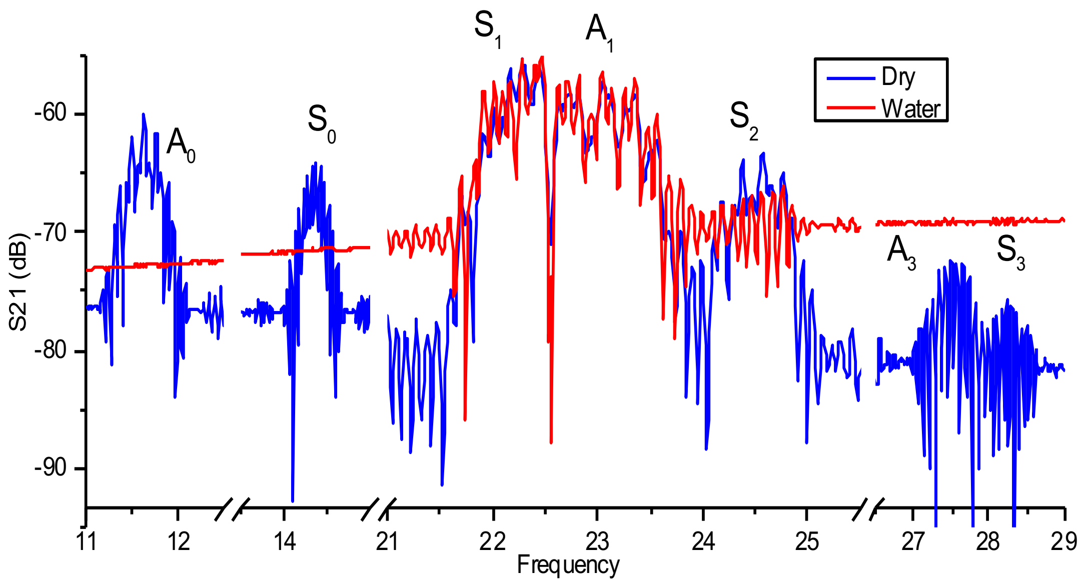

Figure 4.10 Delay line frequency response in air and water

Viscosity Sensor

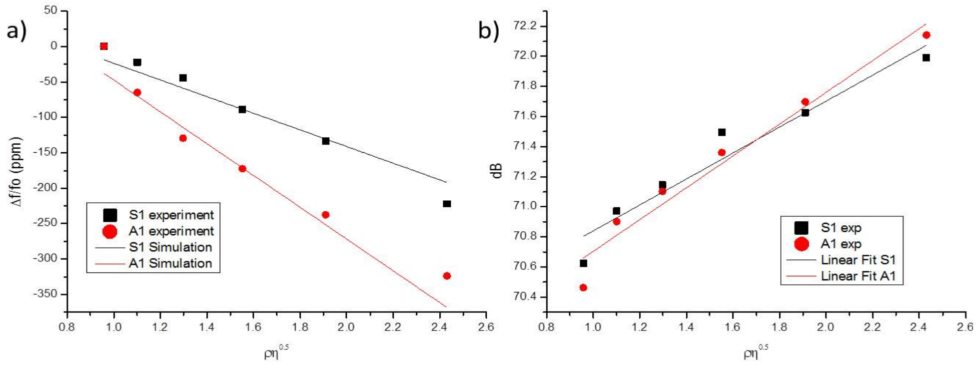

Figure 4.11 Viscosity sensor water glycerol

4.2.2 SiN/AlN thin film Lamb waves

Figure 4.12 XRD

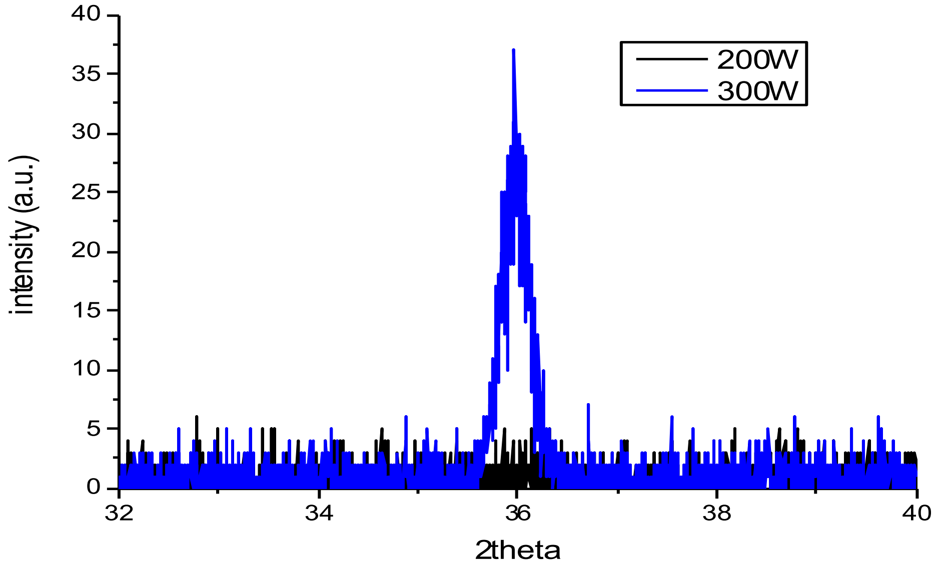

Figure 4.13 XRD of AlN on Silicon

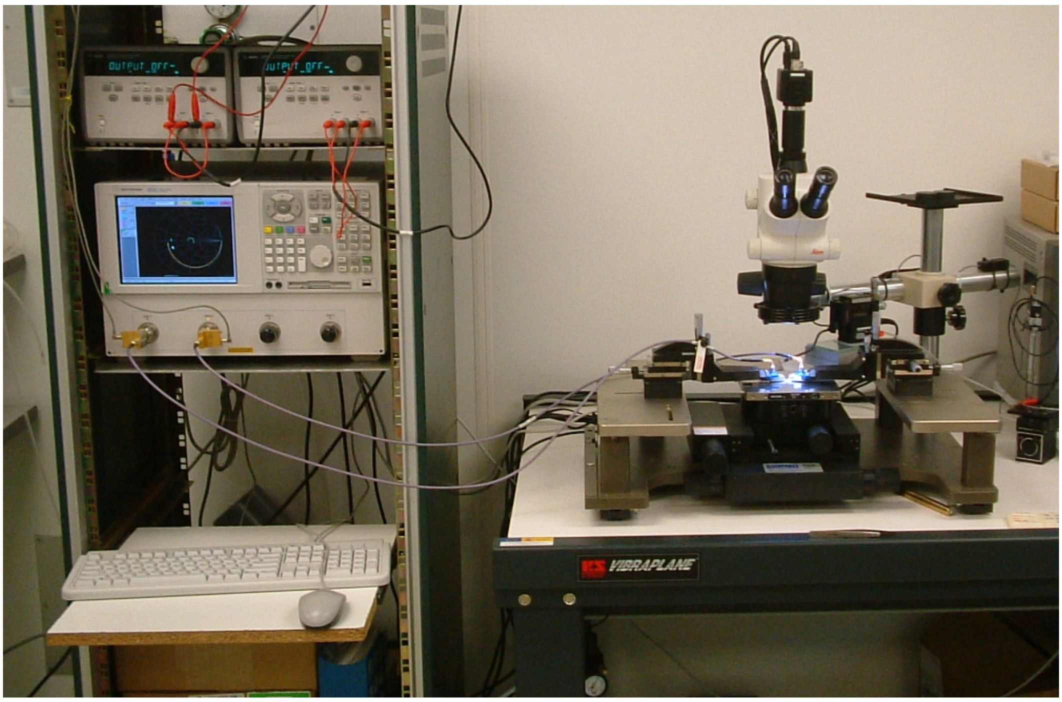

Figure 4.15 RF Probe and VNA

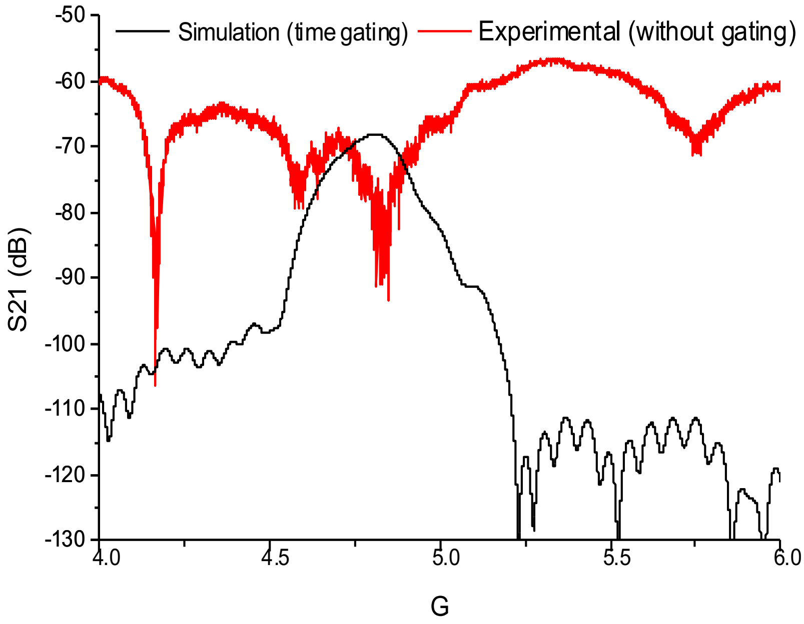

Figure 4.15 RF Probe characterisation result

Bibliography

CHAPTER 5

ZERO GROUP VELOCITY LAMB WAVES

This chapter is devoted for a new concept of electroacoustic resonator devices by exploiting Zero Group Velocity (ZGV) Lamb waves, resulting in a resonator design that do not require metal strip gratings or suspended edges to confine the acoustic energy. The concept of ZGV resonators are theoretically demonstrated on two types of composite thin film: SOI/AlN and a-SiC/ZnO, with numerical calculation for the gas and pressure sensor application respectively.

Related Publications:

C. Caliendo, **M. Hamidullah,** Zero-group-velocity acoustic waveguides for high-frequency resonators, Journal of Physics D: Applied Physics, Volume 50, Number 47, 2017.
Caliendo, C., and **M. Hamidullah**. "Pressure sensing with Zero Group Velocity Lamb modes in self-supported a-SiC/c-ZnO membranes." Journal of Physics D: Applied Physics 51.38 (2018): 385102.

Lamb waves are acoustic guided modes that propagate in finite thickness plates and are strongly dispersive [1]. For some branches of the dispersion curves, a strong resonance can be found that occurs at the frequency minimum: at this frequency, a zero-group velocity (ZGV) Lamb mode occurs that is characterized by a vanishing group velocity combined with a non-zero wave number [2]. More specifically, the zero-group velocity is due to the interference of two modes with the same frequency and mode shape, and propagating with equal phase velocity in opposite directions. As a result, a stationary non-propagating mode is obtained that corresponds to a local resonance in the response spectrum of the plate where the Lamb modes travel. ZGV modes have been proposed for a wide range of applications such as the estimation of the Poisson's ratio [3,4], the measurement of the thickness of plates [5,6], the probing of interfacial stiffness between two plates [7-10], to cite just a few. The available literature refers to ZGV modes along tungsten [4], aluminium [6], glass [9], duralumin [5.10], poly methyl methacrylate [11] and metal plates bonded with sub-millimetric glue layer [9]. Although the literature concerning ZGV Lamb modes is rather extensive, to the authors' knowledge, only a few studies consider the topic of ZGV electro-acoustic resonators on thin suspended acoustic waveguides: in the references [12,13] the first symmetric

Lamb S_1 mode ZGV resonator based on a c-AlN thin suspended membrane (2.5 μm thick and wavelengths of about 8.0–8.8 μm) is theoretically studied and experimentally verified. The impact of the free edges shapes (flat or biconvex) of the piezoelectric suspended rectangular membrane, the tether-to-plate angle (90° or 59° for 'butterfly' shaped plate), electrode configurations, materials, and thicknesses on the performances of the AlN-based Lamb wave resonators have been investigated in references [14-17]. As opposed to the ZGV resonators, the resonators based on a piezoelectric thin suspended membrane with free edges require a more complicated micromachining technology to acoustically isolate the resonator and mechanically couple it to the substrate by two anchors. Indeed, the ZGV points are associated with an intrinsic energy localization: the energy confinement is a natural consequence of the selected acoustic mode thus reducing the technological complexity with respect to that required by the free edges resonators. Figure 5.1 shows the comparison of state-of-the-art resonator with ZGV resonator.

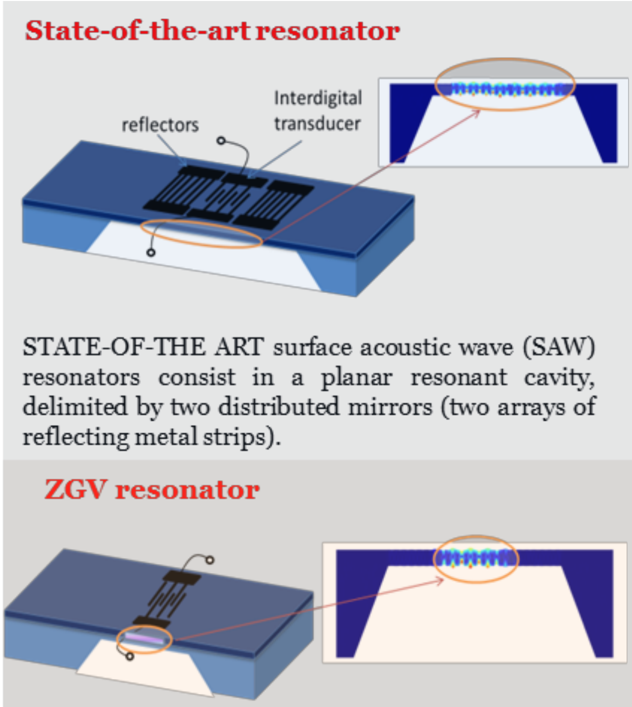

Figure 5.1 the one-port SAW resonator (with the two reflectors) and the ZGV resonator employing only an interdigital transducer.

The characteristics of the ZGV resonators, such as their phase velocity, resonant frequency and Q factor, are affected by the properties of the layer materials, the thickness of the plate, as well as by the electrical boundary conditions. This chapter provides a simulation study of monolithically integrated piezoelectric MEMS RF resonators using silicon on insulator (SOI) substrates with aluminum nitride (AlN) and amorphous silicon carbide (a-SiC) with zinc oxide (ZnO) piezoelectric films with examples of sensor application for gas and pressure sensing respectively.

5.1 Silicon-on-insulator (SOI)/AlN

Silicon on insulator (SOI) technology refers to the use of a layered silicon–insulator–silicon substrate in place of conventional bulk silicon substrates in microelectronics semiconductor manufacturing. SOI substrates are compatible with a broad spectrum of technologies that are used in conventional areas of micro-electronics: they provide the potential for high-performance electronics with multiple integrated functions, such as actuators and sensors, and are suited to produce large-scale integrated systems [18,19]. AlN is a piezoelectric material with unique properties such as a wide band gap, high thermal conductivity, a low thermal expansion coefficient, high breakdown dielectric strength, and the highest acoustic wave velocity among the piezoelectric materials that can be grown in thin film form [20]. SOI/AlN-based suspended membranes offer process robustness and design flexibility to provide devices with multiple ZGV frequencies implemented on single-chip platforms.

5.1.1 Lamb waves dispersion curves in SOI/AlN

The propagation of Lamb waves along a SOI/AlN thin suspended membrane is here investigated. The membrane consists of a piezoelectric AlN layer, 1 μm thick, on top of a SOI suspended membrane with a 10 μm Si layer and a 1 μm thick SiO_2 box layer. Figure 5.2 shows the schematic of the resonator including the array of electrodes on top of the piezoelectric layer. This device can be obtained by standard technological processes, such as the backside SOI/AlN micro-machining process for the fabrication of suspended membranes. In this case the silicon dioxide box plays the role of a back-etching stop layer, allowing the release of a $Si/SiO_2/AlN$ suspended membrane.

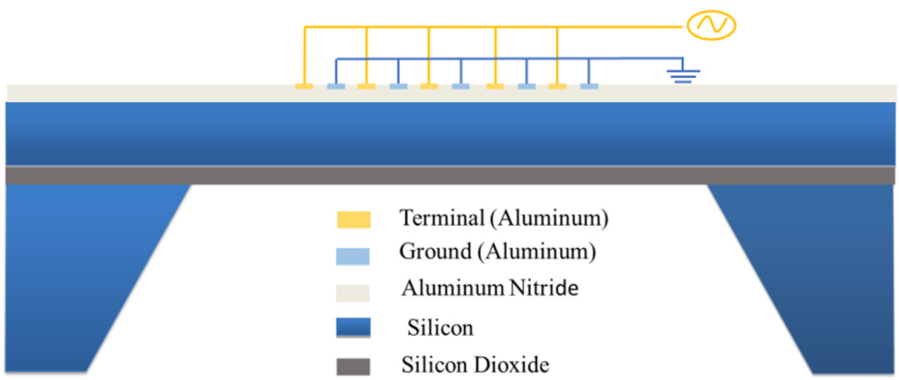

Figure 5.2: Schematic of the Lamb mode resonator on AlN/Si/SiO2 suspended membrane with a thick Si rigid frame.

The total composite plate thickness is $H = h_{SiO_2} + h_{Si} + h_{AlN}$, where h_{SiO_2} is the SiO_2 layer thickness, h_{Si} is the Si layer thickness, and h_{AlN} is the piezoelectric AlN layer thickness. The Lamb waves propagation can be excited and detected by use of interdigitated transducers (IDTs), as for the surface acoustic waves (SAWs). The wavelength of the acoustic wave, λ, is set by the pitch of the interdigital transducer (IDT), while the number of IDTs electrodes is equal to $N = \sqrt{\pi / 4K^2}$, as required to obtain the minimum insertion loss and the maximum frequency bandwidth of the resonator implemented on the SOI/AlN plate; K^2 is the electroacoustic coupling coefficient that depends on the layers thickness and electrical boundary conditions. In the present simulations, the IDTs metallization ratio is supposed to be equal to 1.

The phase velocity dispersion curves of the Lamb-like modes travelling along the SOI/AlN composite plate were calculated and plotted in figure 5.3(a) versus H/λ, being H the total waveguide thickness. The labels near each curve show the corresponding modes order: the fundamental modes are labelled as qS_0 and qA_0, while the higher order modes are indicated with a progressive number. The group velocity dispersion curves of the composite plate were calculated according to the formula $v_{gr}^{n} = v_{ph}^{n}\left(1 + \frac{H}{\lambda}\frac{\partial v_{ph}^{n}}{\partial H/\lambda}\frac{1}{v_{ph}^{n}}\right)$, where n is the mode order, and are shown in figure 5.3(b). The curves of figure 5.3(b) are distinguished on the basis of the color code adopted in figure 5.3(a).

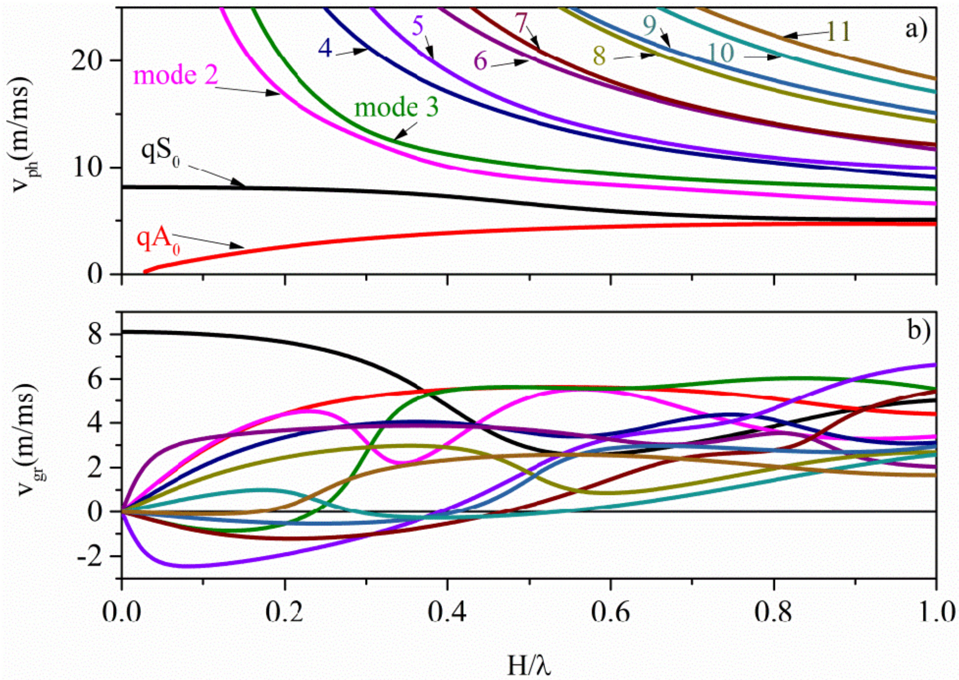

Figure 5.3: (a) The phase velocity and (b) the group velocity versus H/λ of the Lamb modes travelling in the composite plate. Same colored curves in both figures belong to the same mode.

As can be seen in figure 5.3(a) the phase velocity of the lowest two modes, qS_0 and qA_0, (the black and red curves) are continuous with frequency, while the higher order modes originate at a cut-off frequency at which the phase velocity is infinite, and the plate vibrates in longitudinal or shear thickness mode resonance. For the qS0 mode, the group velocity (the black curve of figure 5.3(b)) is equal to the phase velocity in the low-frequency limit but there after falls below the latter, reaching a minimum near the H/λ equal to 0.57. The high-frequency asymptotic limit is the Rayleigh wave velocity. The group velocity of the qA_0 mode (the red curve in figure 5.3(b)) rises rapidly from its low-frequency limit of zero and, at H/λ of about 0.37 and 0.9, it equals that of the S_0-like mode. The group velocity of the higher order modes vanishes at $k = 2\pi/\lambda = 0$, giving rise to a thickness resonance at the cut-off frequency. At these cut off frequencies, multiple reflections between the top and bottom surfaces of the plate result in a thickness resonance. Some branches, corresponding to the 'backward-wave' propagation, occur in the negative-slope region where group velocity and phase velocity have opposite signs. For negative group velocities, the direction of propagation of wave energy and that of wave phase are opposite. In addition to the thickness mode resonances, some Lamb wave resonances, referred to as the ZGV resonances, occur at the frequency values at which some high order modes exhibit null group velocity and finite phase velocity. Figure 5.4 shows a magnification of figure 5.3(b): one can easily observe that all modes have one ZGV point, except the 10 mode that has two ZGV points.

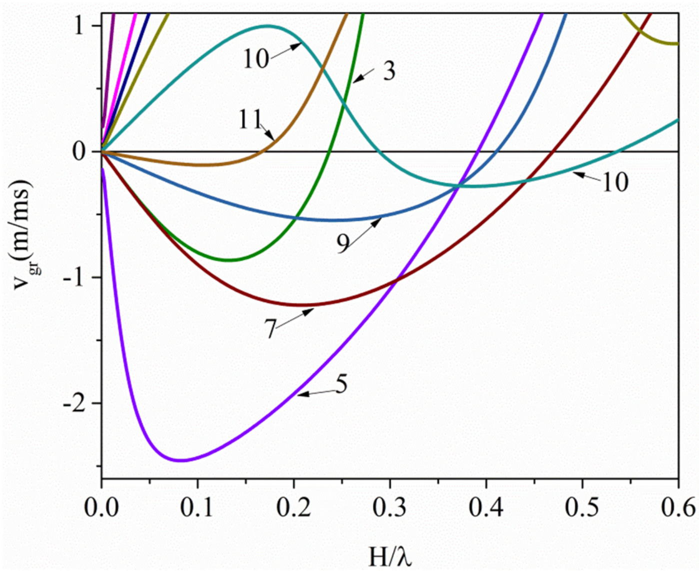

Figure 5.4: A magnification of figure 5.2(b) that shows the single and double ZGV points.

The frequencies of the ZGV points are listed in table 5.1 together with the corresponding wavelength values. As an example, the phase and group velocity dispersion curves of the S1-like mode (qS1), in the vicinity of the ZGV resonance frequency, are shown in figure 5.5 for a composite plate of thickness H = 12 µm. It can be seen that the group velocity is zero at two frequencies corresponding to the thickness resonance frequency (with infinite value of vph, hence $k = 2\pi/\lambda = 2\pi f/vph = 0$) and the ZGV resonance frequency.

Table 5.1. The ZGV mode order, the wavelength, the modes frequency, and the K^2 of the four coupling configurations.

ZGV mode order	λ (μm)	Freq. (MHz)	SFT (%)	STF (%)	SMFT (%)	STFM (%)
3	50	329.71	0.001	0.0035	0.049	0.051
5	30	630.35	0.013	0.027	0.066	0.080
7	25.5	890.74	0.035	0.058	0.051	0.075
9	29	1133.81	0.058	0.080	0.036	0.058
10a	41.5	1372.29	0.077	0.073	0.005	0.001
10b	22	1365.87	0.074	0.093	0.009	0.028

The origin of the latter resonance is due to the behaviour of the dispersion curve at frequencies close to the ZGV resonance, where two branches with different slopes can be distinguished: the upper branch with positive slope, corresponding to the negative vgr values, and the lower vph branch with negative slope, corresponding to the positive vgr values [21]. The upper branch is backward propagating because the phase and group velocities of the mode are of opposite sign, and thus the direction of propagation of the acoustic energy is opposite to the wave vector. On the contrary, the phase and group velocities of the lower branch have the same sign and this branch is considered to be a true mode. In the vicinity of qS1 ZGV resonance frequency, the absolute value of the group velocity of the two branches approach zero, while their phase velocities have the same non-null value. These modes interfere and form the standing qS1 ZGV resonance.

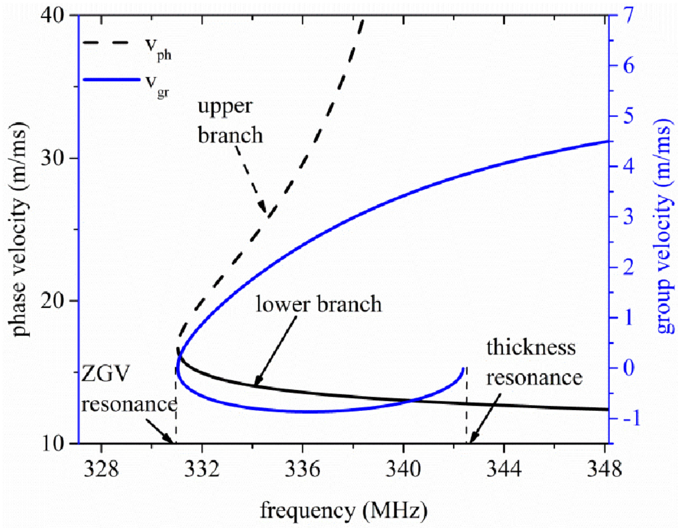

Figure 5.5: Phase and group velocity dispersion curves for the qS1 mode in the vicinity of the zero group velocity resonance.

FEM analysis was performed using COMSOL Multiphysics to explore the field shape of the ZGV points in the composite waveguide. Initially, the plate-guided modes were identified by frequency-response analysis of a 2D composite plate with the IDT of the ZGVR assumed to have five finger pairs, as shown in figure 5.2. For simplicity, the presence of the silicon frame was not accounted in the simulations and the total length of composite plate is 20λ. Traction free boundary conditions were selected for the top and bottom sides of the composite plate, while continuity boundary conditions were selected for the right and left end sides of the waveguide. The geometrical parameters of the ZGVR structure used in the simulation are given in table 5.2.

Table 5.2. The geometrical parameters of the ZGVR structure used in the COMSOL simulation.

IDT Al electrode thickness	100 nm
AlN layer thickness	1 μm
Si layer thickness	10 μm
SiO_2 layer thickness	1 μm
Acoustic wavelength, λ	50 μm, 30 μm, 25.5 μm, 29 μm, 41.5 μm, 22 μm

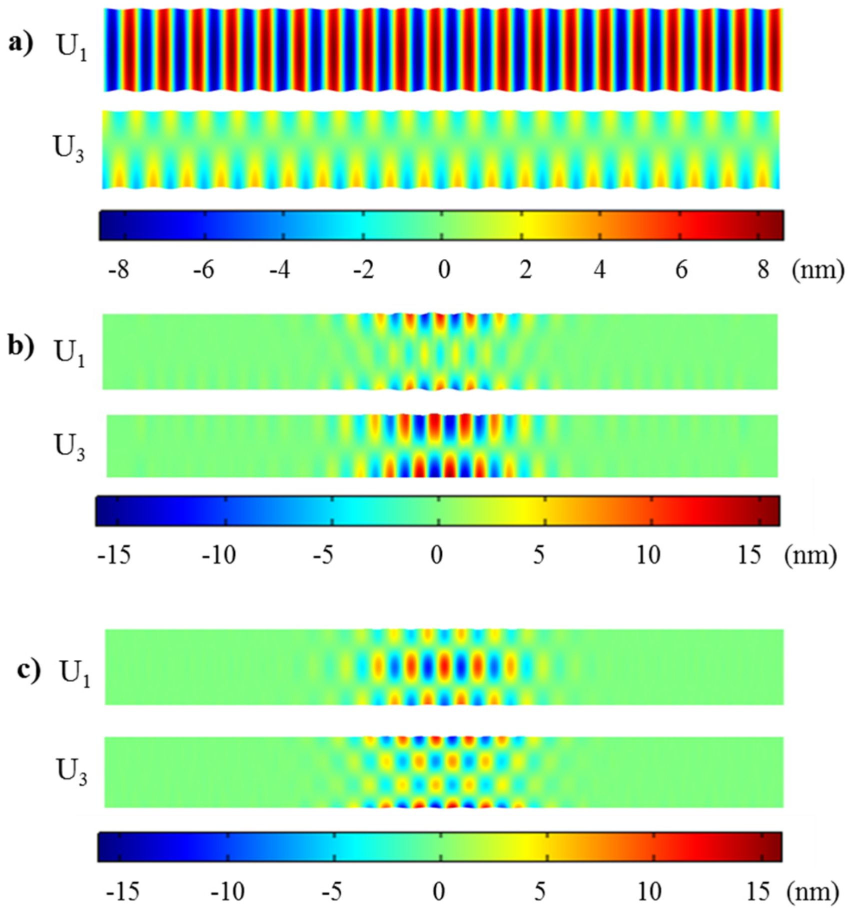

Figure 5.6. The field profile of (a) a propagating mode, the qS0 mode, at frequency 155 MHz and λ = 50 µm; (b) non-propagating ZGV3 mode for λ = 50 µm, (c) non-propagating ZGV5 mode for λ = 30 µm.

As an example, figure 5.6(a) shows the field profile (the longitudinal and shear vertical particle displacement components, U1 and U3) of a propagating mode, the qS0 mode, while figures 5.6(b) and (c) show two non-propagating modes, the ZGV3 and ZGV5 modes. The total displacements of the modes shown in figures 5.6(a)–(c) were determined by an eigenfrequency 2D FEM analysis with applied boundary conditions: the colour density is representative of the relative particle displacement. As can be seen in figures 5.6(a)–(c), the acoustic field shape of the qS0 mode is uniformly distributed under the metal electrodes, as well as in the outside bare region, while the acoustic field of the ZGV3 and ZGV5 modes are localized in the active region of dimension approximately equal to five wavelengths. The acoustic field of the ZGV7, ZVG9, ZVG10a and ZGV10b modes are shown in figure 5.7.

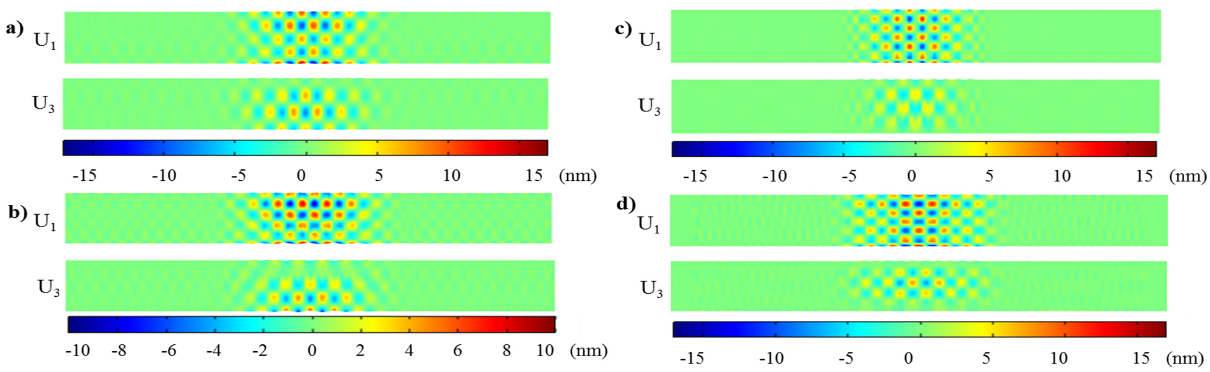

Figure 5.7: The field profile of higher order non-propagating modes, (a) ZGV7 mode for λ = 25.5 µm, (b) ZGV9 mode for λ = 29 µm, (c) ZGV10a mode for λ = 41.5 µm, and (d) ZGV10b mode for λ = 22 µm.

5.1.2 Gas Sensing Application

At the ZGV points, the mode energy is locally trapped in the source area thus these modes are expected to be highly sensitive to the plate thickness and mechanical properties changes, as demonstrated in [22] for homogeneous isotropic plates. In the present study this method is applied to an inhomogeneous composite plate to investigate how the resonator characteristics are affected by the perturbation induced in the mass density of the outer plate layer. The behaviour of the ZGVRs operating as gas sensors was studied under the hypothesis that the surface of the device is covered with a thin polyisobutylene (PIB) film, 0.5 µm thick. The sensor was investigated for the detection of five volatile organic compounds at atmospheric pressure and room temperature: dichloromethane (CH_2Cl_2), trichloromethane ($CHCl_3$), carbontetrachloride (CCl_4), tetrachloroethylene (C_2Cl_4), and trichloroethylene (C_2HCl_3). The phase and group velocity dispersion curves of the PIB-covered SOI/AlN structure were calculated and it was found that, with respect to the uncoated SOI/AlN case, the presence of the PIB layer slightly lowers the frequencies of the first three ZGV points and induces new ZGV points, whose resonant frequencies in air, f_0, are listed in table 5.3. The interaction of the gas molecules with the sensitive PIB layer was simulated as an increase of the mass density of the PIB film, ρ = ρunp. + Δρ, being ρunp. the unperturbed mass density of the PIB layer (in air) and Δρ the partial density of the gas molecules adsorbed in the PIB layer, Δρ = K centerdot M centerdot c0 centerdot P/RT, where P and T are the ambient pressure and temperature (1 atm and 25 °C), c_0 is the gas concentration in ppm, K = 101.4821 is the air/PIB partition coefficient for the studied gas, M is the gas molar mass, R is the gas constant [23-25]. Any effects of the gas adsorption on the PIB layer properties other than the density changes were neglected. The PIB gas adsorption was simulated for gas concentration c_0 in the range from 100 to 500 ppm for the ZGV3, ZGV5, ZGV7, ad ZGV8 modes. It was found that the ZGV resonance frequencies were downshifted by the adsorption of the gas into the PIB sensitive layer: the adsorbed gas increases the PIB mass density and lowers the phase velocity (and then the operating frequency), which can be correlated to the gas concentration. Figures 5.8(a)–(d) show the resonant frequency shift, $\Delta f={{f}_{{\rm air}}}-{{f}_{{{c}_{0}}}}$, versus gas concentration for the four ZGV points, being fair and ${{f}_{{{c}_{0}}}}$ the resonat frequency values in air and at gas concentration c_0. The resonant frequencies in air of the ZGV modes were equal to 323.1298, 616.667, 862.546, and 997.623 MHz, respectively. As can be seen, the frequency shift of each mode has a linear behaviour with respect to the increased mass density of the PIB layer. Moreover, the slope of the curves (i.e. the sensor sensitivity) increases with increasing the resonant frequency.

Table 5.3. The operating frequencies in air, f_0, the PIB mass density increase $\Delta\rho$, and the frequency shift Δf of the ZGV modes in SOI/AlN and of the SAW in yz-$LiNbO_3$ when exposed to 100 ppm of various gases.

		Δf (Hz)				
Gas (100 ppm)	PIB $\Delta\rho$ (kg m^{-3})	ZGV3 (f_0 = 323.1298 MHz)	ZGV5 (f_0 = 616.667 MHz)	ZGV7 (f_0 = 862.546 MHz)	ZGV8 (f_0 = 997.623 MHz)	SAW in $LiNbO_3$ (f_0 = 1121.215 MHz)
Air	0	0	0	0	0	0
CH_2Cl_2	0.01	−61	−158	−831	−3000	−356
$CHCl_3$	0.04	−240	−621	−3261	−13 000	−1394
CCl_4	0.1	−588	−1518	−7975	−32 000	−3408
C_2Cl_4	0.132	−784	−2025	−10 635	−42 000	−21 831
C_2HCl_3	0.166	−986	−2547	−13 378	−53 000	−4544

The ZGV sensors sensitivity to a fixed concentration (c_0 = 100 ppm) of the five volatile organic gases was compared with the theoretical sensitivity of a SAW sensor implemented on a yz-$LiNbO_3$ piezoelectric substrate covered by a PIB layer, 0.5 μm thick, with operating frequency equal to 1.121 GHz [23, 26]. Table 5.3 lists the operating frequencies in air, the PIB mass density increase $\Delta\rho$, and the frequency shifts of each ZGV mode and of the SAW sensor of reference [23, 26] when exposed to 100 ppm of various gases at atmospheric pressure and temperature. The relative frequency shift $\Delta f/f_0$of the ZGV3 sensor is comparable to that of the SAW sensor, while the ZGV5, ZGV7 and ZGV8 sensors show a $\Delta f/f_0$ much higher than that of the SAW sensor.

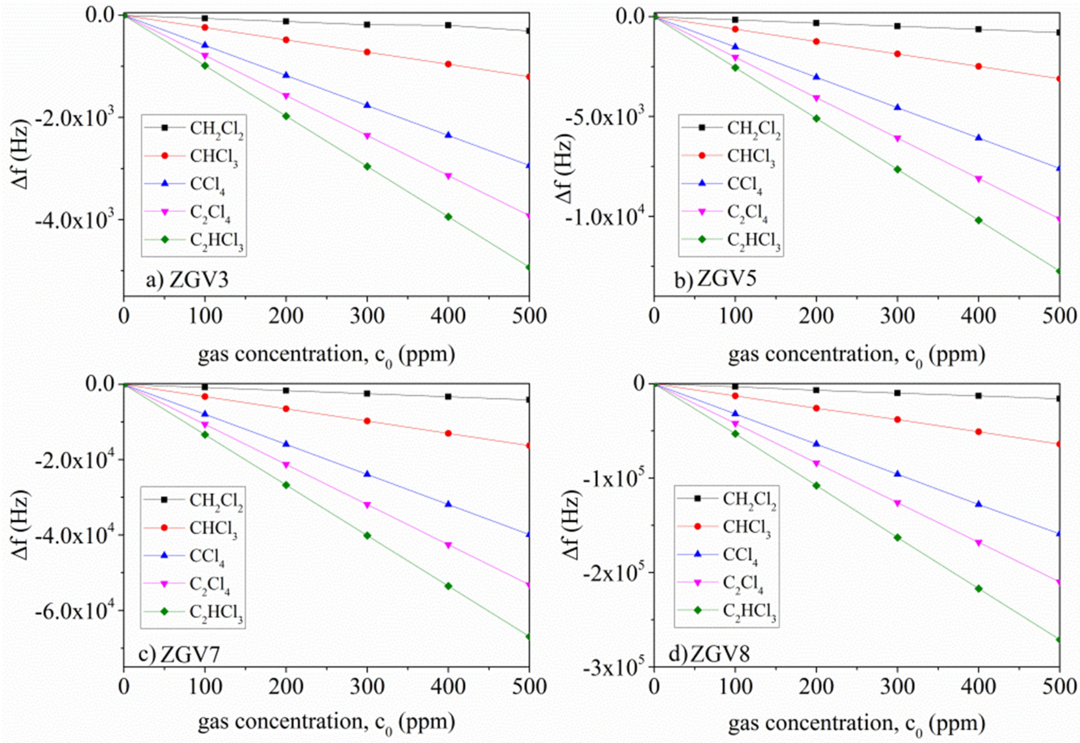

Figure 5.8: The resonant frequency shift versus gas concentration curves of the (a) ZGV3, (b) ZGV5, (c) ZGV7, and (d) ZGV8 modes for five different gases.

To fully evaluate the potential of these sensors for detecting very low gas concentrations, temperature fluctuation effects should be removed from the sensor response. To this purpose some strategies can be exploited: (1) incorporation of a temperature sensor and compensation circuitry or software; (2) dual device configuration design; (3) temperature compensation. The first method is based on the numerical correction of the sensor response by using data from an independent measurement of the temperature by means of a nearby temperature sensor. The second method is based on the use of a dual resonator configuration that consists of a reference device and an active device: both the two devices are implemented on the same substrate and are covered by the PIB layer. The reference and active sensors must be configured to allow the former to be exposed both to the carrier gas and to the common-mode interfering measurands, while the latter is also exposed to the gas to be tested. A mixer circuit provides the difference between the signal from the reference device and that from the active device, so that the mass density variations of the PIB layer exposed to the gas could be distinguished independently of the effects of the temperature changes. Alternatively, a 'stack' of metal and/or oxide layers of proper thicknesses and appropriate sign of the temperature coefficient of stiffness can be add to the device to yield a composite structure exhibiting minimal temperature coefficient [27].

5.2 Amorphous Silicon Carbide (a-SiC)/c-ZnO

Non-piezoelectric amorphous SiC (a-SiC) shows excellent properties such as a high acoustic wave velocity, resistance to chemicals, high hardness and compatibility with the integrated circuit technology as it can be deposited by a r.f. magnetron sputtering system [28–30] at 200 °C onto Si(1 0 0) substrates from a sintered SiC target. Piezoelectric wurtzite ZnO thin film technology has been widely used for many years for the fabrication of SAW devices onto non-piezoelectric substrates, such as silicon, glass, and sapphire, to name just a few. When the piezoelectric ZnO film is grown onto high-velocity materials, such as diamond or SiC, it is a promising candidate for high frequency, high sensitivity micro sensors **[31].** A bi-layered a-SiC/ZnO composite thin plate, few micrometers thick, can be obtained by standard technological processes, such as the magnetron sputtering growth of the a-SiC and ZnO layers onto a Si(1 0 0) wafer, and the backside Si/a-SiC/ZnO micro-machining process for the fabrication of suspended membranes. In this case the a-SiC film plays the role of a back-etching stop layer, allowing the release of the a-SiC/ZnO suspended membrane.

This section provides a simulation study of the ZGV modes in a-SiC/ZnO waveguides for different layers thicknesses. The ZGVR pressure sensitivity, i.e. the relative resonant frequency shift per unit pressure change, has been calculated under external uniform differential pressure, in the 1–10 kPa range. The finite element method (FEM) analysis has been performed to investigate the ZGVR strain, stress and internal pressure, thus allowing to get a further insight into the ZGVR-based pressure sensitivity. The feasibility of high-frequency micro-pressure sensor based on a-SiC and ZnO thin film technology was demonstrated by the present simulation study. A pressure sensitivity (9 ppm kPa^{-1} in the 4–10 kPa range) higher or at least comparable to that of SAWRs-based sensors [32-34] was predicted for the 1–1 ZGV2-based pressure sensor.

5.2.1 Lamb waves dispersion curves in a-SiC/c-ZnO

The phase and group velocity dispersion curves of the a-SiC/ZnO composite plates were calculated by the software DISPERSE [35] for different layers thicknesses. The w-ZnO material constants were extracted from [36]; as the Disperse software does not account for the ZnO piezoelectric constants, then its database was provided with the ZnO stiffened elastic constants calculated with a MATLAB routine. The a-SiC/ZnO composite structure brakes the mid-plane symmetry, thus the symmetric and antisymmetric nature of the modes is hardly distinguished, except for the two fundamental modes, named quasi-S0 (qS0) and quasi-A0 (qA0); the higher order modes are labeled with a progressive number as well as the corresponding ZGV points. Different a-SiC/ZnO composite plates were modelled with variable a-SiC and ZnO layers thickness in the 1–5 µm range. These plates will be labelled hereafter with two numbers: the first corresponds to the ZnO layer thickness in µm, and the second corresponds to the thickness of the a-SiC layer. As an example, figures 5.9 (a) and (b) show the phase velocity dispersion curves of the Lamb modes travelling in the a-SiC/ZnO 2.5–5 and 5–2.5 composite plates: it can be noticed that the number of the propagating modes and their velocity are highly affected by the two layers thickness.

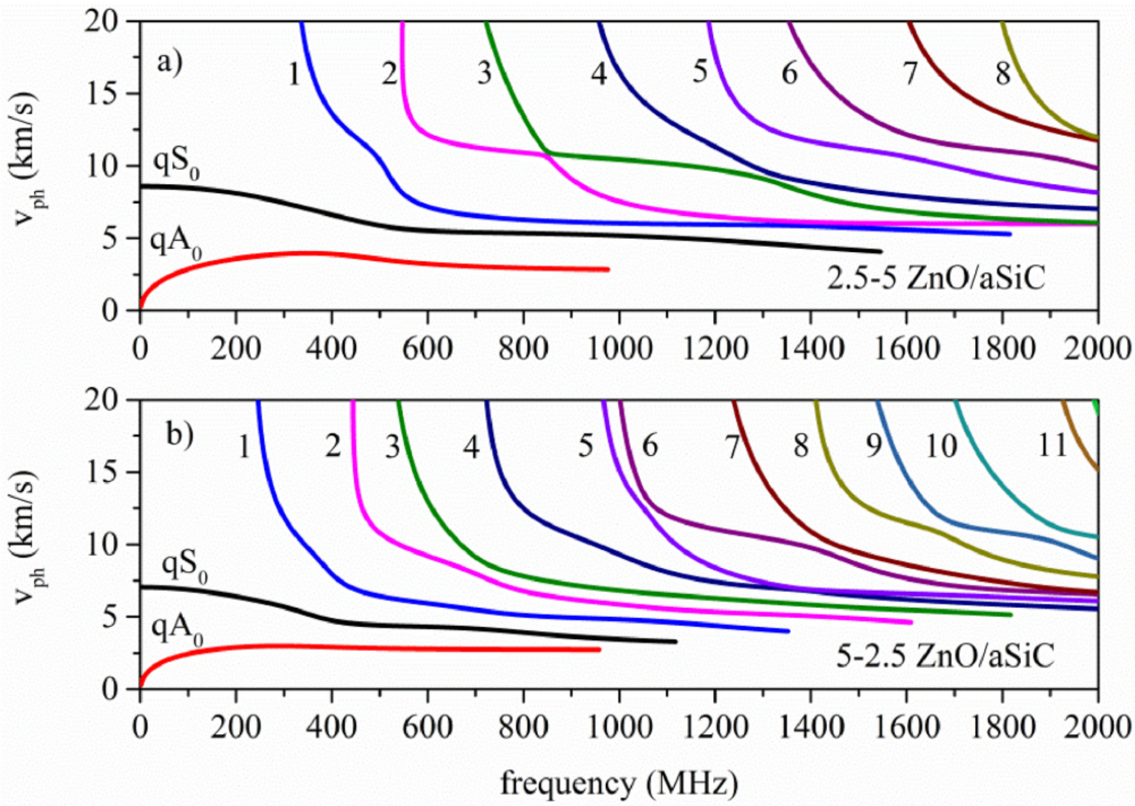

Figure 5.9: The phase velocity dispersion curves of the Lamb modes traveling along the (a) 2.5–5 and (b) 5–2.5 a-SiC/ZnO composite plates.

In the studied frequency range (from few MHz up to 2 GHz), it was found that the 1–5 and 2–5 composite plates exhibit only one ZGV point corresponding to the mode 2 (namely the quasi-S_1 mode, qS_1) at frequencies f_0 = 763.633 and 604.668 MHz, hereafter named ZGV2. The 3–5 and 4–5 composite plates exhibit three ZGV points corresponding to mode 2 (at frequencies f_0 = 499.535 and 424.938 MHz), mode 5 (f_0 = 1059.72 and 900.896 MHz), and mode 8 (f_0 = 1590.61 and 1334.08 MHz), named hereafter ZGV2, ZGV5 and ZGV8. The 5–5 composite plate exhibits up to five ZGV points corresponding to mode 2, mode 5, mode 8, mode 11 and mode 14, named ZGV2, ZGV5, ZGV8, ZGV11 and ZGV14, at f_0 = 369.378, 781.106, 1157.21, 1570.64 and 1954.31 MHz, respectively. As an example, figures 5.10(a) and (b) show the group velocity vgr dispersion curves of the modes 2 and 5, for different ZnO layer thicknesses and fixed a-SiC layer thickness (5 μm). The abscissa is the total plate thickness-to-wavelength ratio $H_{tot}/\lambda = (h_{a\text{-}SiC} + h_{ZnO})/\lambda$.

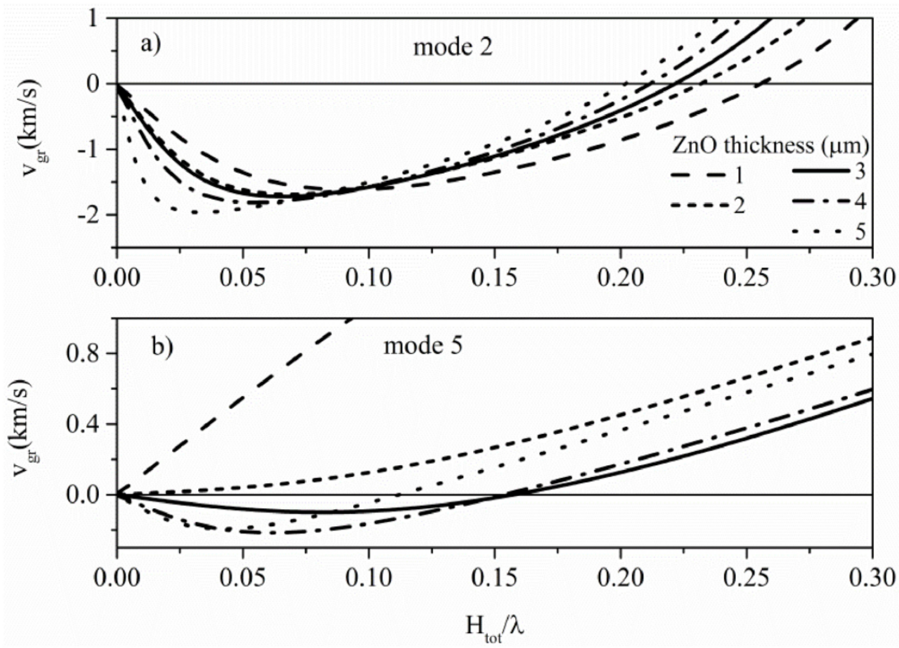

Figure 5.10: The group velocity versus H_{tot}/λ of the (a) mode 2 and (b) mode 5 of the a-SiC/ZnO plate; the a-SiC thickness is fixed (5 μm) while the ZnO thickness is the running parameter.

With increasing the piezoelectric layer thickness from 1 to 5 μm, the abscissa of the ZGV2 decreases as the corresponding wavelength increases and thus the ZGV2 resonant frequency $f_0 = v_{ph}/\lambda$ moves toward lower values. The dispersion curves of the mode 5 do not cross the zero group velocity (ZGV) axis for the 1–5 and 2–5 plates, as opposed to the thicker plates.

The mode shape of the ZGV2, ZGV5 and ZGV8 for the 3–5 composite plate is shown in figures 5.11(a)–(c) as an example. The middle of the composite membrane, 8 μm thick, was chosen to be the zero depth in order to emphasize the plate asymmetry with respect to its midplane. The acoustic field profile of the ZGV2 still shows some peculiarities typical of the first anti-symmetric mode S_1. The field profiles of the ZGV5 and of the ZGV8 have the characteristic shape of a higher order mode but it is artificial to identify a similarity with a symmetric or anti-symmetric mode.

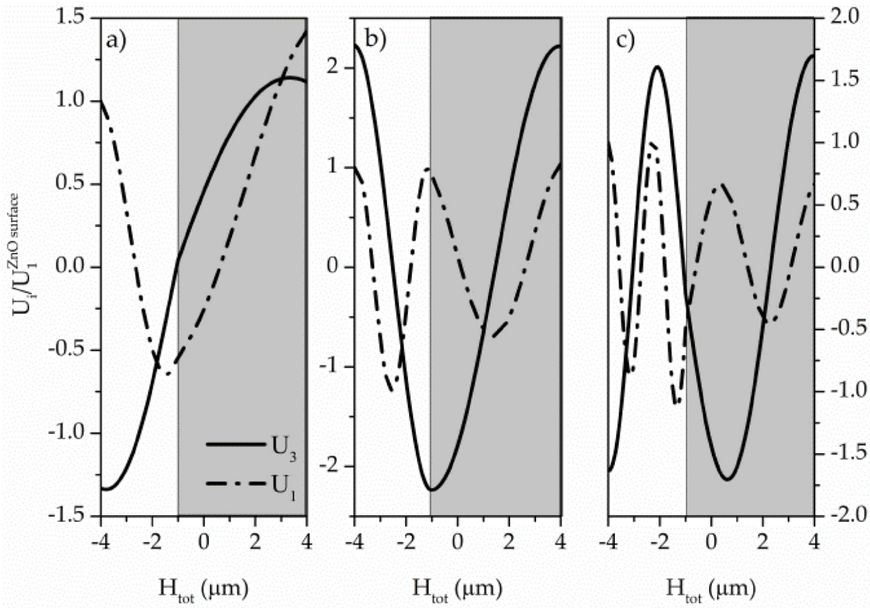

Figure 5.11: The mode shape of the (a) ZGV2, (b) ZGV5 and (c) ZGV8 of the 3–5 structure; the grey area defines the a-SiC thickness. The middle of the composite membrane, 8 μm thick, represents the zero depth.

FEM simulations have been carried out by using COMSOL Multiphysics 5.2 to explore the field shape of the ZGVRs in the composite waveguide. The simulations accounted for five Al IDT finger pairs, 0.1 μm thick and λ/4 wide, located onto the free surface of the ZnO layer: the terminal (1 V) and ground electrical boundary conditions were applied at the top surface of the interdigitated electrodes alternately.

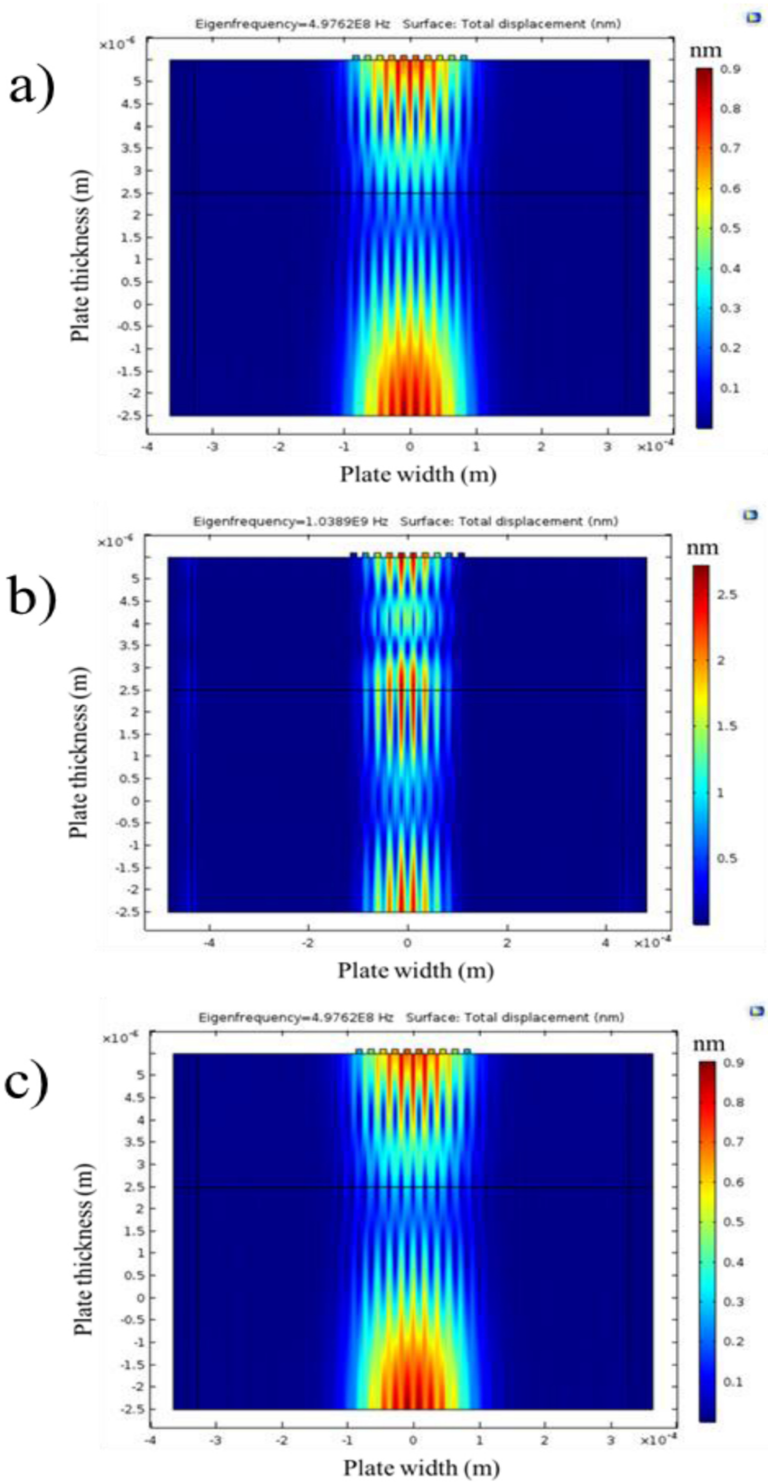

Figure 5.12: The absolute surface total displacement of the (a) ZGV2, (b) ZGV5, and (c) ZGV8 mode for the 3–5 composite plate, with λ = 36, 49 and 35 µm, respectively.

Two perfectly matched layers (PMLs), each one wavelength wide, were applied on the left and right side of the a-SiC/ZnO plate, in order to model a domain with open boundaries through which the wave pass without undergoing any reflection; the traction free boundary conditions were applied to the top and bottom sides of the composite plate. The total length of the studied cell is 20 ▪ λ, including the two PMLs. The maximum and minimum mesh size were λ/10 and λ/100. The ZnO was assumed to have an elastic loss tanδ = 0.002. As an example, figures 5.12(a)-(c) show the absolute total displacement of three zero group velocity points (ZGV2, ZGV5 and ZGV8) belonging to the 3–5 plate, and corresponding to λ = 36, 49 and 35 μm, respectively. As can be seen, the displacement is confined only in the region underneath the IDT.

5.2.2 Pressure Sensing Application

The acoustic energy of a ZGV mode is concentrated under the IDT but, if an external pressure is applied that induces the bending of the membrane, the resonator frequency is expected to change. The investigation of this feature can be exploited for sensing applications or for evaluating the resonator stability under variable environmental pressure. By following the calculation procedure outlined in [35], the major factors determining the pressure sensitivity of the ZGVR were investigated based on mode 2 of the 1–1 composite plate for the smfT configuration. The 1–1 ZGV2 and 5–5 ZGV2 are characterized by a different wavelength value (λ = 10 and 50 μm, respectively) but equal thickness-to-wavelength ratio (H_{tot}/λ = 2/10 = 0.2 and H_{tot}/λ = 10/50 = 0.2) which corresponds to the highest K^2 value, as shown in figure 5.13; the 1–1 ZGV2, besides having a K^2 equal to that of the 5–5 ZGV2, it has the additional technological advantage to require thinner layers and thus smaller sized device.

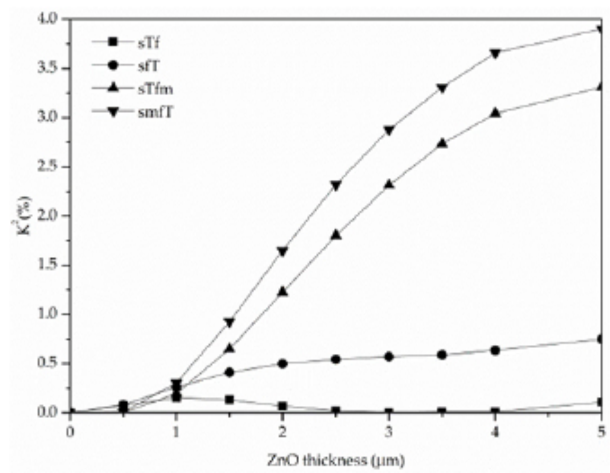

Figure 5.13 The K^2 dispersion curves of the ZGV2 mode of the four coupling configurations; the a-SiC layer thickness is fixed (5 μm thick).

When a membrane is exposed to an external pressure, it resulted strained and the internal pressure changes. As a consequence, the material constants of the membrane change as well as the thickness and the geometrical dimensions of the membrane, thus resulting in a resonance frequency shift. The contributions to the pressure sensitivity of the ZGVRs due to the dependence on the pressure of the elastic constants, the lateral and vertical strains were studied. 2D and 3D FEM COMSOL Multiphysics analysis has been performed to determine the pressure sensitivity of the ZGVR by two-steps simulations: (1) 3D stationary study of mechanical deflection of the membrane with symmetric boundary conditions, under uniform differential pressure; (2) 2D eigen-frequency study of a single pair of IDT at the H/λ corresponding to the ZGV2, with continuity boundary conditions. Figure 5.14 shows the schematic of the ZGV-based pressure sensor; the topological design parameters of the device are listed in table 5.3.

Table 5.3: The topological design parameters of the plate.

Design parameter	*value*
Acoustic wavelength, λ	10 μm
ZnO film thickness, h_{ZnO}	1 μm
a-SiC film thickness, $h_{a\text{-}SiC}$	1 μm
Device aperture	40 λ
Number of finger pairs	40
Membrane size	1000 × 1000 μm^2
IDT area, AIDT	400 × 400 μm^2
Al electrodes thickness	50 nm

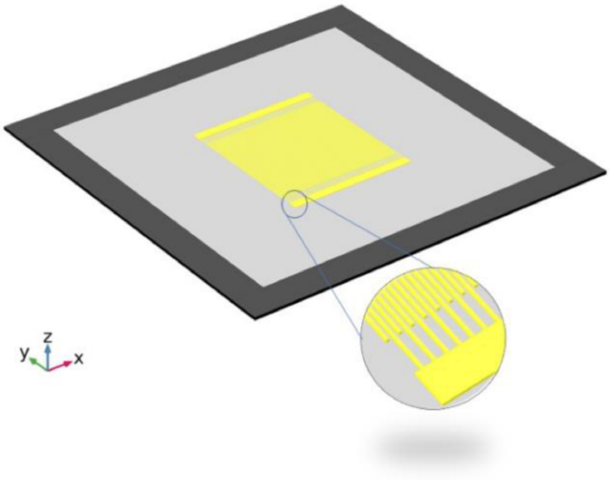

Figure 5.14. The schematic of the suspended membrane: the silicon frame is black, the membrane is gray; the IDT is yellow.

3D stationary study of mechanical deflection of the membrane

Figure 13 shows the total displacement of the 1–1 composite plate under 1 kPa uniform pressure difference: a variable pressure is supposed to be applied to the lower surface of the membrane while the upper one is maintained at fixed (ambient) pressure. The vertical axis of the membrane deformation is scaled up by the factor of 10 for graphical reason, otherwise the deformation could not be clearly observed. Due to the symmetry of the problem, just a quarter of the membrane, with applied symmetric boundary conditions, is sufficient for the analysis. As can be seen, most of the displacement is concentrated in the center of the membrane.

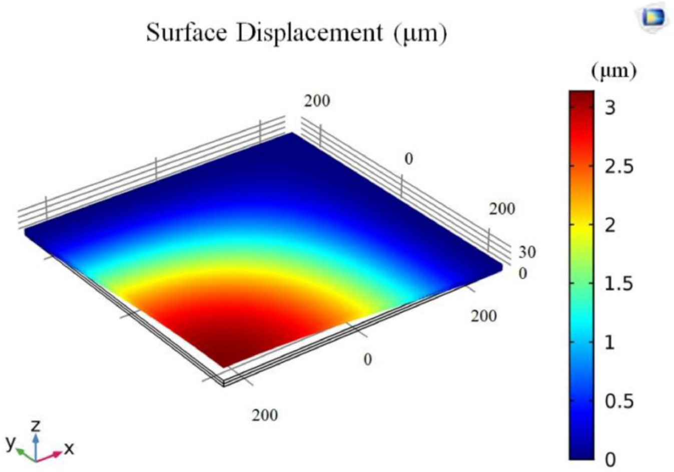

Figure 5.15: The total displacement of the 1–1 composite membrane under 1 kPa ambient pressure difference. The vertical axis of the membrane deformation is scaled up by the factor of 10.

The FEM model was used to determine the strain (S_{xx}, S_{yy} and S_{zz}), stress (T_{xx}, T_{yy} and T_{zz}) and internal pressure Pint = $-(T_{xx} + T_{yy} + T_{zz})/3$, at the interface of the two layers, as well as at the free surface of each layer. Figures 5.16(a)–(c) show S_{xx}, S_{zz} and P_{int} versus the distance from the center of the membrane. Each figure shows three curves: the solid and dash curves are referred to the free surface of the ZnO and a-SiC layer, and the dot-dash curves are referred to the interface between the two layers, respectively. The gray area represents half the IDT area, AIDT/2: inside this area the Sxx, Szz and Pint are almost constant.

The volume average values of the strain and internal pressure, S_{xx}, S_{zz} and P_{int}, were derived inside the ZnO and the a-SiC layers, underneath the IDT area: the data obtained are listed in table 2. The S_{xx} , S_{zz} and P_{int} represent the layers elongation, the thickness change and the internal pressure the plate is subjected to, due to the applied differential pressure. As it can be seen from table 2, the 1 kPa pressure induces a remarkable internal pressure (MPa order of magnitude). The $\overline{S_{xx}}$, $\overline{S_{zz}}$, and $\overline{P_{int}}$were then calculated for different external pressure values in the 1–10 kPa range.

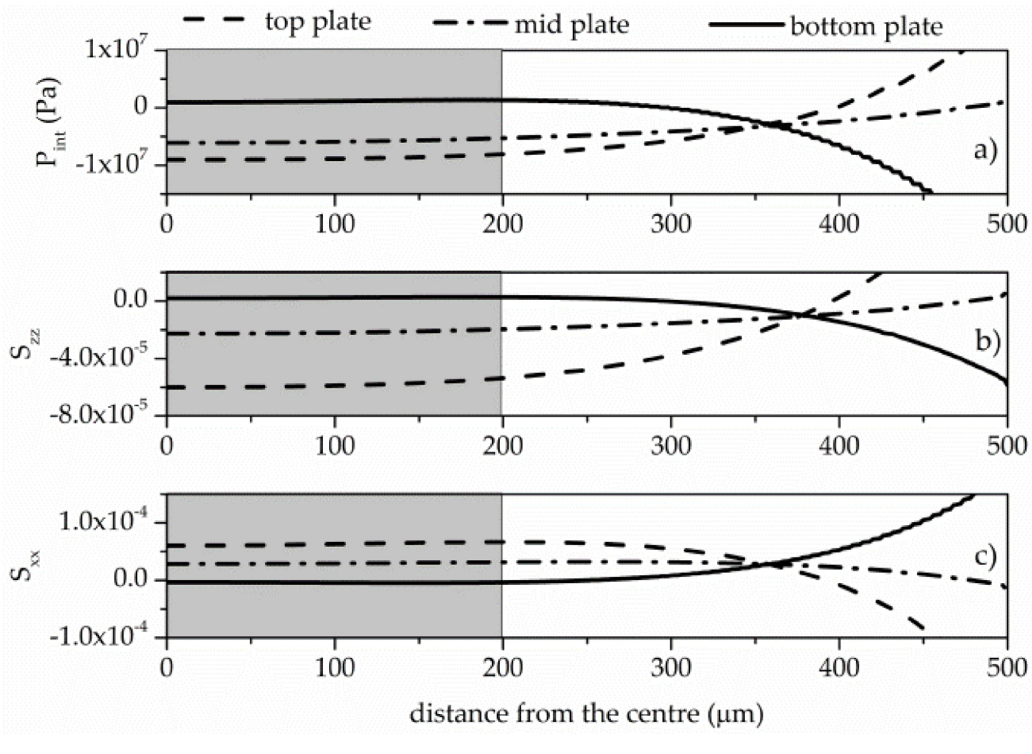

Figure 5.16: (a) The internal pressure Pint, (b) the Szz and (c) Sxx strain components versus the distance from the centre of the membrane; the solid and dash curves are referred to free surface of ZnO and a-SiC layer, and the dot-dash curves are referred to the interface between the two layers, respectively. The gray area represents half the IDT area, $A_{IDT}/2$.

Table 2. The $\overline{P_{int}}$ internal pressure, and the $\overline{S_{xx}}$ and $\overline{S_{zz}}$ strain mean values of the 1–1 a-SiC/ZnO plate subjected to 1 kPa uniform constant differential pressure.

Layer	$\overline{P_{int}}$ (MPa)	$\overline{S_{xx}}$ (ppm)	$\overline{S_{zz}}$ (ppm)
ZnO	−6.22	41.368	−41.256
a-SiC	−2.93	10.444	−6.278

2D eigen-frequency study

The eigen-frequency study of the ZGV2 for the 1–1 composite plate was performed for three perturbed conditions:

1. The IDT wavelength was assumed to be equal to

$$\lambda_{pert} = \lambda(1 + \overline{S_{xx}^{ZnO}}) \quad (1)$$

under the hypothesis that the IDT is positioned onto the free surface of the piezoelectric layer, and that the wavelength is not affected by the $\overline{S_{xx}^{a\text{-}SiC}}$; the two layers thickness and material constants are assumed to be unaffected by the applied differential pressure P.

2. The thickness of each layer was assumed to be equal to

$$h_{ZnO}^{pert} = h_{ZnO}(1 + \overline{S_{zz}^{ZnO}}) \quad (2)$$

and

$$h_{a\text{-}SiC}^{pert} = h_{a\text{-}SiC}\left(1 + \overline{S_{zz}^{aSiC}}\right). \quad (3)$$

wavelength and the materials constants are assumed to be unaffected by P.

3. The two layers elastic constants and mass density were changed according to their pressure dependence

$$c_{ij}^{pert} = c_{ij} + \left({}^{\partial c_{ij}}\!/\!_{\partial P}\right) \cdot P_{int} \quad (4)$$

and

$$\rho_{pert} = \rho + \left(\partial\rho / \partial P\right) \cdot P_{int}; \qquad (5)$$

the thickness of each layer and the wavelength were assumed to be unaffected by P

The a-SiC and ZnO pressure derivatives of the elastic constants [36, 7] c_{ij} and mass density ρ are listed in table 3.

Table 3. The pressure derivatives of the mass density and elastic constants of ZnO and a-SiC.

Material	Pressure derivative of material constants		
a-SiC	$\partial c_{11} / \partial P = 3.49$	$\partial c_{12} / \partial P = 4.06$	$\partial\rho/\partial P = 16.06$ (kg m^{-3} GPa^{-1})
	$\partial c_{11} / \partial P = 3.8$	$\partial c_{12} / \partial P = 5.2$	$\partial c_{13} / \partial P = 4.7$
ZnO	$\partial c_{33} / \partial P = 3.7$	$\partial c_{44} / \partial P = -0.53$	$\partial\rho / \partial P = 37.8$ (kg m^{-3} GPa^{-1})

The Murnaghan equation of state

$$P = \left(\frac{B}{B'}\right) \cdot [\left(\frac{V_0}{V_{pert}}\right)^{B'} - 1] \qquad (6)$$

was used to calculate the w-ZnO relative mass density change ρ_0 / ρ caused by the applied pressure P, where ρ and ρ_0 are the pressure-perturbed and unperturbed mass density, B(142.6 GPa) and B' (3.6) are the ZnO bulk modulus and its pressure derivative, $B' = \partial B/\partial P$; V_{pert} and V_0 are the perturbed and equilibrium volumes [38].

The Murnaghan equation of state for isotropic elastic solidi [39]

$$P = a \cdot (f + 5 \cdot f^2) \qquad (7)$$

was used to evaluate the pressure derivative of the a-SiC mass density, with $f = 0.5 \cdot \left\{\left(V_0 / v\right)^{2/3} - 1\right\}$ and $a = 3 \cdot c_{12} + 2 \cdot c_{44}$.

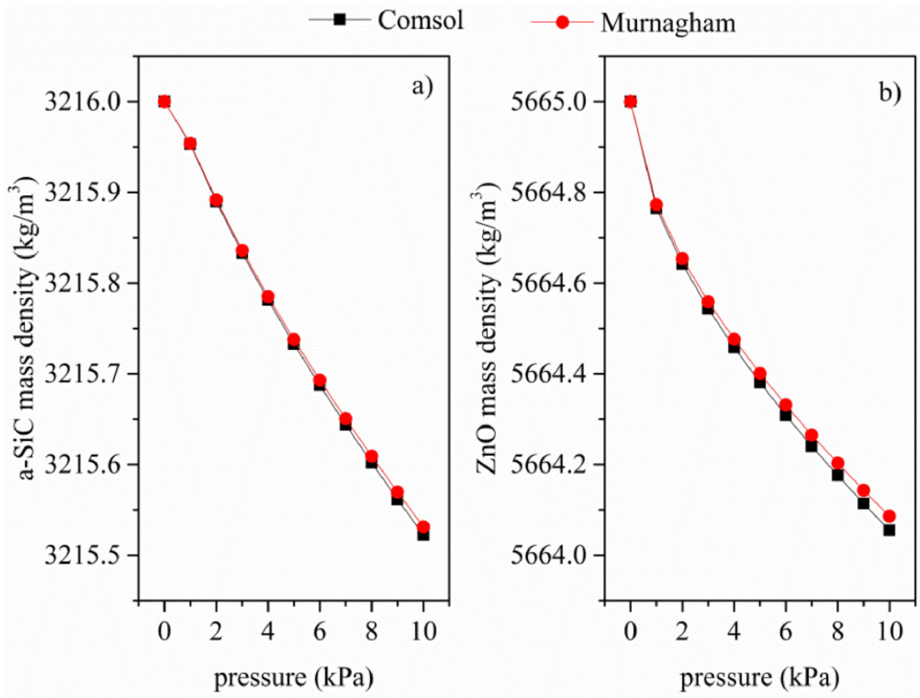

Figure 5.17. The mass density versus pressure curves of (a) a-SiC and (b) ZnO; the red circle and black square points were calculated by the Murnagham equation and by COMSOL simulation, respectively.

The pressure derivatives of the mass density for both the ZnO and a-SiC layers were also calculated by 3D FEM stationary study. The ZnO and a-SiC mass density, as a function of Pint, was deduced by the plate volume change V0/Vpert = ρ/ρ0, being Lx, Ly and Lz the equilibrium membrane sides along the axis system, V0 = Lx . Ly . Lz the unperturbed volume, $V_{pert} = V_0 \cdot (1 + S_{xx}) \cdot (1 + S_{yy}) \cdot (1 + S_{zz})$ the perturbed volume. The a-SiC and ZnO mass density evaluated by the two methods for different pressure values are very close, as shown in figure 5.17. The discrepancy between the data obtained with the two methods is from 7 . 10−3 to about 3 . 10−2 kg m−3 for ZnO, and from 7 . 10−4 to 8.7 . 10−3 kg m−3 for a-SiC, respectively, in the studied pressure range.

Figure 5.18 shows the relative resonant frequency shifts of the ZGV2, $\Delta f/f_0$, induced by $\overline{S_{xx}}$, $\overline{S_{zz}}$ and $\overline{P_{int}}$ versus the applied differential pressure; $\Delta f = f_{pert} - f_0$, f_0 = 1841.754 MHz is the unperturbed resonant frequency, and f_{pert} is the pressure-perturbed resonant frequency.

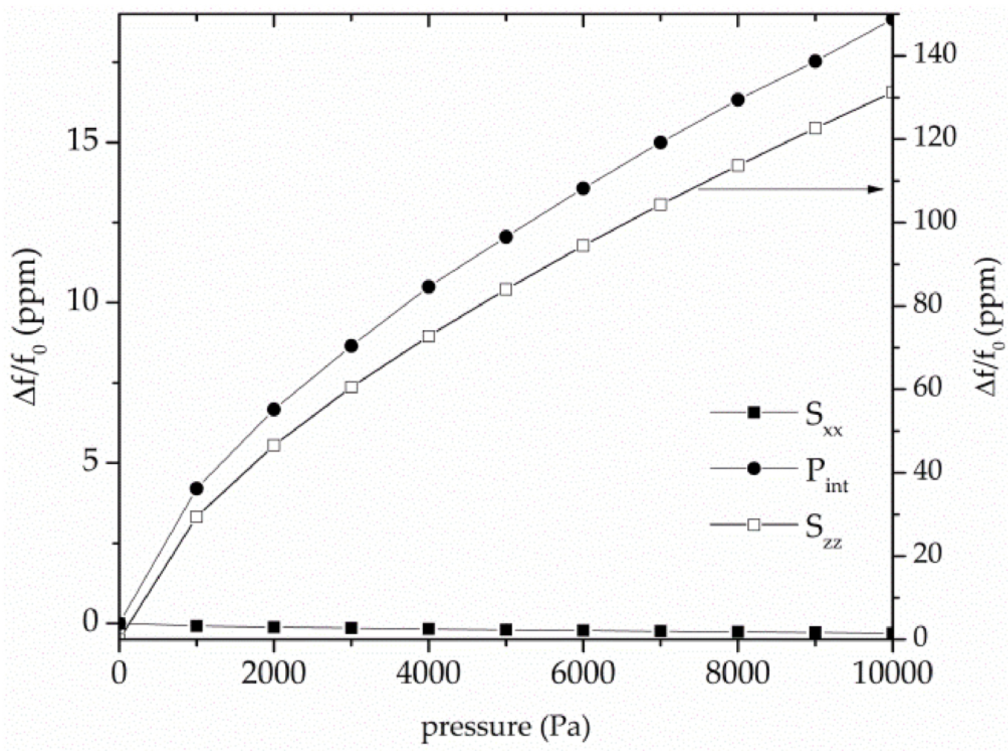

Figure 5.18. The $\overline{S_{xx}}$, $\overline{S_{zz}}$, $\overline{P_{int}}$ -induced ZGVR relative frequency changes versus the applied differential pressure for the 1–1 composite plate.

From figure 5.18 it appears evident that the ZGV2 relative frequency shifts induced by the changes in the membrane length, thickness and internal pressure are quite different. The effect provided by the $\overline{S_{zz}}$ changes is positive since the membrane thickness decreases under the applied pressure, and the wave velocity (and hence the resonant frequency) consequently increases. This effect is dominant over the others since the ZGV highly dispersive behavior ensures a large sensitivity to any thickness changes. The contribution related to $\overline{S_{xx}}$ is negative as the wavelength increases under the applied pressure, and the resonant frequency consequently decreases; it is also marginal since the mode corresponds to the ZGV dispersion. The effect provided by the $\overline{P_{int}}$ changes is positive and smaller than that provided by $\overline{S_{zz}}$, as opposed to the results shown in [35] where the $\overline{P_{int}}$ contribution is dominant and the pressure-induced mass density changes are not accounted for. In the present simulation, the a-SiC and ZnO pressure-induced mass density changes are accounted for: the mass density contribution has the effect to lower the elastic constants contribution to the mode velocity increase.

Figure 5.19 shows the *sum* of the relative frequency shifts shown in figure 5.18, $\left(\Delta f/f_0\right)_{sum} = \left(\Delta f/f_0\right)_{S_{xx}} + \left(\Delta f/f_0\right)_{S_{zz}} + \left(\Delta f/f_0\right)_{P_{int}}$, versus the differential pressure.

Figure 5.19 also shows the total frequency shift $\left(\Delta f / f_0\right)_{total}$ versus the differential pressure: the ordinate was calculated by changing, at the same time, the membrane size (thickness and length) and the two layers material constants (mass density and elastic constants). In the 4–10 kPa pressure range, the two curves of figure 5.19 can be linearly fitted, showing a sensor sensitivity, i.e. the curve slope, of 9.34 and 10.98 ppm kPa^{-1}, respectively. As the two curves are very similar, then we can argue that the net response of the ZGVR-pressure sensor can be approximated, in the studied pressure range, as the sum of the responses caused by the different contributions.

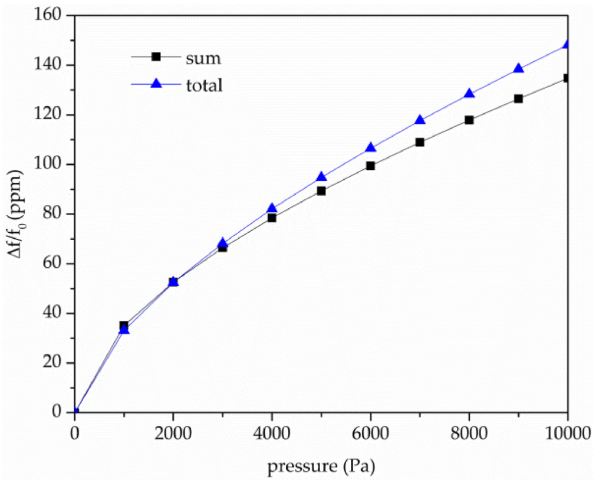

Figure 5.19. The $\left(\Delta f / f_0\right)_{sum}$ and the $\left(\Delta f / f_0\right)_{total}$ versus the pressure curves of the ZGV2-based sensor on the 1–1 composite plate.

As an example, figure 5.20 shows the ZGV2 absolute admittance versus frequency curves for the 1–1 plate at three differential pressure values (0 Pa, 5 kPa and 10 kPa).

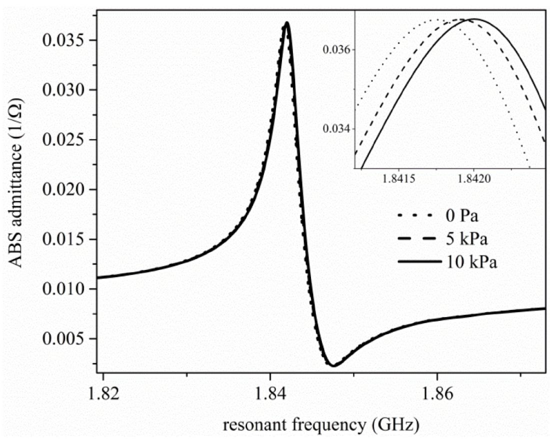

Figure 5.20. The ZGV2 absolute admittance versus frequency curves of the 1–1 plate, for the sfT configuration; the pressure is the running parameter.

The non-linear behavior of the ZGVR-based pressure sensor, shown in figure 5.19, is in agreement with that of the high-frequency (f_0 = 10.77 GHz) one port SAWR-based pressure sensor implemented on AlN(300 nm)/diamond(20 μm) suspended substrate, when a pressure variation in the range from 0 to 100 kPa is applied, as described in [32].The rough side of the diamond free standing layer was glued with an epoxy adhesive to an alumina bulk substrate (few hundreds of μm thick) with a hole in the middle. The pressure underneath the hole was kept constant at atmospheric pressure, while a variable pressure was applied to the upper surface of the membrane. The SAWR-based sensor has a pressure sensitivity (0.31 ppm kPa^{-1}) lower than that of the ZGVR-based sensor, but it has a smaller surface area (the periodicity of the finger pairs is 800 nm, the number of periods was 100 for both the IDT and the reflectors).

In [33], a fully implantable wireless pressure sensor is presented that works in the 0–26.66 kPa pressure range and shows a sensitivity of about 12 ppm kPa^{-1}. The sensor device consists in a 5.3 by 4 mm thin quartz diaphragm on which a one-port SAWR has been implemented that works at about 868 MHz. Since the total space occupied by an implantable sensor also includes the antenna, it is important to minimize its size. The small size of the sensor based on ZGV2 1–1, as well as its compatibility with integrated circuit technology and its sensitivity to low pressures, make it a suitable candidate for the design of implantable devices.

In [34], the effect of the diaphragm shape (circular and rectangular) on the pressure sensitivity of an AlN/SOI-based SAWR sensor was investigated in the 0–1724 kPa pressure range, and an improved sensitivity from 0.0055 to 0.025 ppm kPa^{-1} was found. This result suggests us to study the effects of the membrane shape on the pressure sensitivity of the ZGV-based sensor, as well as the optimization of the IDT design parameters, also including the presence of reflectors to compensate a possible deviation of the theoretical thicknesses from the calculated ones.

The propagation characteristics of the ZGV Lamb modes along a-SiC/c-ZnO composite plates have been modelled for different ZnO and a-SiC layer thicknesses. The phase and group velocity, and the K^2 of four coupling configurations have been theoretically studied specifically addressing the design of enhanced-coupling, microwave frequency electroacoustic devices that are reliable to fabricate by conventional sputtering technologies and microlithography technique. Quite good K^2 corresponds to both the qS_0 and the ZGV2, for the same-thickness plate, but the former has a resonant frequency significantly lower than that of the ZGVR, and requires a larger device area including the IDT and two reflectors. The pressure sensitivity of the ZGV2 resonator was studied for the 1–1 plate subjected to a uniform differential pressure varying in the 1–10 kPa range. A ZGVR sensitivity of about 9 ppm kPa^{-1} was predicted in the 4 to 10 kPa range where the relative frequency change versus the pressure curve can be linearly fitted.

The present study was performed to demonstrate proof of concept of ZGVRs in pressure sensing applications. The a-SiC/c-ZnO-based ZGV2 sensors are proven to achieve remarkable performances (high sensitivity and enhanced coupling efficiency) that are important prerequisite for the design of future devices to be used in the context of chemical, biological and physical quantities detection. Further studies are in progress to improve the device performances, based on the IDT design parameters (such as single electrode and multiple-split electrodes) and the membrane shape.

Bibliography

[1] Rose J L 1999 Ultrasonic Waves in Solid Media (Cambridge: Cambridge University Press)

[2] Prada C, Clorennec D and Royer D 2008 Zero-group velocity modes and local vibrations of an elastic plate J. Acoust. Soc. Am. 123 3156

[3] Baggens O and Ryden N 2015 Poisson’s ratio from polarization of acoustic zero-group velocity Lamb mode J. Acoust. Soc. Am. 138 EL88

[4]Grünsteidl C, Murray T W, Berer T and Veres I A 2016 Inverse characterization of plates using zero group velocity Lamb modes Ultrasonics 65 1–4

[5] Cès M, Clorennec D, Royer D and Prada C 2011 Thin layer thickness measurements by zero group velocity Lamb mode resonances Rev. Sci. Instrum. 82 114902

[6] Cho H, Hara Y and Matsuo T 2014 Evaluation of the thickness and bond quality of three-layered media using zero-group-velocity Lamb waves J. Phys.: Conf. Ser. 520 012023 IOPscience

[7] ezil S, Bruno F, Raetz S, Laurent J, Royer D and Prada C 2015 Investigation of interfacial stiffnesses of a tri-layer using zero-group velocity Lamb modes J. Acoust. Soc. Am. 138 3202

[8] Cho H, Yaguchi Y and Ito H 2015 Characterization of the bond quality of adhesive plates utilizing zero-group-velocity Lamb waves measured by a laser ultrasonics technique Mech. Eng. J. 2 14-00335

[9] Mezil S, Laurent J, Royer D and Prada C 2014 Non contact probing of interfacial stiffnesses between two plates by zero-group velocity Lamb modes Appl. Phys. Lett. 105 021605

[10] Bruno F, Mezil S, Laurent J, Royer D, Ducousso M and Prada C 2016 Zero group velocity resonances of three layer plates for bonding evaluation Review of Progress in Quantitative Nondestructive Evaluation, Conf. Paper p 175
[11] Holland S D and Chimenti D E 2003 Air-coupled acoustic imaging with zero-group-velocity Lamb modes Appl. Phys. Lett. 83 2704
[12] Yantchev V, Arapan L, Katardjiev I and Plessky V 2011 Thin-film zero-group-velocity Lamb wave resonator Appl. Phys. Lett. 99 033505
[13] Yantchev V, Arapan L, Ivanov I, Uzunov I, Katardjiev I and Plessky V 2012 Parametric study of thin-film zero-group velocity resonators (ZGVR) IEEE Int. Ultrasonics Symp. Proc. pp 307–10
[14] Lin C-M, Lai Y-J, Hsu J-C, Chen Y-Y, Senesky D G and Pisano A P 2011 High-Q aluminum nitride Lamb wave resonators with biconvex edges Appl. Phys. Lett. 99 143501
[15] Zou J, Lin C-M and Pisano A P 2014 Quality factor enhancement in Lamb wave resonators utilizing butterfly-shaped AlN plates IEEE Int. Ultrasonics Symp. Proc. pp 81–4
[16] Abdolvand R, Lavasani H M, Ho G K and Ayazi F 2008 IEEE Trans. Ultrason. Ferroelectr. Freq. Control 55 2596
[17] Sorenson L, Fu J L and Ayazi F 2011 Technical Digest of Int. Conf. on Solid-State Sensors, Actuators, and Microsystems (Beijing, China,) p 918
[18] Nguyen B-Y, Celler G and Mazuré C 2009 A review of SOI technology and its applications J. Integr. Circuits Syst. 4 51–4
[19] Kononchuk O and Nguyen B-Y 2014 Silicon-on-Insulator (SOI) Technology: Manufacture and Applications (Woodhead Publishing Series in Electronic and Optical Materials) 1st edn (Amsterdam: Elsevier)
[20] Levinshtein M E, Rumyantsev S L and Shur M S (ed) 2001 Properties of Advanced Semiconductor Materials: GaN, AlN, InN, BN, and SiGe (New York: Wiley)
[21] Balogun O and Murray T W 2007 Simulation and measurement of the optical excitation of the qS1 zero group velocity Lamb wave resonance in plates J. Appl. Phys. 102 064914
[22] Clorennec D, Prada C and Royer D 2007 Local and noncontact measurements of bulk acoustic wave velocities in thin isotropic plates and shells using zero group velocity Lamb modes J. Appl. Phys. 101 034908
[23] Ahmadi M T, Ismail R and Anwar S 2017 Handbook of Research on Nanoelectronic Sensor Modeling and Applications (IGI Global Engineering Science Series) (Hershey, PA: IGI Global) (https://doi.org/10.4018/978-1-5225-0736-9)
[24] Lindgren E R, Rawlinson K S, McGrath L K and Wright J L 2003 Development of a surface acoustic wave sensor for in situ monitoring of volatile organic compounds Sensors 3 236–47
[25] Grate J W and Abraham M H 1991 Solubility interaction and design of chemically selective sorbent coatings for chemical sensor and arrays Sensors Actuators B 3 85–111
[26] Johnson S and Shanmuganantham T 2014 Design and analysis of SAW based MEMS gas sensor for the detection of volatile organic gases Int. J. Eng. Res. Appl. 4 254–8

[27] Ballantine D S, White R M, Martin S J, Ricco A J, Zellers E T, Fye G C and Wohltjen H 1997 Acoustic Wave Sensors: Theory, Design, and Physico-Chemical Applications (London: Academic)

[28] A.K. Costa; S.S. Camargo Jr, Properties of amorphous SiC coatings deposited on WC-Co substrates, Mat. Res. vol.6 no.1 (2003).

[29] Silicon-Based Material and Devices, Properties and Devices, Vol. 1 Materials and processing, chapter 1, Optical, Structural and Electrical properties of amorphous silicon carbide films, Ed. Hari Singh Nalwa, Academic Press 2001.

[30] C Caliendo, "Theoretical investigation of high velocity, temperature compensated Rayleigh waves along AlN/SiC substrates for high sensitivity mass sensors", Appl. Phys. Lett. 100 (2), 021905 (2012).

[31] Y.Q. Fu, J.K. Luo, X.Y. Du, A.J. Flewitt, Y. Li, G.H. Markx, A.J. Walton, W.I. Milne, "Recent developments on ZnO films for acoustic wave based biosensing and microfluidic applications: a review", Sensors and Actuators B 143 606–619 (2010).

[32] J.G. Rodríguez-Madrida,*, G.F. Iriarte a, O.A. Williamsb,1, F. Callea, "High precision pressure sensors based on SAW devices in the GHz range", Sensors and Actuators A 189 364– 369 (2013)

[33] Olive H. Murphy, Mohammad Reza Bahmanyar, Alessandro Borghi, Christopher N. McLeod, Manoraj Navaratnarajah, Magdi H. Yacoub, Christofer Toumazou, "Continuous in vivo blood pressure measurements using a fully implantable wireless SAW sensor", Biomedical Microdevices 15(5), Springer, DOI 10.1007/s10544-013-9759-7.

[34] Tao Wang, Xiaojing Mu, Andrew Benson Randles, Yuandong Gu,and Chengkuo Lee, "Diaphragm shape effect on the sensitivity of surface acoustic wave based pressure sensor for harsh environment", Appl. Phys. Lett. 107, 123501 (2015).

[35] E Anderås, I Katardjiev and V Yantchev, "Lamb wave resonant pressure micro-sensor utilizing a thin-film aluminium nitride membrane", J. Micromech. Microeng. 21 085010 (2011)

[36] Margarita Prikhodko, M. S. Miao, and Walter R. L. Lambrecht, "Pressure dependence of sound velocities in 3C−SiC and their relation to the high-pressure phase transition", Phys. Rev. B 66, 125201, (2002).

[37] Sadao Adachi, Properties of Group-IV, III–V and II–VI Semiconductors, 2005 John Wiley & Sons, Ltd ISBN: 0-470-09032-4, Wiley Series in Materials for Electronic and Optoelectronic Applications.

[38] Claus F. Kingshim, Andreas Waag, Axele Hoffmann, Jean Geurts, "Zinc oxide: from fundamental properties towards novel applications", Springer Series in Materials Science, vol. 120, Springer-Verlag Berlin Heidelberg, p. 220 (2010), doi 10.1007/978-3-642-10577-7.

[39] F. D. Murnaghan, "Finite Deformations of an Elastic Solid", American Journal of Mathematics, Vol. 59, No. 2, pp. 235-260, (1937)

CHAPTER 6

CONCLUSION

This chapter will summarise the result of this thesis project and the contribution the advancement in the state of the art of acoustic wave sensor and recommend the future work to achieve full potential of higher order qL-LWs for sensor application.

6.1 Summary and Contribution

This thesis has demonstrated the sensor application of higher order qL-LWs devices, started from theoretical analysis, the FEM simulation and finally the fabrication and the characterisation of higher order qL-LWs devices in liquid environments as viscosity sensor. The attempt to miniaturise the qL-LWs devices using piezoelectric thin film is also reported. Furthermore, the theoretical analysis and FEM simulation of Lamb waves ZGV resonator is described with possible application of gas and pressure sensor.

There are four main contributions in this thesis project toward the advancement of the state of the art in the sensor application of acoustic waves devices.

1. The in-depth technical review of various type of acoustic waves devices which can provide valuable information in for the peers in related field in choosing and designing SAW sensor for liquid environment

2. FEM simulation model of Lamb waves devices using COMSOL Multiphysics eigenfrequency, frequency domain and time domain study are demonstrated. The model are really useful in predicting the behaviours of higher order Lamb waves, obtaining the mode shapes and the displacement component, and calculating the expected sensitivities of the sensor.

3. Fabrication process of higher order qL-LWs devices on single crystal ST-cut Quartz substrate and composite thin film SiN/AlN. The characterisation result of ST-cut Quartz sample agreed with simulation result and confirming the feasibility of higher order qL-LWs devices for sensor application in liquid environments.

4. The theoretical and simulation study of Lamb waves ZGV resonator gives an insight and promising application of electroacoustic ZGV resonator for sensor application without the needs of metal strip gratings or suspended edges, thus reduce the sizes of the sensor and simplifying fabrication processes.

6.2 Future Work and Recommendation

Nevertheless, there are also several main challenges faced during this thesis project. Future works on this topic are recommended to give better understanding in analysis and design of higher order Lamb waves, and to fulfil the full potential for sensor application.

1. There is no a "perfect" software to satisfy all need of theoretical calculation and simulation of Lamb waves, the use of COMSOL software accompanied by DISPERSE and McGill software is the best method for completing the study of Lamb waves and any other acoustic modes in general. Thus, the software development work is still an important gap to be filled for future work.

2. The fabrication process of thin film higher order is proven to be quite challenging process. While the conventional fabrication process with silicon micromachining by DRIE process is currently a standard proven method, the process development to obtain the right process parameter can be quite challenging. The fabrication process development to simplify to process flow is recommended for future work. One of possible alternative is surface micromachining technique with by using sacrificial layer for releasing the suspended thin membrane.

3. The realisation of ZGV resonator for sensor application is a great interest by fabricating and characterising of the ZGV resonator. The acoustics research team in IFN-CNR under the guidance of Dr. Cinzia Caliendo is currently in process of designing and fabricating the ZGV resonator on X-cut $LiNbO_3$ substrate.

By addressing all the challenges above and continuous work in this research topic, an integrated acoustic waves sensor that can be used for various sensor applications can be realised in advancing the acoustic waves sensor technology